2018

Quantifying Time Retarded Electromagnetic Fields and Their Applications in Transmission Lines

Brandon Thomas Gore
University of South Carolina

Quantifying Time Retarded Electromagnetic Fields and Their Applications in Transmission Lines

by

Brandon Thomas Gore

Bachelor of Science
Mississippi State University 2005

Master of Science
University of South Carolina 2007

Submitted in Partial Fulfillment of the Requirements

for the Degree of Doctor of Philosophy in

Electrical Engineering

College of Engineering and Computing

University of South Carolina

2018

Accepted by:

Paul G. Huray, Major Professor

Yinchao Chen, Committee Member

Guoan Wang, Committee Member

Peng Ye, Committee Member

Cheryl L. Addy, Vice Provost and Dean of the Graduate School

Dedication

This work is dedicated to my son, Mason William Gore. After you were born half way through this journey, my pursuit of more education was no longer an egocentric endeavor. It is my hope that completing this work is a motivation toward your boundless future opportunities.

"Time, patience, and perseverance shall accomplish all things."

Acknowledgments

This work was completed during my tenure at two separate employers: Intel Corporation and SAMTEC Incorporated. Fortunately, most of my close coworkers remained the same at both companies.

I am forever indebted to Richard Mellitz for his willingness to be a technical mentor throughout the past 13 years. He not only taught me how to be a signal integrity engineer, but he has a unique creative spirit and inexhaustible passion for new ideas. A great deal of the motivation for exploring pulse propagation on microstrip transmission lines came from him.

John Abbott was ever pragmatic and kept me grounded when discussing applicability of time retarded effects and test fixture designs. Adam Gregory was always willing to discuss ideas; his ability to quickly grasp complex topics is something that I admire. Scott McMorrow provided valuable metrics for analyzing simulation and measurement results such as the use of phase delay. Ken Young introduced me to LaTeX and provided many templates and illustration ideas to make this work visually appealing. Ted Ballou, Dan Hughes, and Jimmy Hogan made this work readable by editing and proofreading.

My manager during my time at Intel, Soren Sharifi, was ever gently encouraging me to complete this work.

Steve Pytel and Jeff Tharpe of Ansys Corporation provided invaluable insight into the usage of Ansys HFSS. Steve Pytel often offered encouraging words. Witnessing his completion of the doctor of philosophy degree many years ago was my motivation to consider applying to the program.

The kind folks in Samtec's Glass Core Division made the attempt at a test apparatus on fused silica possible. I am grateful to Tim Mobley, Catie Eichhorn, Venkat Goli, Adam Owens, Ken Starzynski, and Nathan Robertson for the many iterations and final delivery of a measurable device.

I would not have moved past a few stuttering portions of my study without the guidance of my committee members Dr. Guoan Wang, Dr. Yinchao Chen, and especially Dr. Peng Ye. Dr. Ye consistently presented a possible path forward and a discerning eye when drawing conclusions from simulation results.

Dr. Paul Huray set me on a path for which I will always be grateful. A serendipitous visit during spring break in 2005 introduced me to signal integrity. His immediate and infectious joy at discussing electromagnetics was an ineluctable draw to the University of South Carolina program. It has been an honor to study under his guidance and debate topics that are foundational to the practicing industry. His direction throughout the course of my time at the University is something that I have often felt that I did not deserve but something that I will cherish. I hope to emulate a fraction of his zealous pursuit of knowledge.

My wife, Melissa Blackledge Gore, has always and continues to be a bedrock of support. Her forgone conclusion that I could complete this work inspired me when I doubted myself. She is the ideal life partner, and I love her dearly. I hope for many years and opportunities to give her equal levels of support.

Abstract

Modern baseband signaling that facilitates the passing of information over high speed interconnects such as copper twin-ax cable and printed circuit boards supports single line data rates of 100 Gbps. Next generation bandwidth requirements of electrical links are approaching frequencies up to 50 GHz. Yet, signal integrity engineers that analyze these interconnects rely on models with underlying assumptions and limited extensions beyond those proposed in the 19th century to describe per unit length characteristics of Resistance, Inductance, Conductance, and Capacitance (RLGC) for transatlantic telegraph cable. An excluded phenomenon is the time retarded behavior of electromagnetic fields.

The aim of this research is to quantify the impact of time retarded electromagnetic fields on the frequency dependent phase as described by the RLGC(p) model and applied to transmission line geometries encountered in printed circuit boards. Four areas of focus are pursued in this study. Applications of time retarded electromagnetic fields are examined with emphasis on velocity mismatch of the surface charge density above and below the signal conductor of a microstrip transmission line, and the loss mechanism of Cherenkov Radiation is newly applied to these electromagnetic waveguides. Simulation experiments are performed to validate that the analytical solutions to Jefimenko‘s equations are comprehended in a full wave EM solver. Design of a test apparatus for quantifying the time retardation impact to coupling of transmission lines on a Fused Silica substrate is presented. Finally, measurement attempts of this apparatus are discussed along with the challenges of metallization of thru glass vias and glass surfaces. Future research is proposed for Cherenkov Radi-

ation on microstrip transmission lines along with suggested experiments to perhaps visualize time retarded electromagnetic fields.

Preface

The motivation for much of this research is to continue the work presented in Dr. Peng Ye's doctoral dissertation, *Applying the Retarded Solutions of Electromagnetic Fields to Transmission Line RLGC Modeling*. The development of the RLGC(p) model and original discussion of frequency dependent phase is credited to Dr. Ye.

The convention used in this text for vector representation is to denote vector quantities with an arrow over the top of the symbol for the quantity. For example, electric field intensity $\vec{E}$.

Symbols for electric and magnetic field quantities are color coordinated in this text. Red font is used for related electric field quantities of electric surface charge density Σ_s, electric field intensity $\vec{E}$, electric flux density $\vec{D}$, scalar electric potential, and V. Blue font is used for related magnetic field quantities of current density $\vec{J}$, magnetic field intensity $\vec{H}$, magnetic flux density $\vec{B}$, and vector magnetic potential $\vec{A}$. By using colored symbols, Maxwell's equations are revealed even more beautifully symmetric.

Table of Contents

List of Tables

List of Figures

List of Symbols

t	Time at an observation point
t'	Time at a source point
x	Position at an observation point
$\vec{x}'$	Position at a source point
c	Velocity of light in free space
v	Velocity of light in a medium
v_p	Propagation velocity in a medium
$v(z,t)$	Voltage as a function of position and time
$i(z,t)$	Current as a function of position and time
Δz	Infinitesimal Length
Z_0	Characteristic Impedance
R	Resistance
L	Inductance
G	Conductance
C	Capacitance
$R_{p.u.l.}$	Resistance per unit length
$L_{p.u.l.}$	Inductance per unit length
$G_{p.u.l.}$	Conductance per unit length
$C_{p.u.l.}$	Capacitance per unit length
$Z_{p.u.l.}$	Impedance per unit length
$Y_{p.u.l.}$	Admittance per unit length
$RLGC$	Classic RLGC Model
$RLGC(p)$	RLGC Phase Model

$S21$	Insertion Loss Scattering Parameter
$S11$	Return Loss Scattering Parameter
λ	Electrical Wavelength
ϕ	Phase Angle
ϕ_{unwrap}	Unwrapped Phase Angle
f_c	Cutoff Frequency
k_c	Cutoff Wave Number
ω	Angular Frequency
γ	Propagation Constant
α	Attenuation Constant
β	Phase Constant
δ	Dirac Delta Function
$\vec{\nabla}\cdot$	Divergence Operator
$\vec{\nabla}^2$	Laplace Operator
$\vec{\nabla}\times$	Curl Operator
$[\ ]_{ret}$	Time Retarded Quantity
G_{ret}	Time Retarded Green's Function
ε_0	Permittivity of free space
ε_r	Relative Permittivity
μ_0	Permeability of free space
μ_r	Relative Permeability
$\vec{E}$	Electric Field Intensity
$\vec{D}$	Electric Flux Density
V	Electric Scalar Potential
Q	Electric Charge
q	Elementary Charge of a Proton
λ_l	Line Charge Density

Σ_s	Surface Charge Density
ρ_v	Volume Charge Density
$\vec{H}$	Magnetic Field Intensity
$\vec{B}$	Magnetic Flux Density
$\vec{A}$	Magnetic Vector Potential
$\vec{J}$	Electric Current Intensity

List of Abbreviations

ASJE	Analytically Solved Jefimenko‘s Equation
CAD	Computer Assisted Design
DUT	Device Under Test
DC	Direct Current
EMC	Electromagnetic Compatibility
ENIG	Electroless Nickel Immersion Gold
FEXT	Far End Crosstalk
FWTLT	Full Wave Transmission Line Theory
Gbps	Giga Bits Per Second
HFSS	High Frequency Structure Simulator
HPFS	High Purity Fused Silica
IFT	Inverse Fourier Transform
PEEC	Partial Element Equivalent Circuit
PEC	Perfect Electrical Conductor
PCB	Printed Circuit Board
SLE	Selective Laser Etching
SBR	Single Bit Response
TEM	Transverse Electric and Magnetic
TE	Transverse Electric
TM	Transverse Magnetic
TDR	Time Domain Reflectometry
TGV	Thru Glass Via

Chapter 1

Introduction

Printed circuit boards are defacto platforms in the electronics industry to mechanically support and electrically connect high frequency signaling devices. The electrical connections between transmitting devices and receiving devices are transmission lines which consists of conductive traces etched from copper sheets laminated together with dielectric substrates. Printed circuit transmission lines represent a majority of the signal degradation of an interconnect used for high frequency signaling; therefore, accurate modeling of transmission lines is an important part of signal integrity analysis.

There exists several techniques to model uniform transmission lines. A classical technique is the RLGC model and its augmentations. This model was originally introduced in the 19th century and contains many simplifying assumptions. The most notable exclusion for the purposes of this research is the effects of time retarded electromagnetic fields. A derivative of the RLGC was recently introduced to incorporate time retarded electromagnetic field effects. This model is named the RLGC(p) model [1].

Practicing signal integrity engineers are currently discovering the challenges of broadband signaling at data rates up to 56 Gbps (26 GHz). Traditionally, 2D numerical codes are chosen over analytical solutions [2] because of flexibility in solving transmission lines on printed circuit boards. However, these simulators often neglect time retarded field effects. Miniaturization of the transmission line geometry along with the signaling frequency increase has allowed the assumptions inherent in the classical RLGC model and 2D numerical simulators to remain less obvious. But, as data

rates and interconnect characterization approaches 100 GHz including the impact of time retardation on the performance of transmission lines becomes pertinent.

1.1 Historical Perspective for the Classical Transmission Line Model

The origins of describing signal propagation on a transmission line can be traced back to the transatlantic telegraph cable and the theoretical contributions by William Thomson and Oliver Heaviside [3].Failures to recover telegraph signals during the first attempts at transatlantic communication can, indeed, be referred to as the first signal integrity problem. It is important to recall challenges that were being faced and, more important, to understand the assumptions made during the development of the original transmission line theory - particularly - to keep in mind that Maxwell's equations were not yet published or refined.

The rapid deployment of submarine cable would have been a significant feat of engineering in the modern era let alone in the mid 19th century. There was a span of only seven years between the first cables laid in 1851 across the English Channel (at a length of 40 km and a depth of 30 fathoms) to the first successful transatlantic attempt reaching from Valentia, Ireland to Trinity Bay, Newfoundland (at a length 4074 km at depths ranging from 1700 to 2400 fathoms) [4].

Typical construction of submarine cable consisted of 6 copper wire conductors impregnated in an insulation of Gutta-Percha. Purity of the available copper yielded a conductivity of 85% that of pure copper. Gutta-percha is a vegetable gum thermoplastic and has the same chemical formulation as rubber (C_5H_8); however, it is rigid and does not react in water. This made it ideal for submarine applications [4]. The relative permittivity of Gutta-percha is $\varepsilon_r \approx 3.1$. The armouring of the cable was done with 12 to 18 strands of heavy iron wire. Figure 1.1 is a photo of cable sections from 1858 to 1866.

Figure 1.1: Cable Sections (Photo credit Atlantic-Cable.com)

First successful transatlantic telegraph communication was on August 17$^{\text{th}}$, 1858. Approximately 700 messages were achieved before cable failure, and the entire cable was abandoned only after three months [4]. An insufficient understanding of signal propagation led to the belief that a large voltage should be applied to the cable to overcome the long distance that the signal must travel; however, these large voltages resulted in catastrophic cable faults from insulator breakdown.

Professor William Thomson (later Lord Kelvin) put forth a theory of transmission line signal propagation in October 1854 to which George Stokes provided the general solution in November 1854 [5],[3]. For this theory, Professor Thomson simplified the geometry to that shown in Figure 1.2 which is similar to a co-axial cable. He

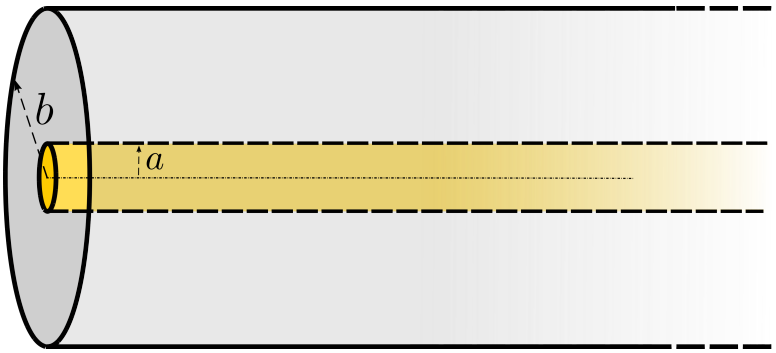

Figure 1.2: Illustration of Simplified Submarine Cable

was familiar with the thermal conduction theory of Joseph Fourier [5] and modeled

the voltage change versus position on the cable as a diffusion equation. Applying Kirchhoff's current law and Ohm's law to a infinitesimal length of cable, it is possible to show that the voltage v for a position x along the cable as

$$\frac{\partial^2 v}{\partial x^2} = KC\frac{\partial v}{\partial t} \tag{1.1}$$

For Equation 1.1, a resistance per unit length K of the wire is defined along with an "electrostatical capacity" per unit length as

$$C = \frac{2\pi\varepsilon}{ln(b/a)}$$

where the radius of the inner conductor is denoted as a and the radius of the outer conductor is denoted as b.

Equation 1.1 predicts the inter-symbol interference caused by the diffusing of the different frequency components contained within a single telegraph key stroke. It was not until 20 years later, in 1876, that Oliver Heaviside introduced an inductance per unit length S and derived the complete telegrapher‘s equation. Equation 1.2 allows for describing signal propagation as a wave. It also was the key to solving the inter-symbol interference plaguing transatlantic communication by introducing intentional faults (inductance) at particular positions along the line.

$$\frac{\partial^2 v}{\partial x^2} = KC\frac{\partial v}{\partial t} + SC\frac{\partial^2 v}{\partial t^2} \tag{1.2}$$

It is remarkable the usefulness and longevity of the telegrapher's equations given that they were derived by Oliver Heaviside assuming time independent fields and before he was familiar with James Clark Maxwell's theory of electromagnetism; the theory which he would make so much contribution over the next several years [3]. Even so, assumptions need to be made to assign physical meaning to the per unit length parameters introduced by William Thomson and Oliver Heaviside almost 150 years ago. Section 1.1 will review these assumptions and provide a derivation of the Classical RLGC Transmission Line model.

1.2 The Classical Transmission Line Model and Assumptions

It is often the case that the application of a particular modeled behavior is far removed from the theory and assumptions made during the development of said model. Such underlying assumptions, often made out of necessity, simplify the complexity of the solution, but errors in analysis are introduced as these assumptions are violated even incrementally. The subject of electrical analysis of transmission lines was once an entire course in undergraduate electrical engineering, but given a crowed curriculum the topic is only briefly covered, if at all [6]. This can only lead to potential misuse of analytical solutions or numerical tools designed to solve transmission line models.

Similar to Section 1, the Classical RLGC Transmission Line model seeks to represent the total characteristic parameters of resistance (R), inductance (L), conductance (G), and capacitance (C) of a transmission line of length l along the z axis by the infinite sum of distributed, infinitesimal lengths Δz of uniform cross-sections. These infinitesimal lengths are referred to as per unit length parameters where the unit is typically meters m. These parameters are defined in Table 1.1.

Table 1.1: Definition of per unit length RLGC Parameters

Parameter	**Definition**	**Unit**
Resistance per unit length ($R_{p.u.l.}$)	$\lim_{\Delta z \to 0} \frac{R}{\Delta z}$	Ω/m
Inductance per unit length ($L_{p.u.l.}$)	$\lim_{\Delta z \to 0} \frac{L}{\Delta z}$	H/m
Conductance per unit length ($G_{p.u.l.}$)	$\lim_{\Delta z \to 0} \frac{G}{\Delta z}$	S/m
Capacitance per unit length ($C_{p.u.l.}$)	$\lim_{\Delta z \to 0} \frac{C}{\Delta z}$	F/m

For the Classic RLGC Transmission Line model, physical geometry of the transmission line is used to calculate the distributed resistance, inductance, conductance,

and capacitance per unit length parameters. However, the physical meaning of these parameters is only valid for the static [time independent or direct current (dc)] case [6] where the Transverse Electric and Magnetic (TEM) mode is dominant. This is the fundamental assumption for the Classical RLGC Transmission Line model and requires that the lines be perfectly conducting ($\sigma = \infty$). To satisfy the boundary conditions on perfect electrical conductors (PEC), the behavior of the electric and magnetic fields surrounding the transmission lines are orthogonal to each other and have field components only in the plane perpendicular to propagation, the induced current is flowing along the line (in the z - direction), and the fields are uniquely defined [7]. An incremental modification to the fundamental assumption is made by including an additional resistance per unit length to account for the lines being imperfect conductors. This implicitly violates the assumptions of TEM mode and uniquely defined fields. If the resistance is kept small, the effect is ignored, and the solution is referred to as quasi-TEM [6]. Other assumptions include [8]:

- the cross-section of the lines are uniform along the line and small compared to the electrical wavelength λ
- the length of the line is long compared to the wavelength λ
- the surrounding medium is homogeneous
- an external source causes a cosinusoidal [e.g. $cos(\omega t)$ or $\mathrm{Re}(e^{-j\omega t})$] electric \ magnetic field in time on one of the conductors

Detailed derivation and exploration of the Classic RLGC Transmission line model including multiple conductors is the subject of many texts [9],[6],[10],[2]. The following derivation is similar to the treatment by Huray [8]. Figure 1.3 represents the voltage $v(z,t)$ and current $i(z,t)$ for an infinitesimal length Δz as function of the propagation distance z and as a function of characteristic parameters $R_{p.u.l.}$, $L_{p.u.l.}$,

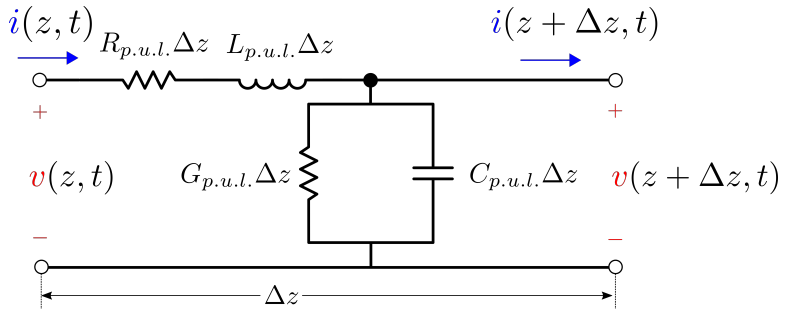

Figure 1.3: Schematic Representation of Infinitesimal Length RLGC Parameters

$G_{p.u.l.}$, and $C_{p.u.l.}$. Applying Kirchoff's voltage law then rearranging the equation obtains,

$$\begin{aligned} v(z+\Delta z,t) &= v(z,t) - R_{p.u.l.}\Delta z i(z,t) - L_{p.u.l.}\Delta z \frac{\partial i(z,t)}{\partial t} \\ \frac{v(z+\Delta z,t) - v(z,t)}{\Delta z} &= -R_{p.u.l.} i(z,t) - L_{p.u.l.}\frac{\partial i(z,t)}{\partial t} \end{aligned} \tag{1.3}$$

Taking the limit as $\Delta z \to 0$,

$$\frac{\partial v(z,t)}{\partial z} = -R_{p.u.l.} i(z,t) - L_{p.u.l.}\frac{\partial i(z,t)}{\partial t} \tag{1.4}$$

Then applying Kirchoff's current law in Figure at the node N obtains,

$$\begin{aligned} i(z+\Delta z,t) &= i(z,t) - G_{p.u.l.}\Delta z v(z+\Delta z,t,t) - C_{p.u.l.}\Delta z \frac{\partial v(z,t)}{\partial t} \\ \frac{i(z+\Delta z,t) - i(z,t)}{\Delta z} &= -G_{p.u.l.}\Delta z v(z+\Delta z,t,t) - C_{p.u.l.}\frac{\partial v(z,t)}{\partial t} \end{aligned} \tag{1.5}$$

Taking the limit as $\Delta z \to 0$,

$$\frac{\partial i(z,t)}{\partial z} = -G_{p.u.l.} v(z,t) - C_{p.u.l.}\frac{\partial v(z,t)}{\partial t} \tag{1.6}$$

Equations 1.4 and 1.6 are known as the transmission line equations. Assuming harmonic inputs,

$$v(z,t) = \mathrm{Re}[V(z)e^{j\omega t}] \tag{1.7}$$

$$i(z,t) = \mathrm{Re}[I(z)e^{j\omega t}] \tag{1.8}$$

the transmission line equations become two coupled, first-order, linear ordinary differential equations for phasor voltage $V(z)$ and phasor current $I(z)$,

$$\frac{dV(z)}{dz} = -R_{p.u.l.}I(z) - j\omega L_{p.u.l.}I(z) \tag{1.9}$$

$$\frac{dI(z)}{dz} = -G_{p.u.l.}V(z) - j\omega C_{p.u.l.}V(z) \tag{1.10}$$

These equations are uncoupled by taking a second spatial derivative and plugging back into Equations 1.9 and 1.10 to yield,

$$\frac{d^2V(z)}{dz^2} = \gamma^2 V(z) = \Big(R_{p.u.l.} + j\omega L_{p.u.l.}\Big)\Big(G_{p.u.l.} + j\omega C_{p.u.l.}\Big)V(z) \tag{1.11}$$

$$\frac{d^2I(z)}{dz^2} = \gamma^2 I(z) = \Big(R_{p.u.l.} + j\omega L_{p.u.l.}\Big)\Big(G_{p.u.l.} + j\omega C_{p.u.l.}\Big)I(z) \tag{1.12}$$

where γ is the propagation constant,

$$\gamma = \alpha + j\beta = \sqrt{\Big(R_{p.u.l.} + j\omega L_{p.u.l.}\Big)\Big(G_{p.u.l.} + j\omega C_{p.u.l.}\Big)} \tag{1.13}$$

Referring back to Figure 1.3, γ is also equal to $\sqrt{Z_{p.u.l.}Y_{p.u.l.}}$ where

$$Z_{p.u.l.} = R_{p.u.l.} + j\omega L_{p.u.l.} \text{ and } Y_{p.u.l.} = G_{p.u.l.} + j\omega C_{p.u.l.} \tag{1.14}$$

The solutions to Equations 1.11 and 1.12 are in form of the sum of propagating waves in the positive z-direction and negative z-direction,

$$V(z) = V_0^+ e^{-\gamma z} + V_0^- e^{\gamma z} \tag{1.15}$$

$$I(z) = I_0^+ e^{-\gamma z} + I_0^- e^{\gamma z} \tag{1.16}$$

If Equations 1.15 and 1.16 are put back into Equations 1.9 and 1.10 the resulting ratio of voltage to current obtains the characteristic impedance, Z_0:

$$Z_0 = \frac{V_0^+}{I_0^+} = \frac{\Big(R_{p.u.l.} + j\omega L_{p.u.l.}\Big)}{\gamma} = \sqrt{\frac{\Big(R_{p.u.l.} + j\omega L_{p.u.l.}\Big)}{\Big(G_{p.u.l.} + j\omega C_{p.u.l.}\Big)}} \tag{1.17}$$

1.3 Literature Review and State of the Art

An assumption of the Classical RLGC model of particular interest for this research is that the cross-sectional geometry be small compared to the wavelength λ. Small is generally thought to be between $\lambda/8$ and $\lambda/10$ [11],[12] with some evidence that wavelengths as small as $\lambda/40$ introduce non-TEM modes [6]. Extending the validity of the Classical RLGC model has been an active research subject [13],[14] particularly for electromagnetic compatibility (EMC) where large distances between wires introduce radiation effects even for single gigahertz frequency ranges. Such analytical models as the so-called full wave transmission line theory (FWTLT) [15] as well as the modified enhanced per unit length parameters [16] introduce complex valued $C_{p.u.l.}$ and $L_{p.u.l.}$ to account for radiation effects up to frequencies of several gigahertz. These models have been extended to multi-conductors with reasonable measurement to model correlation up to 3 GHz [11]. However, such proposed extensions are focused on frequency ranges that are considered low frequency for modern PCB design.

Another approach that is gaining popularity in the EMC field is the partial element equivalent circuit (PEEC) numerical method. This method models arbitrary three-dimensional interconnect structures by introducing circuit elements of controlled current and voltage sources to account for the electromagnetic behaviors of skin depth, dielectric losses, layered media, and time retardation between center to center conductors. A retardation factor is included by calculation of partial inductance and potential sources which is referred to as "lumped retardation". This retardation is frequency independent.[17]

Practicing signal integrity engineers designing at current data rates up to 56 Gbps (26 GHz) typically choose 2D numerical codes over analytical solutions [2]. Numerical codes provide flexibility in solving transmission lines on printed circuit boards. To overcome limitations of the Classical RLGC model, these codes have been modified to produce a tabular w-element models which are frequency dependent RLGC based

on dielectric dispersion in the medium [18]. Extra phase and power loss for copper surface roughness are also added to the tabular w-elements [19],[8].

1.4 Goals of this Research

This research aims to extend the work done during the development of the RLGC(p) model and visualization of time retarded electromagnetic fields [1]. As a result of experimentation with a 3D Full Wave Electromagnetic Simulator: ANSYS HFSS, Chapter 4 validates that similar results to analytical computations can be achieved and lays the ground work for analyzing multiple conductor transmission lines. Both extracted numerical data as well as field visualizations are compared between calculation methods.

Chapter 5 steps through the design and development of a test apparatus to quantify the impact of time retarded electromagnetic fields on a geometry similar to high frequency PCB transmission lines. Chapter 6 contains the measurement results of this test apparatus up to 67 GHz.

Chapter 3 explores applications of time retarded fields in a microstrip transmission line and contains speculations of loss mechanisms newly applied to transmission line analysis. Chapter 7 discusses potential future work to better visualize time retarded fields as well as ways to observe the loss mechanisms introduced in Chapter 3.

Chapter 2

Time Retarded Maxwell's Equations and the RLGC(p) Model

One of the most significant contributions to Natural Philosophy (the precursor to modern Physics) in the mid-19$^{\text{th}}$ century is the theory unifying the experimental investigations of Gauss, Faraday, and Ampere as well as the introduction of the displacement current by Scottish Mathematical Physicist James Clerk Maxwell in his 1873 *Treatise on Electricity and Magnetism*. This theory was subsequently codified into its current form and evangelized after Maxwell's early death at the age of 48 by such prominent 19$^{\text{th}}$ century scientists as Fitzgerald, Lodge, Hertz, and Heaviside [20]. The resulting Maxwell's equations have been the object of intense study and are the governing equations of Classical Electromagnetism. These equations exist in various forms all with the key aspect of relating Electric field intensity ($\vec{E}$), Magnetic field intensity ($\vec{H}$), Electric charge density (ρ_v), and Electric current density ($\vec{J}$) at a particular space-time, ($\vec{x}'$, t') [21]. The asymmetric forms of Maxwell's equations are given in Table 2.1.

In homogeneous media and time varying fields [7], the Electric flux density ($\vec{D}$) and Magnetic flux density ($\vec{B}$) are related by the constitutive quantities of permittivity (ε) and permeability (μ) as shown in equations:

$$\vec{E} = \varepsilon \vec{D}$$

$$\vec{H} = \mu \vec{B}$$

Table 2.1: Asymmetric Form of Maxwell's Equations

Differential Form	**Integral Form**	**Name**
$\vec{\nabla} \times \vec{E} = -\partial\vec{B}/\partial t$	$\oint_C \vec{E} \cdot d\vec{l} = -\iint_S \partial\vec{B}/\partial t \cdot d\vec{S}$	Faraday's Law
$\vec{\nabla} \times \vec{H} = \vec{J} + \partial\vec{D}/\partial t$	$\oint_C \vec{H} \cdot d\vec{l} = I + \iint_S \partial\vec{D}/\partial t \cdot d\vec{S}$	Ampere's Law
$\vec{\nabla} \cdot \vec{D} = \rho_v$	$\oiint_S \vec{D} \cdot d\vec{S} = Q$	Gauss' Law for Electric Charge
$\vec{\nabla} \cdot \vec{B} = 0$	$\oiint_S \vec{B} \cdot d\vec{S} = 0$	Gauss' Law for Magnetic Charge

2.1 Jefimenko's Equations

Electromagnetic fields propagate at a finite velocity; and thus, electromagnetic fields exhibit time retarded behavior. This behavior is, simply that, a time delay must elapse before a change in an electromagnetic condition at a point in space can yield an effect at another observation point. While this may be intuitive given the *principle of causality* which states that all present phenomena must be proceeded by past events [22], it has far reaching consequences for the classical theory of electromagnetic fields. Time retardation manifests in phenomena such as electromagnetic waves generated by oscillating electric charges and currents, electromagnetic fields of moving charge distributions, mechanical relations between time-dependent or moving charges and currents, dynamics of atomic systems, visual appearance of moving bodies, and even relativistic electrodynamics [23].

A simple illustration in Figure 2.1 compares the electrodynamic behavior with a simplified, subset condition: the electrostatic behavior. In Figure 2.1a, the electrodynamic source field intensities are described as $\vec{E}(\vec{x}', t')$ and $\vec{H}(\vec{x}', t')$ where the primed position $\vec{x}'$ and primed time t' denote the source point. The observation point is dis-

tinguished from the source point with the use of un-prime time and position:$\vec{E}(\vec{x},t)$ and $\vec{H}(\vec{x},t)$. The time delay can be described as $t-t' = |\vec{x}-\vec{x}'|/v$ with v being the propagation velocity in the medium. For the simplified condition of electrostatics

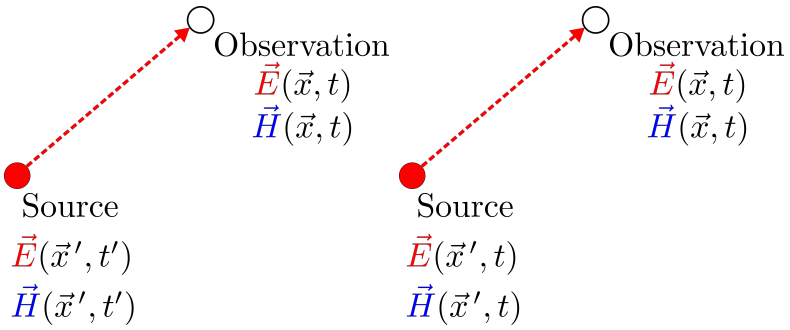

(a) Electrodynamic (b) Electrostatic

Figure 2.1: Illustrating Time Retardation

in Figure 2.1b, sources do not change with time; therefore, $\vec{E}(\vec{x}',t') = \vec{E}(\vec{x}',t)$ and $\vec{H}(\vec{x}',t') = \vec{H}(\vec{x}',t)$. Both the source and observation share the same time component so mathematically the propagation velocity is infinite, effects appear instantaneous, and time retardation is irrelevant [24]. Conversely for the electrodynamic condition, the time components t and t' are treated differently, the derivatives are more complex, and most notably t' is correlated to t, x, and $\vec{x}'$.

It can be argued that Maxwell's Equations in Table 2.1 do not represent causative relationships; therefore, $\vec{E}$ is not created by a time varying $\vec{B}$ or vice versa. Rather $\vec{E}$ and $\vec{H}$ are simultaneously created by the time varying charges and currents [22]. This is contrary to what is traditionally taught in Electrical Engineering texts.

Causal relations must contain retarded (previous time) quantities. These relations are a requirement to fully capture the dynamic effects of electromagnetic waves generated by oscillating electric charges and currents. Expressions for electromagnetic fields in terms of evident time retarded source quantities are referred to as Jefimenko's equations because of the author of the book where they first appeared [25].

The derivation of Jefimenko's equations can be pursued by several methods. A

common approach is to obtain the Liénard-Wiechert Retarded Potentials assuming the Lorenz gauge and calculate the electromagnetic field from the relations:

$$\vec{E} = -\vec{\nabla}V - {}^{\partial \vec{A}}\!/_{\partial t} \tag{2.1}$$

and

$$\vec{B} = \vec{\nabla} \times \vec{A} \tag{2.2}$$

where $\vec{A}$ is the magnetic vector potential and V is the electric scalar potential [26][27][7]. Another approach makes use of a Fourier transform in the temporal coordinate so to avoid complex and error prone manipulations with retarded quantities [28]. Yet another approach is to calculate directly from Maxwell's Equations with the use of the Retarded Green's function [25],[21],[29]. The following derivation will employ the Retarded Green's Function method [30].

The Asymmetric Maxwell's Equations in a vacuum are given by

$$\vec{\nabla} \times \vec{E} = -\frac{\partial \vec{B}}{\partial t} \tag{2.3}$$

$$\vec{\nabla} \times \vec{B} = \mu_0 \vec{J} + \mu_0 \varepsilon_0 \frac{\partial \vec{E}}{\partial t} \tag{2.4}$$

$$\vec{\nabla} \cdot \vec{E} = \frac{\rho_V}{\varepsilon_0} \tag{2.5}$$

$$\vec{\nabla} \cdot \vec{B} = 0 \tag{2.6}$$

Taking the curl of Faraday's Law and the time derivative of Ampere's Law yields

$$\left(\vec{\nabla}^2 - \frac{1}{c^2}\frac{\partial^2}{\partial t^2}\right)\vec{E} = -\frac{1}{\varepsilon_0}\left(- \nabla \rho_V - \frac{1}{c^2}\frac{\partial \vec{J}}{\partial t}\right) \tag{2.7}$$

Similarly, taking the curl of Ampere's Law and the time derivative of Faraday's Law yields

$$\left(\vec{\nabla}^2 - \frac{1}{c^2}\frac{\partial^2}{\partial t^2}\right)\vec{B} = -\mu_0 \vec{\nabla} \times \vec{J} \tag{2.8}$$

Solutions to Equations 2.7 and 2.8 are obtained from the Retarded Green's function $G_{ret}(\vec{x}, t; \vec{x}', t')$ which satisfies the inhomogeneous differential equation

$$\left(\vec{\nabla}^2 - \frac{1}{c^2}\frac{\partial^2}{\partial t^2}\right)G_{ret}(\vec{x}, t; \vec{x}', t') = -4\pi\delta(\vec{x} - \vec{x}')\delta(t - t') \tag{2.9}$$

The solution to Equation 2.9 is

$$G_{ret}(\vec{x},t;\vec{x}',t') = \frac{\delta(t'-(t-|\vec{x}-\vec{x}'|/c))}{|\vec{x}-\vec{x}'|} = \frac{\delta(t'-(t-R/c))}{R} \tag{2.10}$$

where $R \equiv |\vec{r}| = |\vec{x}-\vec{x}'|$. Using Equation 2.10, the solution to Equation 2.7 is written

$$\vec{E}(\vec{x},t) = \frac{1}{4\pi\varepsilon_0}\iiint d^3\vec{x}'\frac{\delta(t'-(t-R/c))}{R}\times\left\{-\vec{\nabla}'\rho_V(\vec{x}',t') - \frac{1}{c^2}\frac{\partial\vec{J}(\vec{x}',t')}{\partial t'}\right\} \tag{2.11}$$

$$= -\frac{1}{4\pi\varepsilon_0}\iiint d^3\vec{x}'\left\{\frac{[\vec{\nabla}'\rho_V]_{ret}}{R} - \frac{1}{c^2R}\left[\frac{\partial\vec{J}}{\partial t}\right]_{ret}\right\} \tag{2.12}$$

Here careful attention is needed because of the notation $[...]_{ret}$ which indicates that the quantities inside the brackets are evaluated at the source position $\vec{x}'$ and the retarded time $t' = t - |\vec{x}-\vec{x}'|/c$. Expanding $[\vec{\nabla}'\rho_V]_{ret}$ as

$$[\vec{\nabla}'\rho_V]_{ret} = \nabla'[\rho_V]_{ret} - \frac{\vec{r}}{c}\left[\frac{\partial\rho_V}{\partial t}\right]_{ret} \tag{2.13}$$

and substituting into Equation 2.12 the relation becomes

$$\vec{E}(\vec{x},t) = -\iiint d^3\vec{x}'\frac{\nabla'[\rho_V]_{ret}}{4\pi\varepsilon_0 R} + \iiint d^3\vec{x}'\frac{\vec{r}}{4\pi\varepsilon_0 cR}\left[\frac{\partial\rho_V}{\partial t}\right]_{ret} - \iiint d^3\vec{x}'\frac{1}{4\pi\varepsilon_0 c^2R}\left[\frac{\partial\vec{J}}{\partial t}\right]_{ret} \tag{2.14}$$

After integrating by parts and discarding surface terms because the charge distribution is localized, Jefimenko's Equation for the electric field intensity is given by

$$\vec{E}(\vec{x},t) = \frac{1}{4\pi\varepsilon_0}\iiint d^3\vec{x}'\left\{\frac{\vec{r}}{R^2}[\rho_V]_{ret} + \frac{\vec{r}}{cR}\left[\frac{\partial\rho_V}{\partial t}\right]_{ret} - \frac{1}{c^2R}\left[\frac{\partial\vec{J}}{\partial t}\right]_{ret}\right\} \tag{2.15}$$

Two important observations in Equation 2.15 are that it reduces to the static case for time independent fields, and the first term on the right hand side becomes Coulomb's Law. Coulomb's law is incomplete because it does not comprehend the

discoveries of the 19th century concerning the finite speed of light. To pursue this further, relations can be used [21] to transform Equation 2.15 to the Feynman expression for the electric field of a single point source

$$\vec{E} = \frac{q}{4\pi\varepsilon_0}\left\{ \left[\frac{\vec{r}}{R^2}\right]_{ret} + \frac{[R]_{ret}}{c}\frac{\partial}{\partial t}\left[\frac{\vec{r}}{R^2}\right]_{ret} + \frac{1}{c^2}\frac{\partial^2 [\vec{r}]_{ret}}{\partial t^2}\right\} \tag{2.16}$$

Feynman provides insight into time retardation in his explanation [31] of Equation 2.16. This explanation is quoted here to preserve the eloquent description of the beauty of nature and the power of mathematics. Several notations have been changed from the original text to match the form in Equation 2.16. These are denoted inside { }.

> *Take the first term, $\{\frac{q}{4\pi\varepsilon_0}\}$. That, of course, is Coulomb's law, which we already know: q is the charge that is producing the field; $\{[\vec{r}]_{ret}\}$ is the unit vector in the direction from the point P where $\vec{E}$ is measured, $\{R\}$ is the distance from P to q. But, Coulomb's law is wrong. (...) It is not correct that the first term is Coulomb's law, not only because it is not possible to know where the charge is now; and at what distance it is now, but also because the only thing that can affect the field at a given place and time is the behavior of the charges in the past. (...) So to allow for this time delay, we $\{$use $[R]_{ret}\}$, meaning how far away it was when the information now arriving at P left q. Just for a moment suppose that the charge carried a light, and that the light could only come to P at the speed c. Then when we look at q, we would not see where it is now, of course, but where it was at some earlier time. What appears in our formula is the apparent direction $\{[\vec{r}]_{ret}\}$ - the direction it used to be - the so-called retarded direction - and at the retarded distance $\{[R]_{ret}\}$. That would be easy enough to understand, too, but it is also wrong. The whole thing is much more complicated. There are several more terms.*

The next term is as though nature were trying to allow for the fact that the effect is retarded, if we might put it very crudely. It suggests that we should calculate the delayed Coulomb field and add a correction to it, which is its rate of change times the time delay that we use. Nature seems to be attempting to guess what the field at the present time is going to be, by taking the rate of change and multiplying by the time that is delayed. But we are not yet through. There is a third term - the second derivative, with respect to t, of the unit vector in the direction of the charge. Now the formula is finished, and that is all there is to the electric field from an arbitrarily moving charge.

For completeness in reviewing Jefimenko's equations, a derivation of Biot-Savart law for the magnetic field intensity follows. Again, the Retarded Green's Function in Equation 2.10 is employed to solve Equation 2.8 which gives

$$\vec{B}(\vec{x},t) = \frac{\mu_0}{4\pi R}\iiint d^3\vec{x}\,'\,[\vec{\nabla}\,' \times \vec{J}]_{ret} \tag{2.17}$$

and using the relation

$$[\vec{\nabla}\,' \times \vec{J}]_{ret} = \vec{\nabla}\,' \times [\vec{J}]_{ret} + \frac{\vec{r}}{c} \times \left[\frac{\partial \vec{J}}{\partial t}\right]_{ret} \tag{2.18}$$

then Equation 2.17 takes the form

$$\vec{B}(\vec{x},t) = \frac{1}{c}\int \frac{d\vec{x}\,'}{R}\vec{\nabla}\,' \times [\vec{J}]_{ret} - \frac{1}{c^2}\int d\vec{x}\,'\frac{\vec{r}}{R} \times \left[\frac{\partial \vec{J}}{\partial t}\right]_{ret} \tag{2.19}$$

Integrating by parts obtains

$$\begin{aligned}\vec{B}(\vec{x},t) = \frac{\mu_0}{4\pi}\iiint d^3\vec{x}\,'\vec{\nabla}\,' \times \left(\frac{[\vec{J}]_{ret}}{R}\right) + \\ \frac{\mu_0}{4\pi}\iiint d^3\vec{x}\,'\,[\vec{J}]_{ret} \times \vec{\nabla}\,'\left(\frac{1}{R}\right) - \\ \frac{1}{c}\iiint d^3\vec{x}\,'\frac{\vec{r}}{R} \times \left[\frac{\partial \vec{J}}{\partial t}\right]_{ret}\end{aligned} \tag{2.20}$$

After discarding the first term on the right-hand side of Equation 2.20 because the current distribution is localized in space, the relation $\vec{\nabla}'(1/R) = -\vec{r}/R^2$ is used to obtain

$$\vec{B}(\vec{x},t) = \frac{\mu_0}{4\pi}\iiint d^3\vec{x}'\left\{\frac{1}{R^2}\left([\vec{J}]_{ret}\times\vec{r}\right) + \frac{1}{cR}\left(\left[\frac{\partial\vec{J}}{\partial t}\right]_{ret}\times\vec{r}\right)\right\} \tag{2.21}$$

Equations 2.15 and 2.21 are Jefimenko's Equations for the Electric Field and Magnetic Field in a vacuum, respectively. Taking the Fourier transform and substituting $c = v$ where $v = c/\sqrt{\mu\varepsilon}$ is the propagation velocity in a medium yields the solutions in the frequency domain as given in Equations 2.22 and 2.23.

$$\vec{E}(\vec{x},\omega) = \frac{1}{4\pi\varepsilon_0}\iiint d^3\vec{x}'\left\{\frac{\vec{r}}{R^2}\left(1+j\frac{\omega R}{v}\right)\rho_V e^{-j\omega R/v} - j\frac{\omega}{v^2 R}\vec{J}\,e^{-j\omega R/v}\right\} \tag{2.22}$$

$$\vec{B}(\vec{x},\omega) = \frac{\mu_0}{4\pi}\iiint d^3\vec{x}'\left\{\frac{1}{R^2}\left(1+j\frac{\omega R}{v}\right)\left[\vec{J}\,e^{-j\omega R/v}\times\vec{r}\right]\right\} \tag{2.23}$$

2.2 RLGC(p) Model

In Section 1.1, the classic RLGC transmission line model is discussed along with the associated per unit length parameters $(R_{p.u.l.}, L_{p.u.l.}, G_{p.u.l.}, C_{p.u.l.})$ as well as the transmission line per unit length impedance $Z_{p.u.l.}$ and per unit length admittance $Y_{p.u.l.}$. In this section, the logic for the proposed [1],[24] RLGC(p) transmission line model is summarized.

The RLGC(p) model introduces frequency dependent phase $\phi(\omega)$ terms as a mechanism for incorporating the time retardation of the fields near a transmission line while retaining the *RLGC* form of the classic transmission line model. Table 2.2 contains both the Classic *RLGC* model and the RLGC(p) model.

A key feature of the RLGC(p) model is the addition of $\omega|L_{p.u.l.}\cdot\Delta z|\,sin\phi(\omega)$ and $|C_{p.u.l.}\cdot\Delta z|\,cos\phi(\omega)$ terms in the resistance (R) and conductance (G) parameters which

Table 2.2: Classic RLGC Model and the RLGC(p) Model

Parameter	**Classic RLGC Model**	**RLGC(p) Model**
Resistance (R)	$R_{p.u.l.} \cdot \Delta z$	$R_{p.u.l.} \cdot \Delta z - \omega \lvert L_{p.u.l.} \cdot \Delta z \rvert \, sin\phi(\omega)$
Inductance (L)	$L_{p.u.l.} \cdot \Delta z$	$\lvert L_{p.u.l.} \cdot \Delta z \rvert \, cos\phi(\omega)$
Conductance (G)	$G_{p.u.l.} \cdot \Delta z$	$G_{p.u.l.} \cdot \Delta z + \omega \lvert C_{p.u.l.} \cdot \Delta z \rvert \, sin\phi(\omega)$
Capacitance (C)	$C_{p.u.l.} \cdot \Delta z$	$\lvert C_{p.u.l.} \cdot \Delta z \rvert \, cos\phi(\omega)$

are the real portions of Z and Y. These terms are the same but opposite in polarity. As a consequence, one is the energy source and the other is the energy consumer rendering this model as energy neutral. This is important not only to conserve energy but to describe the time retardation phenomena where, for an instance in position, energy from the previous segment appears in the present segment [24].

Defining inductance and capacitance parameters in the RLGC(p) model uses the classic definitions of self-inductance and self-capacitance at a per unit length or infinitely small area Δz. Self-Inductance is the ratio of the total magnetic flux surrounding a segment to the current on that segment. This reduces to a line integral for a infinitely small area Δz at point O. The magnetic flux is calculated normal to the path, $\vec{B}_{y-total}$. Figure 2.2 illustrates the path of the line integral in Equation 2.24.

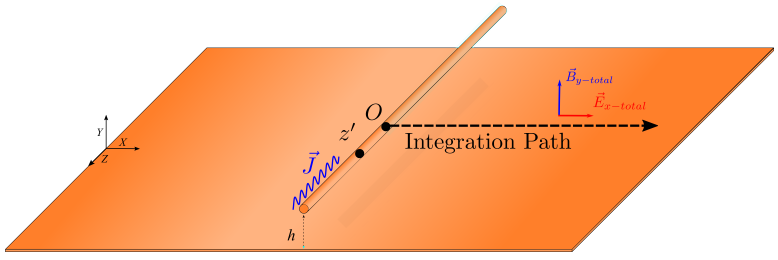

Figure 2.2: Illustration of Integration Path Chosen for Inductance and Capacitance

$$L_{p.u.l.} = \frac{1}{\vec{J}_O} \int_{path} \vec{B}_{y-total} \cdot d\vec{x} \tag{2.24}$$

Jefimenko's Equation 2.21 is used to solve for $\vec{B}_{y-total}$ and can be shown [1] to yield

$$L_{p.u.l.} = \frac{\mu}{4\pi} \int_a^{\infty} \int_{L_1}^{L_2} (x - x') e^{-jkz'} \left\{ \left(\frac{e^{-jkR}}{R^3} - \frac{e^{-jkR_{img}}}{R_{img}^3} \right) + jk \left(\frac{e^{-jkR}}{R^2} - \frac{e^{-jkR_{img}}}{R_{img}^2} \right) \right\} dz' dx' \tag{2.25}$$

where a is the radius of the wire, h is the height above the ground, L_1 and L_2 are the starting and ending location of the transmission line, and $k = \omega/v$. Additionally, R is the distance from the observation point to an integral segment, and R_{img} is the distance from the observation point to the mirror image. An image technique is used to assure that fields on the PEC are orthogonal to the reference plane.

Self-capacitance is the ratio of charge density Q to the voltage V where V is the path integral of electric intensity $\vec{E}$ between two points. For the RLGC(p), this path is selected to be the same as defined in Equation 2.24. Mathematically we have

$$C_{p.u.l.} = \frac{q_O}{\int_{path} \vec{E}_{x-total} \cdot d\vec{x}} \tag{2.26}$$

For $\vec{E}_{x-total}$, Jefimenko's Equation 2.15 is used and can be shown [1] to yield Equation 2.27 for the path shown in Figure

$$C_{p.u.l.} = \frac{4\pi\varepsilon}{\int_a^{\infty} \int_{L_1}^{L_2} (x - x') e^{-jkz'} \left\{ \left(\frac{e^{-jkR}}{R^3} - \frac{e^{-jkR_{img}}}{R_{img}^3} \right) + jk \left(\frac{e^{-jkR}}{R^2} - \frac{e^{-jkR_{img}}}{R_{img}^2} \right) \right\} dz' dx'} \tag{2.27}$$

It is notable that the path integration for $L_{p.u.l.}$ and $C_{p.u.l.}$ relies on path independence by only computing one path integral. This is a valid approach for time invariant fields; however, for the time varying fields that produce time retarded behavior this may not hold true. Computations for additional integration paths require the field calculations in Equations 2.25 and 2.27 to be reformulated. Another approach is to replace the various integrations by a fitting technique.

There is a common factor in Equations 2.25 and 2.27 which can be assumed to take the form of a complex solution. The resulting equation is

$$|P|e^{j\phi(\omega)} = \int_a^{\infty}\int_{L_1}^{L_2}(x-x')e^{-jkz'}\left\{\left(\frac{e^{-jkR}}{R^3}-\frac{e^{-jkR_{img}}}{R_{img}^3}\right)+jk\left(\frac{e^{-jkR}}{R^2}-\frac{e^{-jkR_{img}}}{R_{img}^2}\right)\right\}dz'dx' \tag{2.28}$$

By assuming the form in Equation 2.28, $C_{p.u.l.}$ and $L_{p.u.l.}$ become

$$L_{p.u.l.} = \frac{\mu}{4\pi}|P|e^{j\phi(\omega)} = |L_{p.u.l.}|e^{j\phi(\omega)} = |L_{p.u.l.}|cos\phi(\omega) + j|L_{p.u.l.}|sin\phi(\omega) \tag{2.29}$$

$$C_{p.u.l.} = \frac{4\pi\varepsilon}{|P|e^{j\phi(\omega)}} = |C_{p.u.l.}|e^{-j\phi(\omega)} = |C_{p.u.l.}|cos\phi(\omega) - j|C_{p.u.l.}|sin\phi(\omega) \tag{2.30}$$

Recalling from Section 1.1 that $Z_{p.u.l.} = R_{p.u.l.}+j\omega L_{p.u.l.}$ and $Y_{p.u.l.} = G_{p.u.l.}+j\omega C_{p.u.l.}$, the $Z_{p.u.l.}$ and $Y_{p.u.l.}$ become

$$Z_{p.u.l.} = R_{p.u.l} - \omega|L_{p.u.l.}|sin\phi(\omega) + j\omega|L_{p.u.l.}|cos\phi(\omega) \tag{2.31}$$

$$Y_{p.u.l.} = G_{p.u.l} + \omega|C_{p.u.l.}|sin\phi(\omega) - j\omega|C_{p.u.l.}|cos\phi(\omega) \tag{2.32}$$

Taking a similar definition as the Classical RLGC model, the Resistance per unit length $R_{p.u.l}$ and Conductance per unit length $G_{p.u.l}$ are defined as the real portion of $Z_{p.u.l.}$ and $Y_{p.u.l.}$, respectively. Therefore,

$$R_{p.u.l.} = real(Z_{p.u.l.}) = R_{p.u.l} - \omega|L_{p.u.l.}|sin\phi(\omega) \tag{2.33}$$

$$G_{p.u.l.} = real(Y_{p.u.l.}) = G_{p.u.l} + \omega|C_{p.u.l.}|sin\phi(\omega) \tag{2.34}$$

Summarizing the RLGC(p) per unit length parameters as

$$\text{Resistance Parameter} = R_{p.u.l.} - \omega|L_{p.u.l.}|\, sin\phi(\omega) \tag{2.35}$$

$$\text{Inductance Parameter} = |L_{p.u.l.}|\, cos\phi(\omega) \tag{2.36}$$

$$\text{Conductance Parameter} = G_{p.u.l.} + \omega|C_{p.u.l.}|\, sin\phi(\omega) \tag{2.37}$$

$$\text{Capacitance Parameter} = |C_{p.u.l.}|\, cos\phi(\omega) \tag{2.38}$$

For lossy mediums and low frequencies, the time retardation terms will be negligible and the real portion of the $R_{p.u.l.}$ and $G_{p.u.l.}$ parameters will overwhelm the imaginary portions of these parameters. For this special case, the RLGC(p) reduces to the classic RLGC model. However, for high frequencies and low losses where time retardation is significant, the RLGC(p) model can be used to correctly capture the time retarded behavior.

Chapter 3

Applications in Transmission Lines

This chapter introduces speculative concepts of time retarded electromagnetic fields as they propagate in a transmission line waveguide. The transmission line waveguide of interest is a common type used in printed circuit boards (PCB) consisting of a finite width, rectangular shaped signal conductor also referred to as a trace, that is supported by a dielectric medium and above a reference plane conductor. With the signal conductors printed on the external layers of a PCB, the region above the signal conductor is air. This type of transmission line is referred to as a microstrip; Figure 3.1 contains an illustration of this configuration.

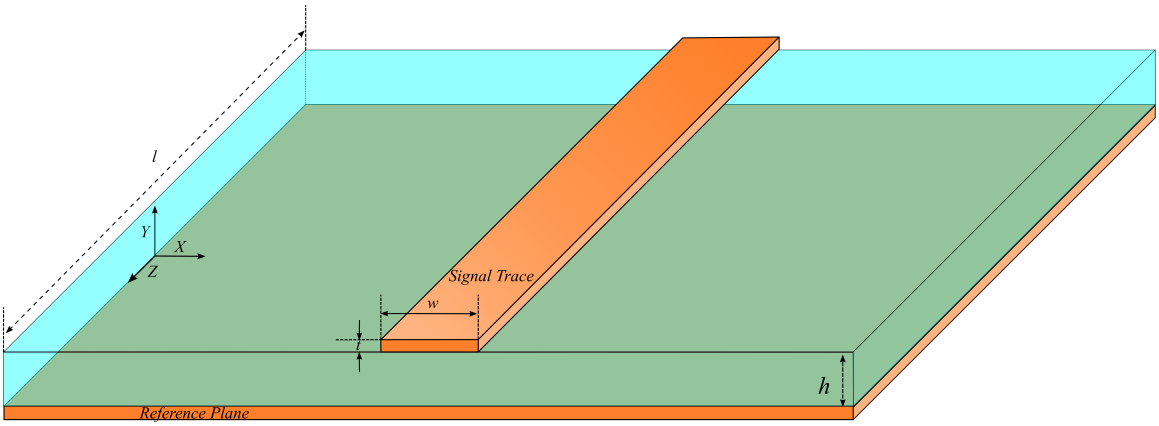

Figure 3.1: Idealized Microstrip Transmission Line

The air region supports the propagation of electromagnetic waves above the signal conductor and hence the surface charge density at the top boundary between the air and the signal conductor is roughly twice the velocity of the typical dielectric medium below the signal conductor. The faster surface charge density propagating in the air region will be referred to as a precursor to the slower surface charge density

propagating below the signal conductor in the dielectric region. In a lossless model, such a surface charge density on the top of the signal conductor and its accompanying electromagnetic wave above the trace should arrive at the receiving end of the transmission line in approximately half of the time before the surface charge density on the bottom side of the signal conductor. Such a precursor signal has not (to our knowledge) been previously observed. It is speculated that the above model is either highly lossy or incorrect in some other aspect.

In this Chapter, it is speculated that these precursors are of short, transient duration due to a loss mechanism newly applied in the context of transmission line: Cherenkov radiation. This loss mechanism is traditionally associated with isolated charged particles moving faster than the speed of light allowed in a medium. The surface charge density on the top of the signal conductor (the air side) can be thought of as a distribution of isolated charged particles whose complementary electromagnetic waves propagate in air at nearly the speed of light in a vacuum. The electromagnetic waves must connect to the below reference plane with a refraction discontinuity as they pass through the air-dielectric interface. The portion of the electric field lines inside the dielectric are restricted to propagate at approximately half the speed of light in a vacuum; therefore, they should exhibit Cherenkov type behavior in this region.

The Cherenkov shock wave front will be a violent and significant change in electric potential for a time equal to the width of the surface charge density pulse at those neutral atoms and molecules in the dielectric as the sequence of mach cone shock fronts move past them. The step function response of the dielectric medium to such potential changes was shown in Section 5.7 of Huray, *The Foundations of Signal Integrity* [8] and led to a wake of "Ringing dipoles" behind the potential shock wave as shown in Figure 5.34 of that text. Note that the frequency of oscillation of the"Ringing dipoles" is completely determined by the characteristics of atoms and

molecules in the dielectric material. Thus, if the dielectric material were water, the same visible blue glow associated with Cherenkov radiation in a spent reactor fuel pool would result. In another material, the frequency of the "Ringing dipoles" would be at some other frequency, perhaps not in the visible spectrum. Nonetheless, this potentially new loss mechanism for transmission lines is in addition to well explored loss mechanisms from surface roughness and dispersive dielectric mediums. Also, it should be emphasized that this would apply only to the surface charge density on top of the signal conductor since that is the origin of the *fast* electromagnetic waves that are produced in the dielectric material. How these *fast* Electric field lines determine, a priori, that they should refract at the air-dielectric interface or even how they know to become orthogonal to the reference plane is probably determined by quantum mechanical rules at extremely high velocities. One can even imagine that the electric field lines are like micro lightning bolts that initially search for a continuous path from the top of the signal conductor to the reference plane.

3.1 Assumptions

It is necessary to carefully state all fundamental assumptions that are made as concepts of time retarded fields in microstrip transmission lines are developed. The intent of the following subsections is to explicitly state the foundation for the exploration contained in the remainder the chapter.

3.1.1 Transmission Line Geometry Boundaries and Medium Characteristics

A homogenous dielectric is considered and is a necessary assumption for any analytic analysis employing static or transverse electromagnetic (TEM) fields such as the Classic RLGC model. However, the dielectric medium supporting PCB transmissions lines is far from homogeneous. It is an amalgam of epoxy resin impregnated with glass fabric and often includes voids, water, impurities, and other intentional inorganic

fillers [8]. These features of “real world” PCB dielectric mediums are neglected in the simulation of multi-layer PCB because of the difficulties quantifying and including these features in numerical simulators. Some exceptions are the macro scale effects of the glass fabric as a periodic medium [32],[33],[34] or the impact of skew on differential signaling [35],[36] which are analyzed and mitigated separate from transmission line simulation.

To ensure models of transmission lines exhibit causal behavior especially when creating Classic RLGC models, the dielectric medium is given a complex permittivity that is frequency dependent [18]; a common model for PCB dielectrics is the so called Djordjevic-Sarkar or Wide Band Debye model [37]. This frequency dependence results in signals that disperse or broaden as they propagate along the transmission line wave guide. The physical mechanisms for this frequency dependence of the permittivity are the various types of charges in the medium that move from equilibrium to produce electric dipole moments. Some examples of these dipole moments are permanent electric polar moments, induced electric dipoles, conduction electrons, and plasma elections [8]. To concentrate only on the exploration of time retardation as it applies to microstrip transmission lines, complex and frequency dependent permittivity will be ignored in this chapter.

Another approximation in this chapter is to treat the transmission line conducting surfaces as smooth with perfect model boundaries; again, this allows the isolation of the time retardation behavior of the fields. In actual manufactured microstrip transmission lines, edges are not rectangular, but more trapezoidal due to the acid etching and plating processes. Additionally, the surfaces of the conductors are intentionally roughened to promote adhesion and decrease the risk of delamination. Indeed, standards exists for "pull tests" to ensure the adhesion of external transmission lines are adequate [38]. Increasing the roughness is done by adding nodules or distributions of different sized, stacked spheres resembling snowballs [19]. This roughened surface

leads to a fractional power loss and a retarded current density that depends on the size and location of the conducting spheres. At the end of the transmission line, a pulse is dispersed as a result of surface roughness [8]. Other effects that are not included are: (1) the temperature of the dielectric molecules which will produce a Boltzmann distribution of excited states in the molecules prior to a electromagnetic shock wave and (2) the fact that the excitation of the propagating wave is not of the "lumped port" type used in most numerical simulations, but a non TEM^z type in which electric field intensity lines "lean" in the propagation direction from top to bottom (e.g. in Figure 3.10, page 41 as opposed to Figure 3.4, page 33) due to the finite propagation speed of the charge source from the transmitting device.

3.1.2 Validity of Maxwell's Equations

In Chapter 2, the asymmetric forms of Maxwell's Equations were assumed when deriving time retarded Electric field intensity ($\vec{E}$), and Magnetic field intensity ($\vec{H}$). These forms can be found as summarized previously in Table 2.1. An alternative approach would be to assume the symmetric form of Maxwell's Equations which requires including terms for Magnetic charge density and Magnetic current density. This is mathematically convenient when solving the inhomogeneous wave equations with boundary conditions chosen such as to separate transverse electromagnetic (TEM), transversion electric (TE), or transverse magnetic (TM) solutions [9]. However, the physics community assumes Magnetic charge density and magnetic current density do not exist; moreover, the approximation to include these terms and the resulting vector techniques are poor when considering fields in the near field [8]. For the purpose of this chapter, it is assumed that the asymmetric forms of Maxwell's Equations are valid at every point in time and are applicable at every location inside conductors, inside a medium, and in free space.

For the derivation of Jefimenko's equations, also known as time retarded Electric

field intensity ($\vec{E}$) and time retarded Magnetic field intensity ($\vec{H}$) in Chapter 2, the approach is chosen to calculate directly from Maxwell's Equations with the use of the Retarded Green's function. The more common approach is to obtain the Liénard-Wiechert Retarded Potentials provided in Equations 3.1 and 3.2 and then calculate the electromagnetic field from the relations $\vec{E} = -\vec{\nabla}V - {}^{\partial \vec{A}}/_{\partial t}$ and $\vec{B} = \vec{\nabla} \times \vec{A}$ where $\vec{A}$ is the magnetic vector potential and V is the electric scalar potential.

$$V(R,t) = \frac{1}{4\pi\varepsilon} \iiint d^3\vec{x}' \frac{\rho_V(t - R/c)}{R} \tag{3.1}$$

$$\vec{A}(R,t) = \frac{\mu}{4\pi} \iiint d^3\vec{x}' \frac{\vec{J}(t - R/c)}{R} \tag{3.2}$$

Liénard-Wiechert Retarded Potentials are solutions to the inhomogeneous wave equations for $\vec{A}$ and V by using the Fourier transform of Green's Function to obtain the Retarded Green's function [8]. These inhomogeneous wave equations are written below in Equations 3.3 and 3.4. They are second order partial differential equations (PDEs) for V and $\vec{A}$ which were uncoupled by assuming an additional restriction of the Lorenz Gauge $\vec{\nabla} \cdot \vec{A} - {}^{\partial V}/_{\partial t} = 0$.

$$\left(\vec{\nabla}^2 - \mu\varepsilon \frac{\partial^2}{\partial t^2}\right) V = -\frac{\rho_V}{\varepsilon} \tag{3.3}$$

$$\left(\vec{\nabla}^2 - \mu\varepsilon \frac{\partial^2}{\partial t^2}\right) \vec{A} = -\mu\vec{J} \tag{3.4}$$

If another gauge or restriction is assumed e.g. the Coulomb Gauge, different scalar electric potential and magnetic vector potential are obtained [8].

3.1.3 $\vec{E}$ and $\vec{H}$ Field Intensity-Charge Coexistence

Time dependent Electric field intensity $\vec{E}$ and Magnetic field intensity $\vec{H}$ coexist and radiate from sources as they propagate as waves in space. Thus, a volume of electric charge densities ρ_V can be thought of as producing $\vec{E}$. Moving charges

then constitute a current density $\vec{J}$ that induces $\vec{H}$. However, it can be shown [8] that to satisfy boundary conditions at a conducting surface, it is required that an electric surface charge density Σ_s distribution exist to support electric and magnetic fields. Since conduction electrons do not travel at velocities comparable with those of electromagnetic fields in a medium, it is argued [7] that surface charge densities rather than conduction electrons satisfy conductor/insulator boundary conditions. A field-charge density is therefore assumed to exist at these boundaries so that it is equivalent for fields to induce charges or charges to induce fields[8]. Physicists often call these charge densities Surface Plasmons.

3.1.4 Transverse Wave of Charges on the Conductor Surface

A medium such as the dielectric region of a microstrip transmission line supports a propagation velocity $v_p = c/\sqrt{\mu\varepsilon}$ in the direction $\hat{z}$ for the electromagnetic fields. The induced surface charge density needed to satisfy Gauss's law at the conducting boundary is $\Sigma_s = \varepsilon \vec{E}_y$. A linear current density $\vec{J}$ is formed from this surface charge density as it propagates at the velocity of the medium [8]. This current density is $\vec{J} = v_p \Sigma_s \hat{z}$.

Assuming a permittivity similar to traditional PCB of $\varepsilon_r = 4$, the propagation velocity is approximately $v_p = c/2 = 1.5 \times 10^8$ m/s which is two orders of magnitude greater than the Fermi velocity of conduction electrons in copper: 1.57×10^6 m/s. As explained by Pippard [39], the propagating surface charge density is not a longitudinal movement of conduction electrons, but rather a transverse displacement of the "free" electron cloud from their ion cores of only a fraction of a nuclear dimension is needed to produce the required surface charge density Σ_s [8].

Figure 3.2 illustrates this transverse displacement of conduction electrons for a cosinusoidally varying surface charge wave in sync with the electromagnetic field intensity. Magnetic field intensity lines are shown as blue arrows in and out of the

page.

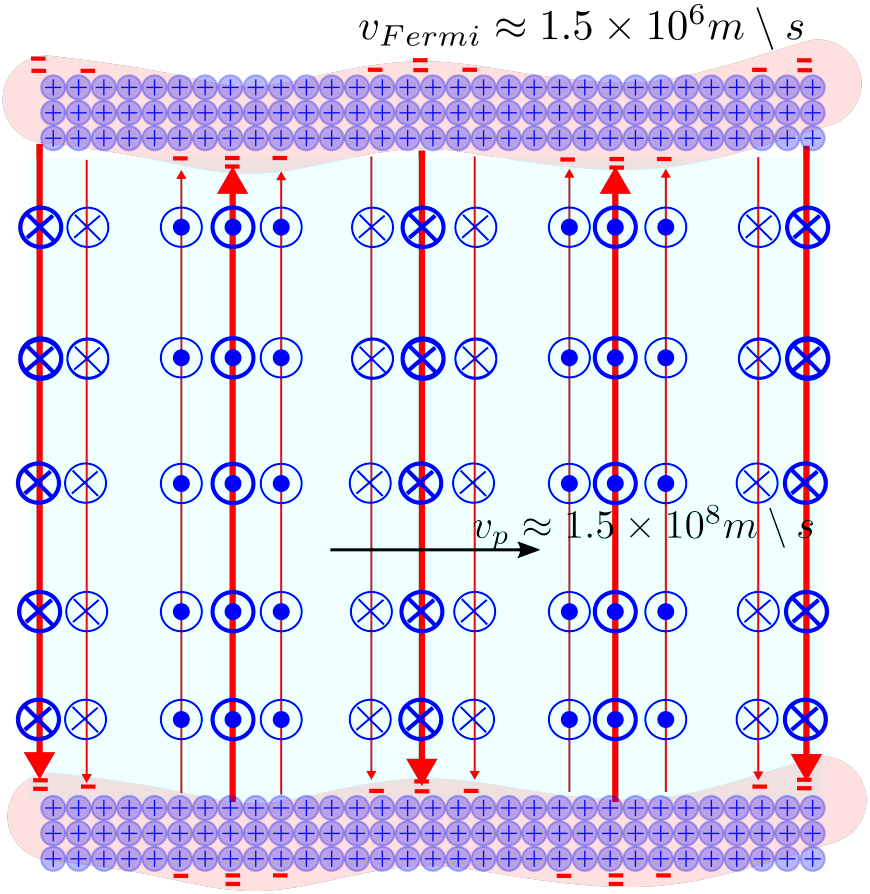

Figure 3.2: Transverse Displacement of Conduction Electron to Support Surface Charge Density

3.2 Static Field Analysis for a Microstrip Transmission Line

For understanding conceptual behavior of fields, static field analysis can be applied to transmission line waveguides and microstrip transmission lines in particular by enforcing several approximations. The first is to assume perfect electric conductors which have boundary conditions that require the electric field intensities to be normal to the conducting surfaces and the magnetic field intensity to be tangent to the conducting surfaces [6]. Another simplification often employed is to treat the two separate regions of air and dielectric as one effective region [10]. The resulting propagation mode is referred to as quasi-TEM to denote the use of approximations. Such

a propagation mode is assumed when deriving the Telegrapher‘s equations and the Classic RLGC model as in Section 1.1.

For the TEM^z mode of propagation, no electric field component exists in the direction of propagation $\hat{z}$. Additionally, a voltage can be uniquely defined (i.e. path independent) between the signal conductor and a reference plane since there is an evenly distributed scalar potential and a conservative electric field intensity [6]. Equation 3.5 defines this unique voltage along the path $d\vec{l}$ between P' and P where P' is located on the signal conductor and point P is located on the reference plane.

$$V(z,t) = -\int_{P\prime}^{P} \vec{E}_y \cdot d\vec{l} \tag{3.5}$$

Similarly, a unique current can be defined by integrating the Magnetic field intensity around a closed path encompassing the signal trace. Without a component of the electric field in the propagation direction, no displacement current $\partial\vec{D}/\partial t$ exists and the current is equivalent to the static condition of Ampere‘s law. Equation 3.6 contains the mathematical description of Ampere‘s law in the static condition.

$$I(z,t) = \oint_C \vec{H}_x \cdot d\vec{l} \tag{3.6}$$

Figure 3.3 depicts the end view of a microstrip transmission line with field lines drawn to illustrate the Electric and Magnetic field intensities for the TEM^z mode of propagation. Fringing fields have been ignored in this graphic under the assumption that a shapshot of the Electric field intensity is seen at the signal end of a microstrip transmission line, and that it will gradually fringe out over time as the surface charge density propagates toward the receiver end of the microstrip transmission line. Note (as explained at the end of Section 3.1.1) that this assumption is likely not rigorously valid since a signal charge created by an integrated circuit will likely appear on the signal conductor and then take some time to reach the reference plane. Nevertheless, this “lumped” port excitation is one of the two ways traditionally used to excite a numerical simulator (the other being a wave port configuration which will

better match the electromagnetic field distributions as a signal propagates from one conductor to another). It is noted that the boundary value problems of a microstrip with two distinct regions as well as the fringing fields due to the finite conductor width is difficult to solve analytically and is usually left to numerical simulators [8]. Simple illustrations of the field lines are thus a tool to aid in the understanding of propagating electromagnetic field behavior.

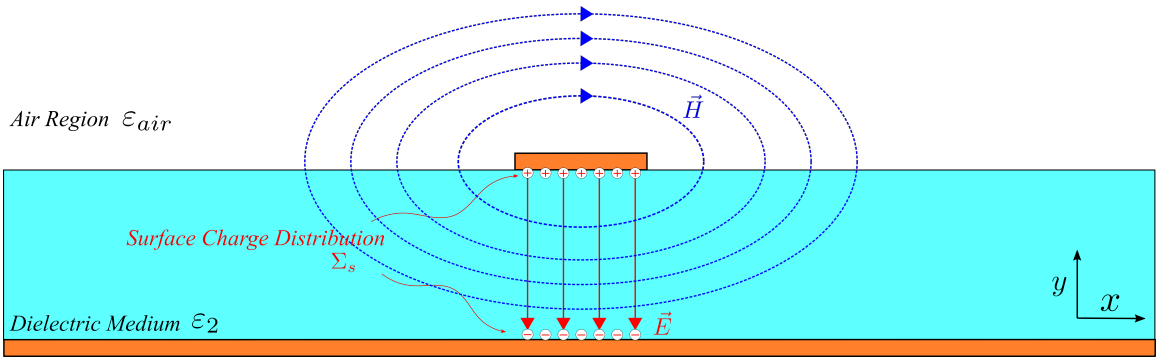

Figure 3.3: End View of a Microstrip with Field Lines Illustrated for Transverse Electromagnetic Magnetic (TEM) Propagation with Fringing Fields Ignored

3.3 Pulse Propagation Along a Microstrip Transmission Line

Visualization of a voltage pulse as it propagates along a transmission line is also of interest for high speed interconnect design. A common simulation technique for interconnect channel evaluation is to convolve the pulse response, also referred to as the single bit response (SBR), with a bit pattern to determine the resulting eye diagram or other channel performance metrics [40]. Therefore, understanding the behavior of a pulse interacting with a single transmission line lends insight to the expected outcome of simulated responses. In the following sections, several instances of a pulse propagating as it is guided along a microstrip transmission line will be explored. For the initial set of visualizations, the field lines are drawn as depicted in the TEM^z mode, i.e. from a "lumped" port excitation, of Figure 3.3. Here, the transmission line is viewed from the side or yz plane as the pulse moves along

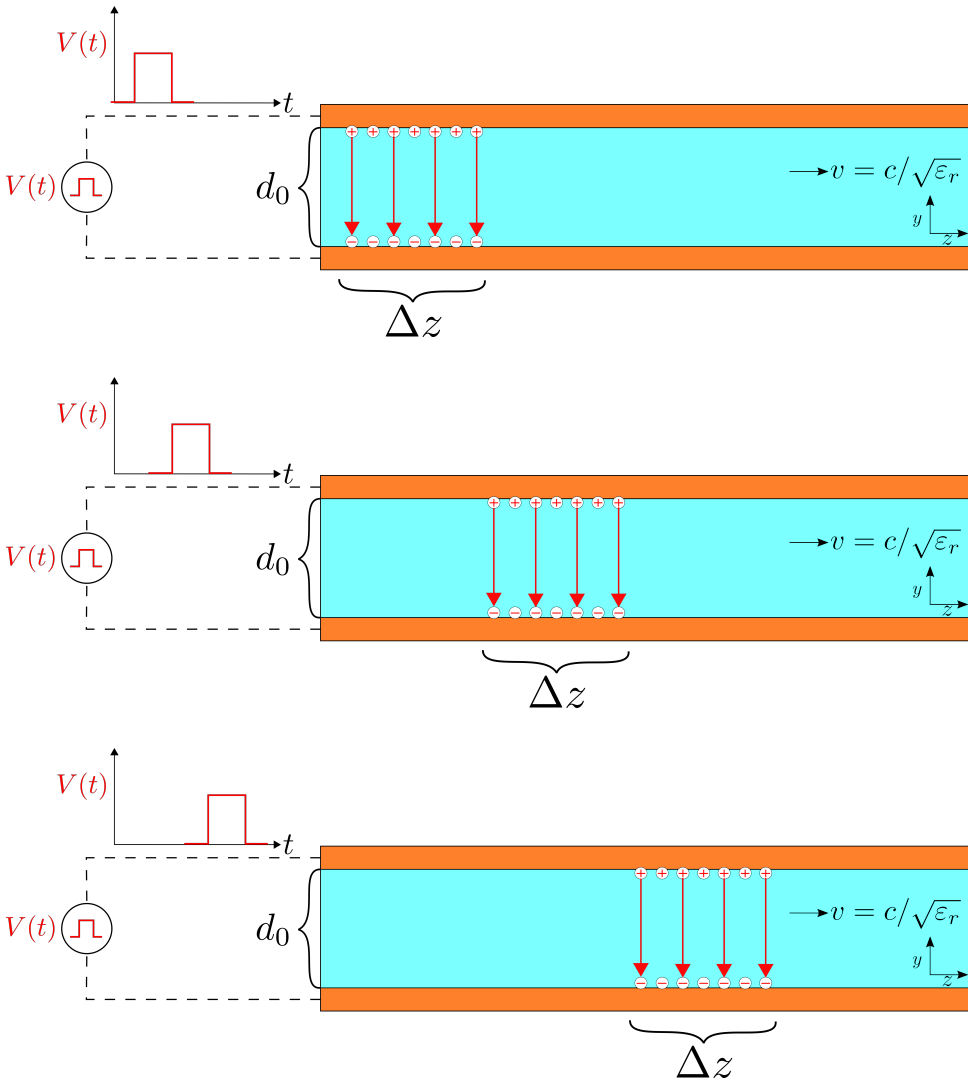

Figure 3.4: Pulse Propagation Assuming Static Electric Field Lines

the transmission line in the z-direction. Consecutive frames in Figure 3.4 represent snapshots of increasing time t as the pulse propagates at a velocity $v_p = c/\sqrt{\varepsilon_r}$. The pulse has a finite width denoted Δz, and the signal conductor and reference conductor are separated by the distance d_o. For these illustrations, the surface charge density Σ_s is confined to the region with relative permittivity, $\varepsilon_r = 4$. When viewed in this configuration, the pulse is likened to a moving parallel plate capacitor.

3.3.1 Relativistically Moving Parallel Plate Capacitor

In his book *Electromagnetic Retardation and Theory of Relativity*, Jefimenko suggests an equivalence between relativistic field transformations and time retarded electromagnetic fields. The Lorentz transformations are derived from both time retarded Electric field intensity and time retarded Magnetic field intensity for several charge distributions. He emphatically states that:"[. . .]we hardly have any choice but to conclude that the relativistically correct visual shape of a moving body is its retarded shape" [23].

Jefimenko evaluates a moving parallel plate capacitor by use of the Lorentz operator γ which transforms field quantities between stationary and moving reference frames. In this analysis, the capacitor plates are assumed to be thin and the separation between the plates is small. These assumptions preclude an electrically significant distance between the plates; therefore, time retardation between plates is ignored. Jefimenko concludes that the electromagnetic fields of a stationary capacitor are the same as those in a moving capacitor [23]. He did not consider a moving parallel plate capacitor with significant distance between the plates. This solution is assumed to be too difficult for analytical analysis.

3.3.2 Charge Dilation from Retardation

In his book *Causality, Electromagnetic Induction, and Gravitation*, Jefimenko relates electromagnetic equations for fields in a vacuum with gravitation field equations. This includes isolated charge, surface charge density, and volume charge density with their gravitational counterparts of mass, surface mass density, and volume mass density [22]. Just as an object moving at relativistic speeds appears to increase in mass to a stationary observer [31], charge and current density moving at relativistic speeds dilate according to the Lorentz-Einstein transformations [23]. As discussed in the previous section, either relativistic field transformations or time retarded electromag-

netic field equations yield the same descriptions of field quantities.

Jefimenko examines the Electric and Magnetic field intensities resulting from a uniformly moving charge distribution. He concludes that the projected length, shape, and thickness of the front and back of the charge distribution are not the same as the stationary charge distribution. The effective length of the charge distribution is greater than the stationary length. Further, only the leading and trailing ends of the charge distribution contribute to the electromagnetic fields at future projected positions [23]. Superposition of electric fields at previous positions create contour curves that lengthen in the direction perpendicular to motion as velocity increases [22]. The resulting field lines bend away from the source charge and are represented as elliptic in subsequent sections.

3.4 Time Retarded Fields in a Microstrip Transmission Line

Continuing the discussion of a pulse propagating along a microstrip transmission line, the surface charge density is assumed to be present on both the top and bottom of an infinitesimally thin signal conductor. The influence of the reference plane is ignored for the following visualizations. This is represented by a reference conductor that is less transparent in color compared to the signal conductor. Surface charge density that propagates on the top of the conductor is surrounded by air which has a relative permittivity near unity ($\varepsilon_r \sim 1$) and supports a propagation velocity v_p near the speed of light, c. Surface charge density that propagates on the bottom of the conductor is surrounded by a medium with a relative permittivity of four ($\varepsilon_r = 4$) and supports a propagation velocity one-half the speed of light $v_p = c/2$.

3.4.1 Charge Density on Bottom of the Conductor

In this section, surface charge density is assumed only on the bottom of the signal conductor and confined to the medium below. The separation between the conductors

is enough to ignore the influence of the reference plane. Electromagnetic fields are in regions both above and below the signal conductor and are propagating at the same velocity as the surface charge density in the medium below the signal conductor $v_p = c/2$. Consecutive frames in Figure 3.5 represent snapshots of increasing time t as the pulse propagates at a velocity $v_p = c/\sqrt{\varepsilon_r}$.

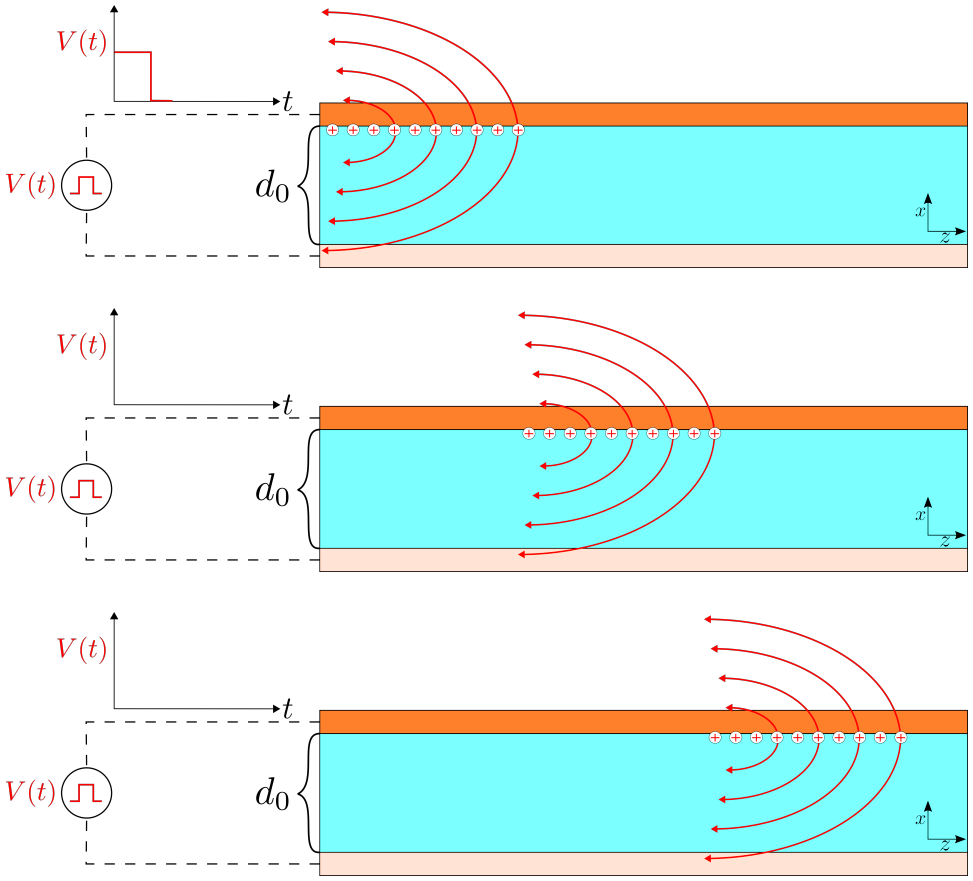

Figure 3.5: Pulse Propagation Assuming only Surface Charge Density on the Bottom of the Conductor

When a reference plane is present below the signal conductor, electromagnetic waves must connect to the reference conductor and surface charges are induced on the lower conductor. Boundary conditions near the conductor require that the electric field lines to be perpendicular to the surface. When the separation between conductors, d_0, is small enough for time retarded electromagnetic fields to be signifi-

cant there must exist a transition region between electric field lines from the surface charge density on the signal conductor and electric field lines from the surface charge density on the reference conductor. Figure 3.6 illustrates this as superimposed elliptical Electric field lines from the signal conductor and normal Electric field lines on the reference conductor. Given there is a time delay associated with the induced surface charge density on the reference conductor, the superposition of delayed Electric field lines may be more appropriate. This would facilitate a reflected but lagging electric field in the wake of the pulse.

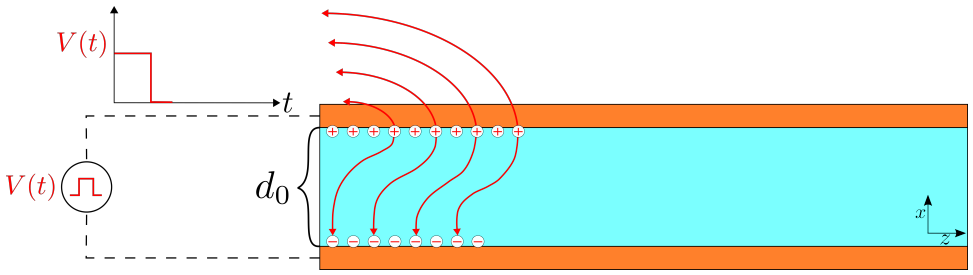

Figure 3.6: Influence of a Reference Plane to the Field Lines

3.4.2 Charge Density on Top of the Conductor

In this section, surface charge density is assumed only on the top of the signal conductor. Electromagnetic fields are in both regions above and below the signal conductor. The Electric fields lines associated surface charge density are propagating at the same velocity supported by the air region above the signal conductor ($v_p = c$). However, in the region below the signal conductor, the velocity of propagation is roughly one-half that supported above the conductor. It is speculated that the surface charge density propagates faster than what is supported by the medium, and this meets the criteria for Cherenkov radiation.

Cherenkov radiation is a characteristic light emitted when a charged particle travels faster than the phase velocity in a medium (often blue light if the medium is water) [21],[41]. It is the reason that underwater nuclear reactors give off a blue glow and

was first observed by Pavel Cherenkov in 1934 when a bottle of water was exposed to emitted charged particles in radioactive decay [42]. On a macroscopic level, the charged particle is often described as emitting the radiation; however, the reason for the emission is that nearby medium atoms or molecules experience a shock wave of electromagnetic potentials due to the fast moving charged particles [41]. This radiation that results is thus fluorescence or relaxation of the medium atoms or molecules as they lose energy following a violent induced dipole moment. The wavelength of the observed radiation is thus due to the time dependent relaxation of the neutral atoms and/or molecules in the medium that were induced by the motion of the charged particle and its shock wave (Mach Cone) of electromagnetic potential. Figure 3.7

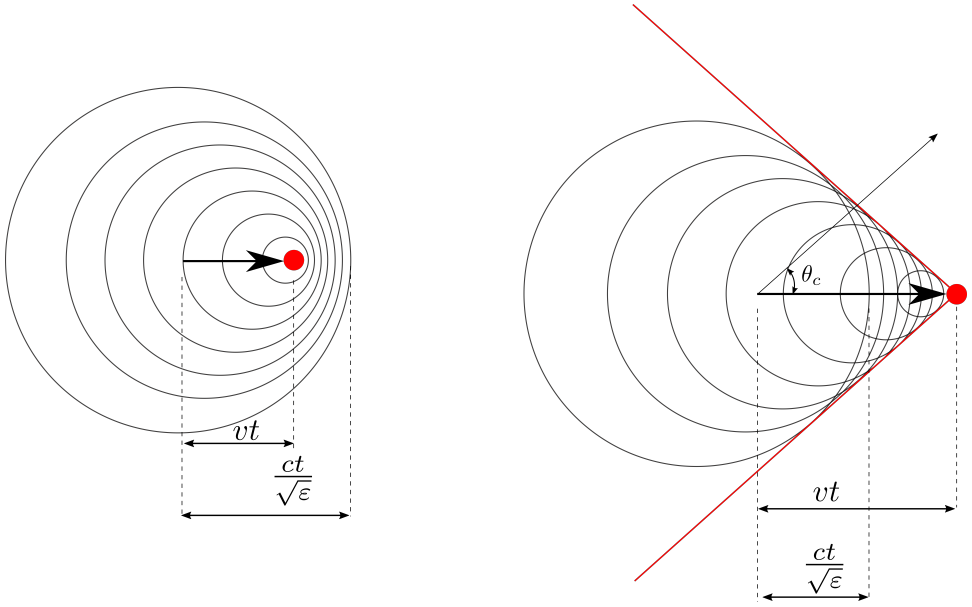

Figure 3.7: Charged Particle at Different Velocities

contains the spherical fields of a particle traveling at a velocities both less than and greater than the velocity of light in the medium. When the velocity of propagation is less than the speed of light supported in the medium, the spherical fields are the same as represented by Jefimenko's Figure A5.3 [22]. When the velocity of propagation is greater than that of light in the medium (at right of Figure 3.7), an electromagnetic shock front is created by the instantaneous positions of the retarded particle

movements and likened to a sonic boom produced by sound waves [21].

Inside the "Mach Cone", the electromagnetic potential and therefore electric field lines are bunched along the wavefront. Outside this cone, no potentials or electromagnetic fields exist. An unpolarized atom or molecule with no electric dipole would then experience a sudden electromagnetic potential shock wave as the charged particles pass by (sometimes called the wake of the potentials). At some later time, the atom or molecule would return to its previous state. Figure 3.8 depicts a single charged particle passing two neutral atoms along with a third atom who's nucleus is displaced to depict an induced dipole. Some artistic liberties are taken in depicting the displacement of the nucleus of the neutral atom in the direction perpendicular to the charged particle. It more likely that the dipole is induced in the direction normal to the Mach Cone line of potentials. Inducing a dipole in that direction would excite rotational modes if they are present in a molecule e.g. water molecules.

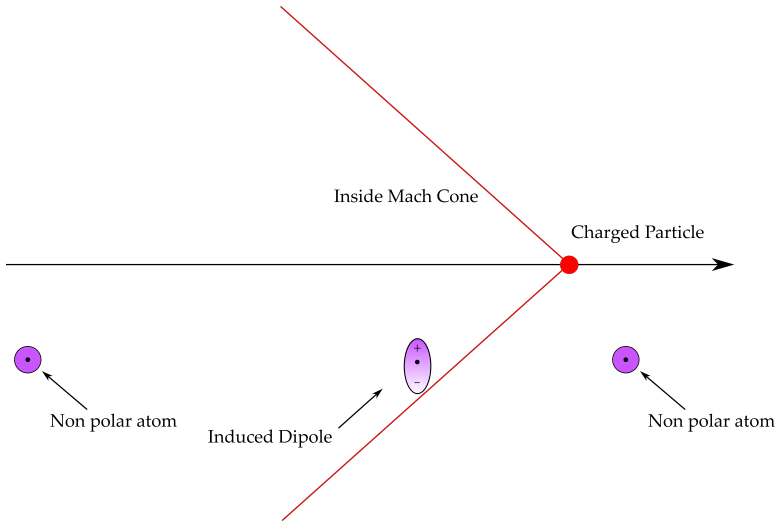

Figure 3.8: Three Neutral Atoms Passed by a Single Charged Particle's Shock Wave Potential

Figure 3.9 illustrates subsequent shock waves from an increasing number of charged particles. A sequence of three charged particles are shown in Figure 3.9a and the dipole displacement is enhanced compared to the dipole in Figure 3.8. Figure 3.9b illustrates N number of charged particles with a width denoted by the grey region

bounded by the fore and trailing charged particle. The dipole displacement is now enhanced to its maximum displacement. The degree of polarization grows while the molecule is in the shaded grey area.

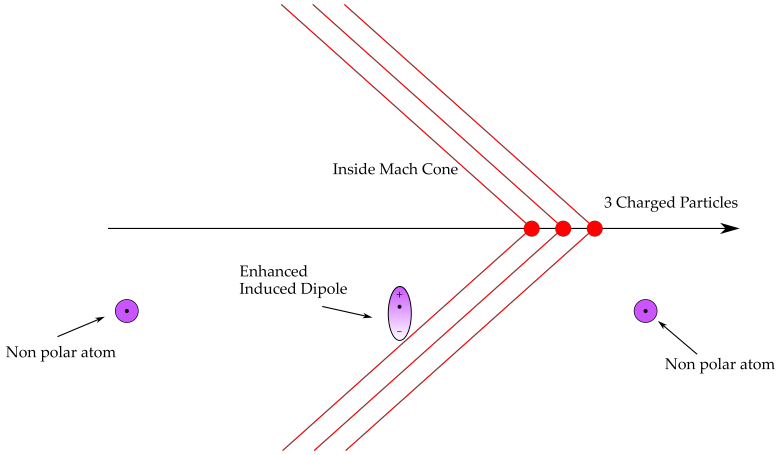

(a) Three Charged Particles

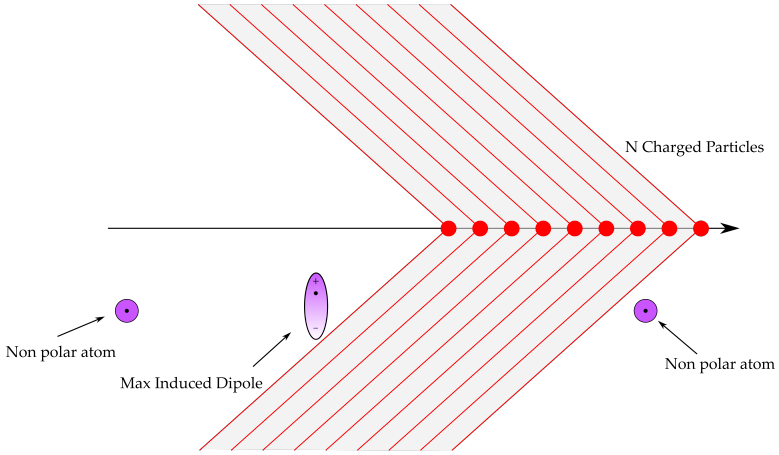

(b) N Charged Particles

Figure 3.9: A Sequence of Three Charged Particles and N Charged Particles

To illustrate how surface charge density may propagate only on the top surface of the signal conductor, consecutive frames in Figure 3.10 represent snapshots of increasing time t as the voltage pulse propagates at a velocity $v_p = c$. In the air region, the electric field lines are elliptical and representative of time retarded electric field intensity. In the region below the signal conductor, the field lines are swept back at an angle θ representing the potential shock wave that causes Cherenkov radiation. In subsequent frames, the surface charge density as well as the electromagnetic field

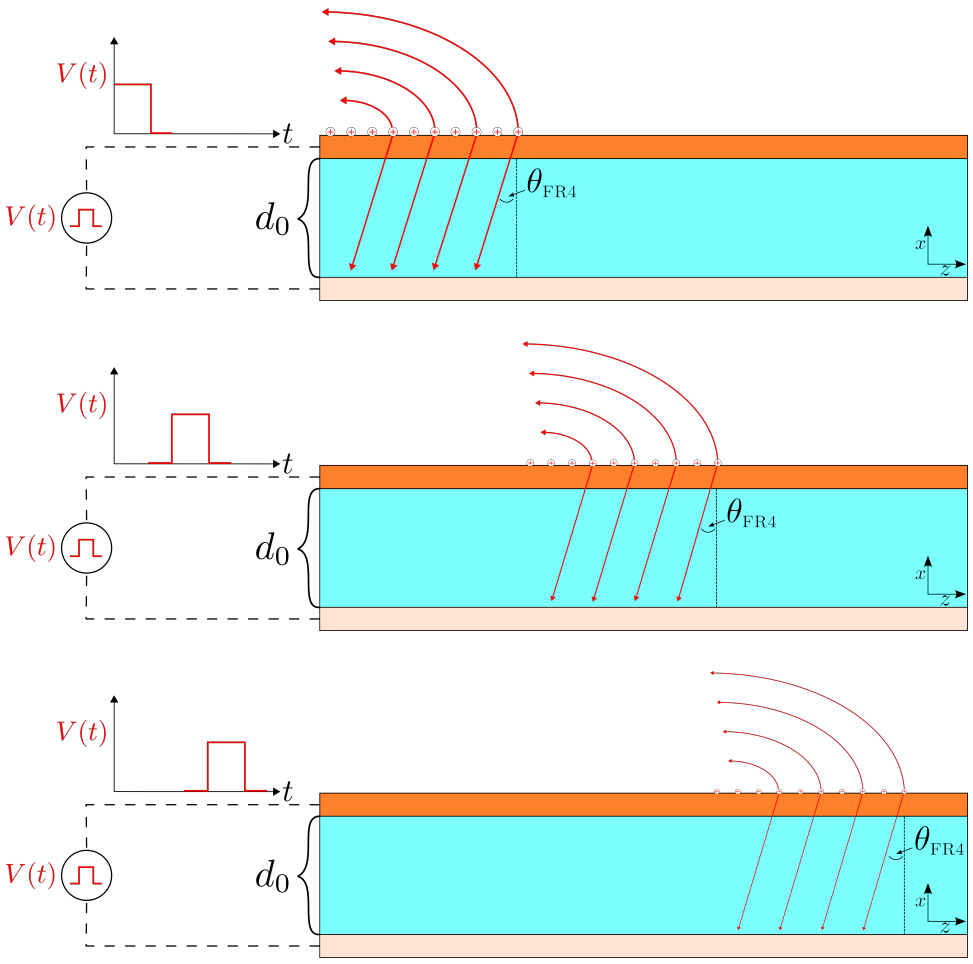

Figure 3.10: Pulse Propagation Assuming Only Surface Charge Density on the Top of the Conductor

lines are decreasing in magnitude (drawn less bold) which is speculated to be due to the radiation loss by absorbing material molecules that are involved in Cherenkov radiation. Thus, the surface charge density on the top of the signal conductor is an evanescent propagation mode since electromagnetic waves are continuously losing energy.

By superimposing the illustration of surface charge density on both top and bottom of the microstrip transmission in Figure 3.11, the "race" condition between the two surface charge densities is made clear. The reason that a precursor pulse is not detected to arrive at the end of the transmission line twice as fast as the pulse in the

region below the transmission line is due to the evanescent losses of induced material dipoles and their subsequent re-radiation i.e. Cherenkov radiation.

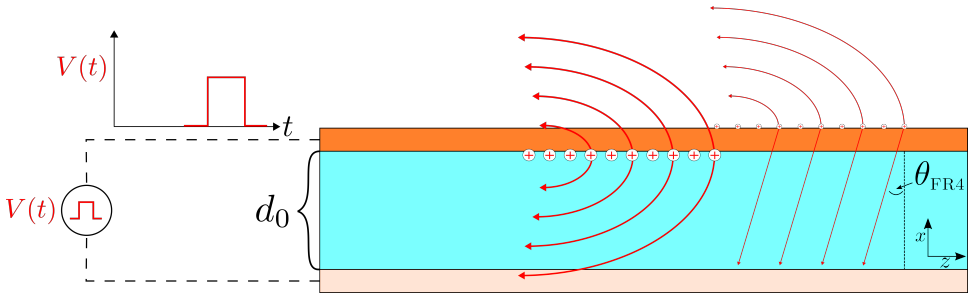

Figure 3.11: Superimposed Charge Densities on both Top and Bottom of the Signal Conductor

3.5 Speculation on Ringing Dipoles

In his book *The Foundations of Signal Integrity*, Huray computes the induced electric dipole from the sudden interaction with a uniform electric field intensity. This displacement is in the x-direction and normal to the direction of propagation. To evaluate this displacement, a convolution is performed between the step function electric field intensity, $f(t-\tau)$, and the Green's function for the stationary dipole, $G(t)$. The electric dipole is described with oscillator coefficients of spring constant $\sqrt{k_i/m}$ and damping constant b_i/m. This convolution is given in Equation 3.7 and shown pictorially in Figure 3.12.

$$x(t-t_1) = \frac{-e}{m}\vec{E}_p = \int_0^\infty f(t-\tau)e^{(-\frac{b_i}{2m}\tau)}\frac{\sin\sqrt{k_i/m-(b_i/2m)^2\tau}}{\sqrt{k_i/m-(b_i/2m)^2}}d\tau \tag{3.7}$$

As a rapid moving Electric field intensity passes by and induces electric dipoles in the medium, these dipole moments continue to oscillate and decay as shown in the envelope drawn in Figure 3.12c. Huray described these oscillations as "ringing dipoles". We speculate that the electromagnetic fields in the wake of such oscillating

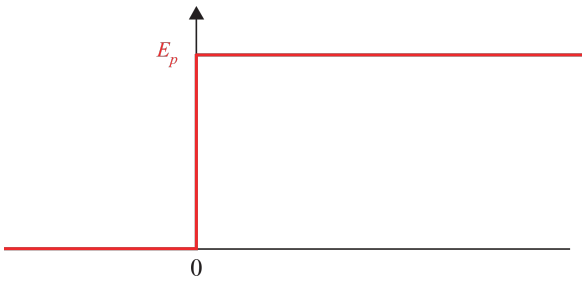

(a) Electric Field Intensity in the x-direction

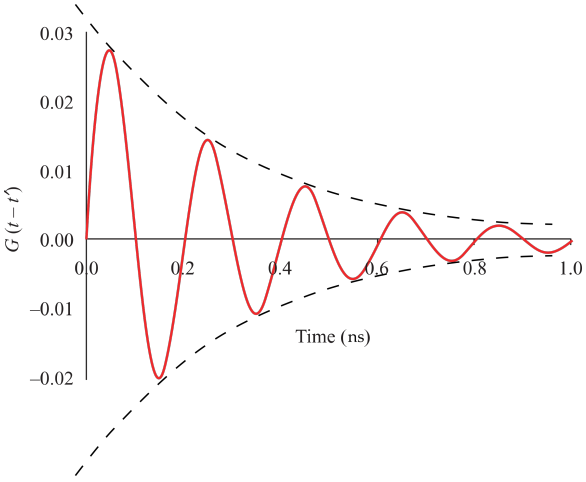

(b) Green's Function for the Charge with Spring Constant $\sqrt{k_i/m} = 5\,\text{GHz}$ and Damping Constant $b_i/m = 1\,\text{GHz}$

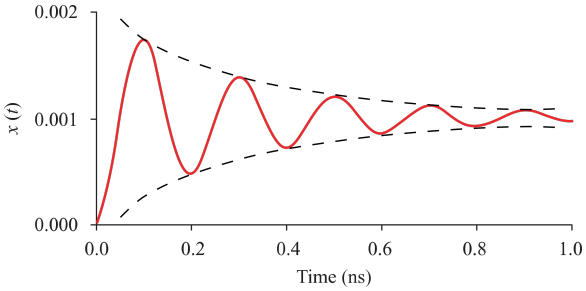

(c) Convolution Response Showing the Oscillating Decay

Figure 3.12: Pictorial of the Convolution between $G(t)$ and $f(t-\tau)$

dipoles would fluoresce and create losses in the medium. These loss mechanisms from the evanescent fields are from the same mechanisms that create Cherenkov Radiation.

Jefimenko describes the effect of a moving point charge on a stationary charge by the assistance of a dynamic field map [22]. A similar diagram is reproduced in Figure 3.13. This map shows the accumulation of electric field vectors *as measured* by the stationary charge at point O for twelve previous positions as well as the current

position of a point charge q moving at a constant velocity v_p. The previous positions are distinguished by progressively transparent circles containing a red plus sign. Note that the dynamic field map is representing charges moving less than the speed of light in the medium. Corresponding vector lengths indicate that the stationary charge

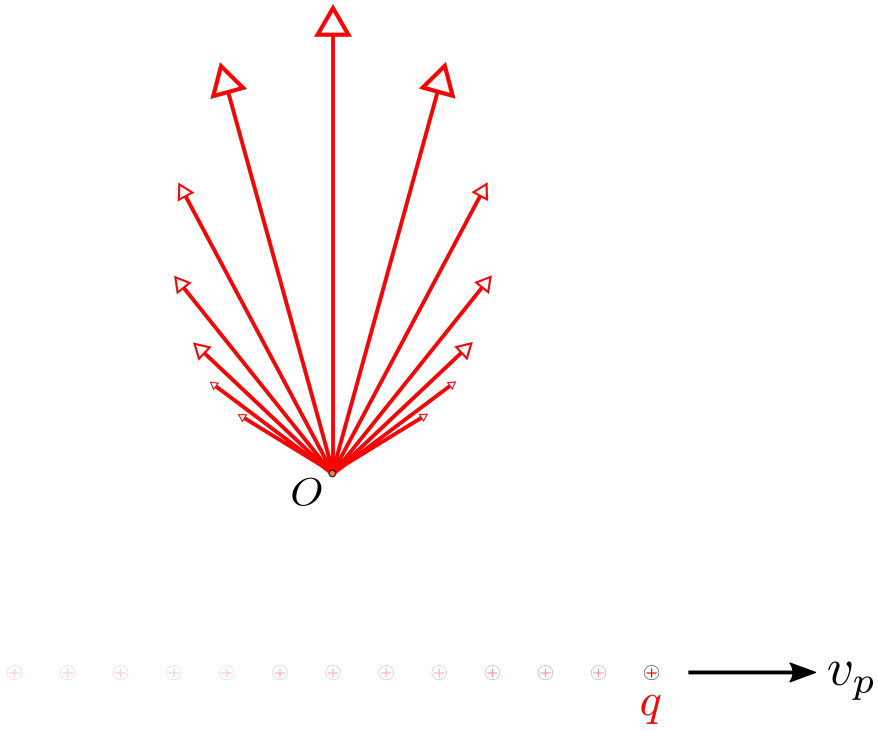

Figure 3.13: Dynamic Electric Field Map

experiences a "shock" normal to the direction of motion due to the burst of electric field from the moving point charge. It is noted that the outline traced by the vector map is the Electric field contour map. The width of the electric field contour narrows as the velocity of the charge approaches the speed of light [22]. Once the speed of light in the medium is exceeded, the electric field lines are now similar to the shock cone of Cherenkov Radiation. This description agrees with the "ringing dipole" scenario given by Huray and may be a similar loss mechanism as the shock wave of Cherenkov radiation.

Revisiting the shock wave distribution from N number of charged particles, it is shown in Figure 3.14 that the transverse displacement from a charged particle

decays or “rings” for some time after the pulse width shock wave distribution. The oscillations is determined by the drag coefficients of nearby neighboring atoms or molecules. This transverse displacement and subsequent return to a neutral state would exhibit radiation loss and by such photons of various frequencies are released (perhaps in the visible spectrum in some cases).

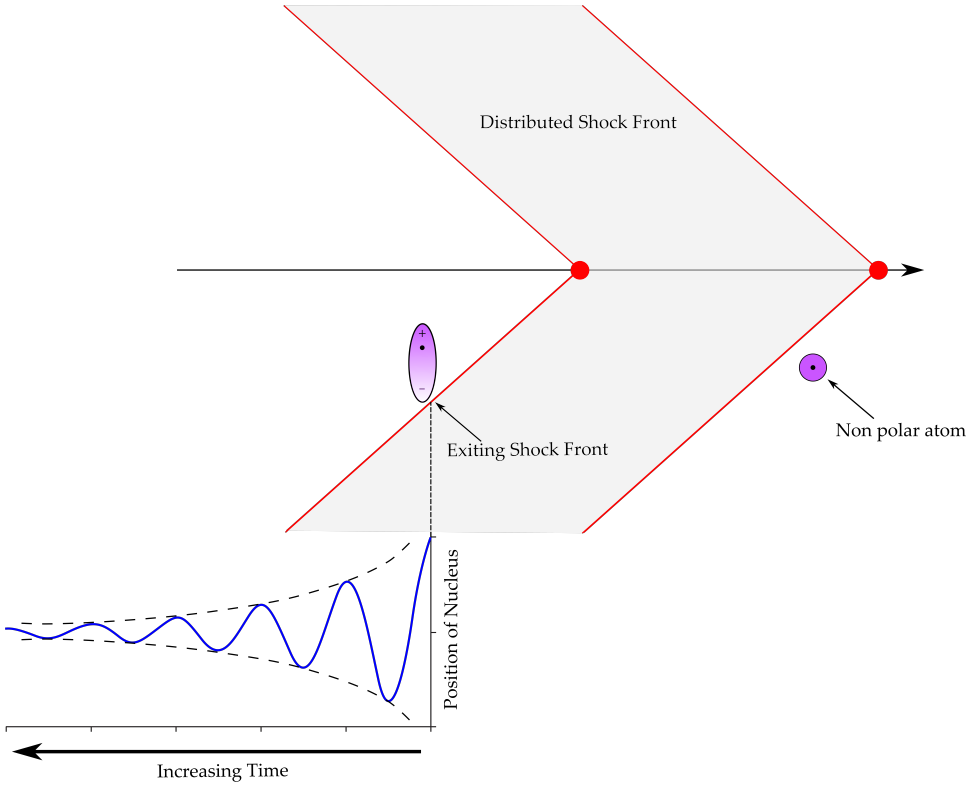

Figure 3.14: Ringing Dipole After the Distributed Shock Front

3.6 Simulation of a Pulse Propagating on a Microstrip Transmission Line

To better explore a pulse propagating along a microstrip transmission line as described in Sections 3.3 and 3.4, a series of numerical simulations are performed and analyzed in this section. The simulation software used for these simulations is ANSYS HFSS Transient Solver which is a 3D Full Wave, Time Domain Electromagnetic Field solver

based on the Discontinuous Galerkin method (DGTD). The geometry constructed for simulation is found in Figure 3.15.

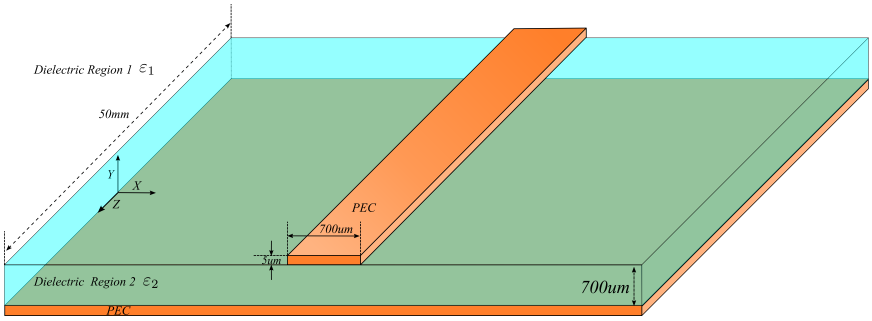

Figure 3.15: Microstrip Transmission Line Geometry for Pulse Simulation

Excitation is achieved through a lumped port and assigned a Gaussian Pulse as described mathematically in Equation 3.8. The magnitude is set as $V_o = 1\,\text{V}$ and the pulse width chosen as $w = 6\,\text{ps}$.

$$V(t) = V_o e^{\frac{-t^2}{2w^2}} \tag{3.8}$$

The dielectric regions above and below the signal conductor are assigned several different configurations. First, air is assigned to both dielectric regions 1 and 2. Second, a material with relative permittivity of 4 is assumed both above and below the signal conductor. Lastly, air is assigned above the signal conductor and a dielectric region with relative permittivity 4 is assigned below. The last configuration closely represents a microstrip transmission line.

Pulse propagation is visualized for each of these configurations by plotting the electric vector field for both the 2D cross-section cut in the middle of the signal conductor and for the entire simulated volume at an isometric view. Figure 3.16 contains an illustration of the 2D observation plane which is cut at the middle of the microstrip transmission line. This is the yz cross-section and referred to as the side view.

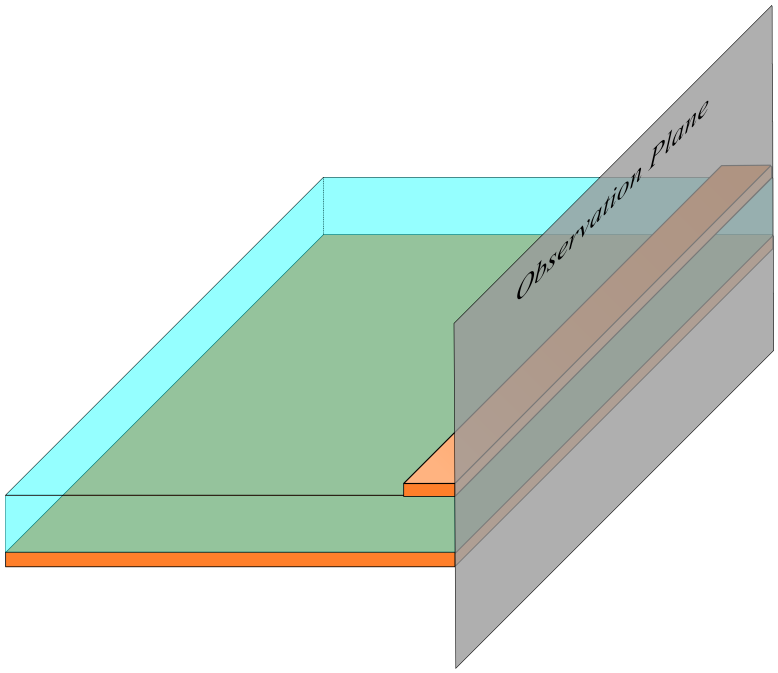

Figure 3.16: Observation Plane for Side View (Y-Z Plane) of Pulse Simulation

Figure 3.17b contains the side view of a microstrip with a dielectric medium of relative permittivity equal to 4 both above and below the signal conductor when the pulse is located near the receiving end of the transmission line. Compared to Figure 3.17a where the microstrip dielectric regions are assigned with air both above and below, the electric vector field has more curvature. This is expected because the relative velocity of the medium with relative permittivity of 4 is half the velocity of propagation in air.

Figure 3.18a, again, contains the side view of a microstrip with a dielectric medium of relative permittivity of 4 both above and below the signal conductor when the pulse is located near the receiving end of the transmission line. However, Figure 3.18b contains the Electric vector field when the dielectric regions of the microstrip are changed to air above and relative permittivity of 4 below the signal conductor. As noted from Figure 3.18b, the pulse has broadened with more distinct areas behind and in front of the main body of the pulse as compared to a microstrip where the regions above and below are homogeneous. The area behind the main body of the

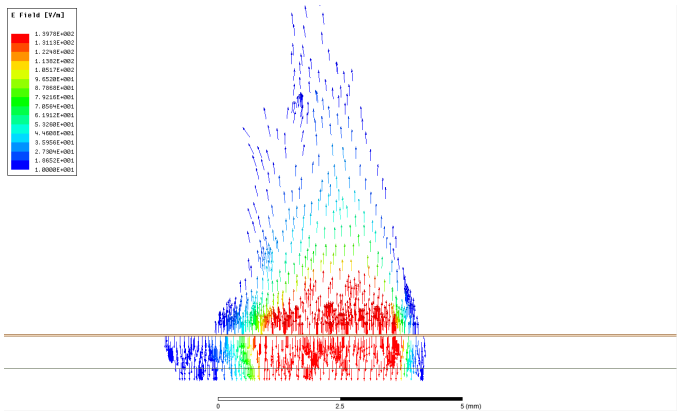

(a) Air Dielectric in Regions 1 and 2

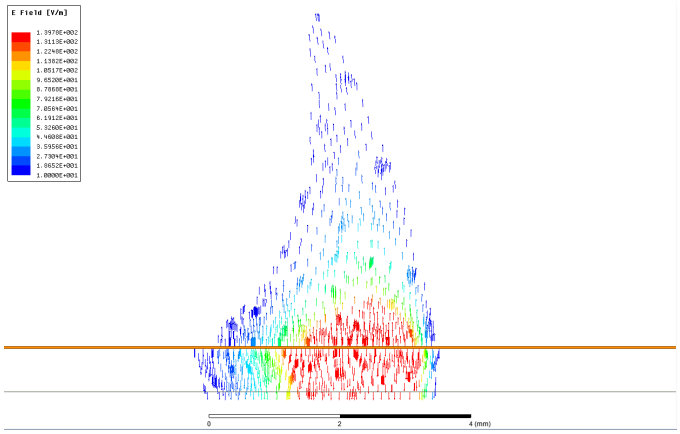

(b) Relative Permittivity of 4 in Dielectric Regions 1 and 2

Figure 3.17: Microstrip Transmission Line Electric Field Vector Plot Side View (yz cross-section)

pulse (the post-cursor region) is likely due to reflections off the reference plane. The area preceding the main body (the pre-cursor region) is speculated to be due to the mismatch of propagation velocity above and below the signal conductor. In the region above, the charges on the top of the signal attempt to "race" ahead. However, Cherenkov radiation losses as described in Section 3.5 create an evanescent propagation mode. This continuous evanescence of the charge density on the top of the signal conductor produces a pulse that appears more broad or dispersed in electric vector field intensity plots.

To further examine the pre-cursor and post-cursor regions of the pulse, Figure 3.19b contains an isometric view of the pulse on the mixed medium microstrip

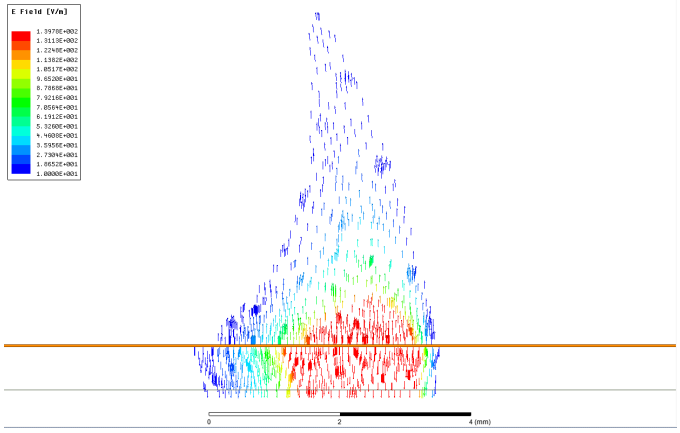

(a) Relative Permittivity of 4 in Dielectric Regions 1 and 2

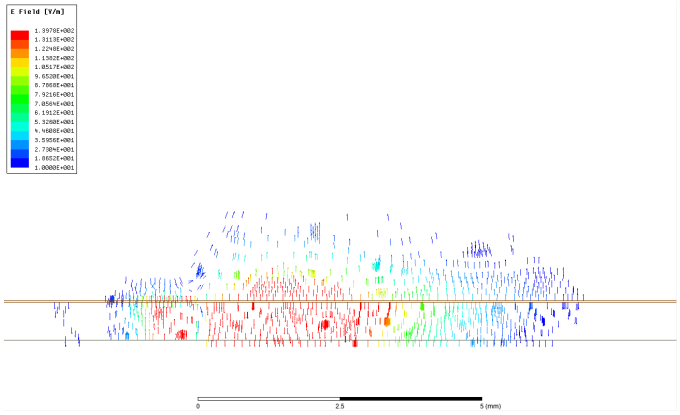

(b) Air Dielectric in Region 1 and Relative Permittivity of 4 in Dielectric Region 2

Figure 3.18: Microstrip Transmission Line Electric Field Vector Plot Side View (yz cross-section)

near the end of the transmission line. The pulse appears elongated compared to the more compact pulse of Figure 3.19a.

Figure 3.20 contains a series of frames of an animation of the pulse propagation for the mixed medium microstrip near the pulse excitation. These frames capture the transient nature of the charge density on top of the signal conductor. During the excitation, the pulse has not broadened to the same extent as shown in Figure 3.19b near the end of the transmission line. Thus, evanescent charge on the top of the conductor is more apparent than later in the pulse propagation and is of a short, transient duration. Figure 3.20a shows the electric vector fields at 42 ps after the

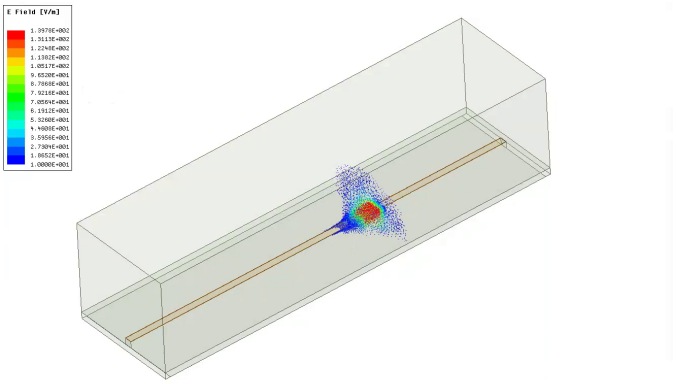

(a) Relative Permittivity of 4 in Dielectric Regions 1 and 2

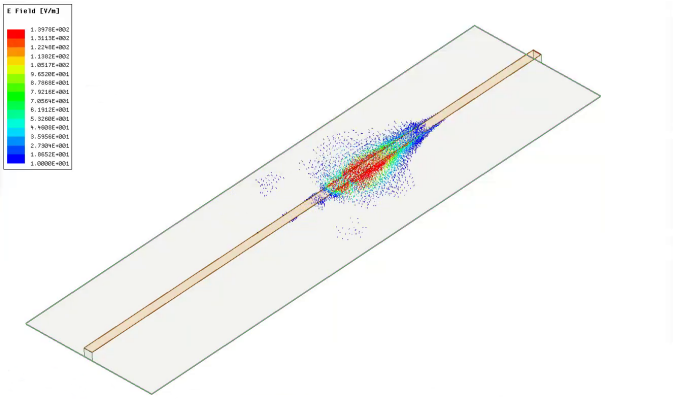

(b) Air Dielectric in Region 1 and Relative Permittivity of 4 in Dielectric Region 2

Figure 3.19: Isometric View of Pulse Propagation on a Microstrip Transmission Line

excitation. In this frame, the leading charges are beginning to break away from the main pulse. In the following frame which is 15 ps later in time, the charge density has separated from the main pulse as shown in Figure 3.20b. In the final frame which is 69 ps after the excitation, the transient charge density has evanesced and is barely visible.

3.7 Chapter Discussion and Conclusion

Chapter 3 explores applications of time retarded electromagnetic fields as they propagate in a microstrip transmission line. Surface charge density propagating on the top of the signal conductor where the air dielectric allows propagation near the speed of

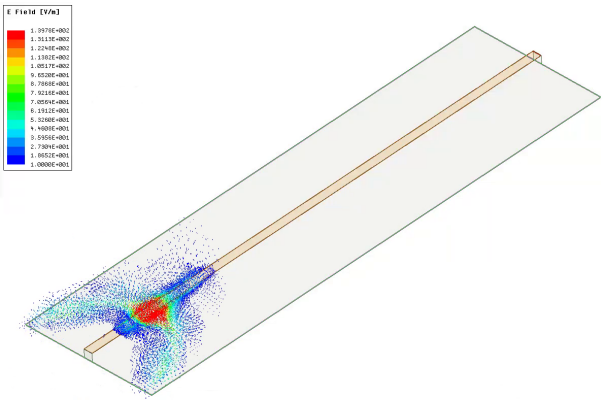

(a) Pulse 42 ps After Excitation

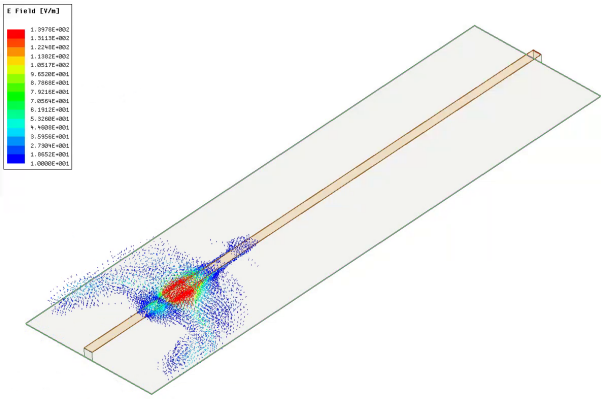

(b) Pulse 57 ps After Excitation

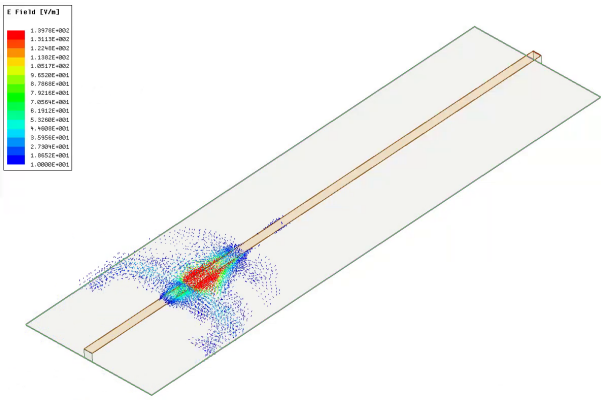

(c) Pulse 69 ps After Excitation

Figure 3.20: Initial Excitation Showing Evanescent Pulse Propagation

light is contrasted with charge density on the bottom of the signal conductor where the medium supports a propagation velocity roughly one-half the speed of light. A new loss mechanism in microstrip transmission lines is speculated to exist namely Cherenkov radiation. Time domain, numerical simulation visitations are presented. These simulations appear to indicate both the dispersion because of the medium mismatch as well as the evanescent propagation mode for the charges on the top of the signal conductor limited by Cherenkov radiation or Ringing Dipoles. We thus conclude that: "Every microstrip transmission line should cause a fast precursor pulse of short, transient length that shows up as lost fluorescent energy in the medium at frequencies characterized by its atoms or molecules, principally at locations near the insertion location in the medium."

Chapter 4

Comparison Of Numerical And Analytical Methods

In his dissertation, Dr. Ye uses a simulation constructed in MathWorks MATLAB to analytically evaluate the retarded electromagnetic field solutions (Jefimenko's Equations) for several simple geometries. However, rather than construct and support a new simulation engine for the RLGC(p) model, it is advantageous to use commercially available numerical method simulators (particularly for the geometry flexibility allowed therein) to extract the field data and package it into the RLGC(p) model. For this reason and because previous RLGC(p) modeling is benchmarked against several commercially available numerical method simulators [24], this chapter provides comparison between one of the transmission line (a microstrip waveguide) structures that is previously solved [1],[24] by the analytic code implemented in MathWorks MATLAB (hereafter referred to as Analytically Solved Jefimenko's Equation or ASJE) and a similar structure evaluated with ANSYS HFSS.

To review, the geometry under consideration with ASJE is a uniform, lossless, and infinitesimal line source along the z direction which represents an idealized transmission line or embedded microstrip wave guide. This line source is a distance h above a flat, infinite, and PEC plane which acts as the reference plane. The homogeneous medium surrounding the line source is given the lossless constitutive parameters $\varepsilon = 4\varepsilon_0$ and $\mu = \mu_0$ where the fields propagate at a finite velocity v. For this simulation, the total fields are assumed to be a superposition of fields directly from the line

source combined with fields reflected in total from the reference plane via the image theory technique.

Not only is this configuration useful for cross-sectional visualizations of the electromagnetic fields, it is also the geometry for which the RLGC(p) model is compared to the Classical RLGC model, as discussed in Section 2.1. An illustration of this idealized embedded microstrip waveguide is found in Figure 4.1. Here the height h above the reference plane is chosen to be 100 mils because this is significant enough to invalidate the Classical RLGC Model. Such a height is generally assumed to be one tenth of a wave length [16][12]. By exciting this line source with a sinusoidal varying charge

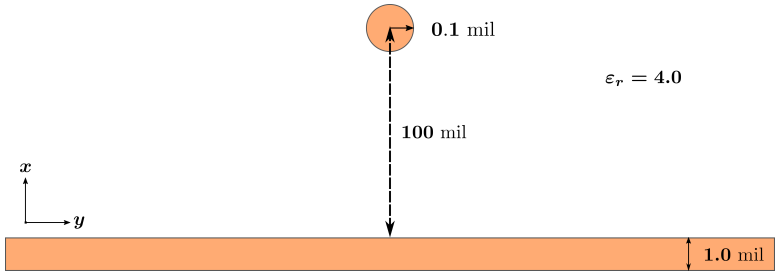

Figure 4.1: Illustration of an Idealized Transmission Line

distribution of two separate frequencies, 10 GHz and 100 GHz, the time retardation effects are evident in field plots on a cross-sectional observation plane illustrated in Figure 4.2. In Figure 4.3a and 4.3b, the magnitude of the Electric field is represented

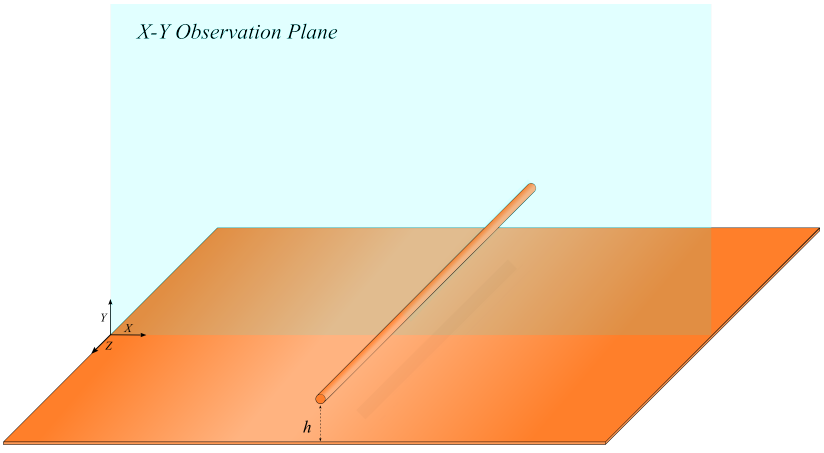

Figure 4.2: Observation Plane for Cross-Sectional Field Plots

with a red color for peak values and a blue color for minimum values. The red quiver plot arrows indicate the direction of the $\vec{E}$ field (Electrical field intensity on the X-Y observation plane) and the blue quiver plot arrows indicate the direction of the $\vec{H}$ field (Magnetic field intensity on the X-Y observation plane). The direction of quiver arrows obeys the Right Hand Rule as applied to the source current that generated them for both frequencies. This indicates that the energy is propagating in the same direction for any point on the observation plane.

In contrast to the 10 GHz excitation and consequent slow moving, uniform field patterns - shown in Figure 4.3a - are the irregular field patterns for the 100 GHz excitation - shown in Figure 4.3b. These irregular field patterns are due to the time retarded behavior of the fields and the subsequent dominance of either the field contributions from the line source, or its reflection from the reference plane. A chief characteristic of these irregular patterns are the particular nulls and peaks of the field intensity extending out as wave-like ripples. It is further noted that the quiver arrows change direction as the fields propagate out from the source indicating a change in the polarity of the field magnitude [24]. Finally, it is noted that given enough distance for the observation, the 10 GHz excitation would also exhibit similar irregular field patterns as in the 100 GHz excitation.

4.1 Analytical Methods Versus Numerical Methods

In practice, numerical methods that solve Maxwell‘s Equations are used to evaluate the signal integrity performance of transmission lines. These solutions can comprehend, from first principles, electromagnetic effects of surface waves, radiation, and parasitic coupling in printed circuit board designs [12]. Numerical methods solve Maxwell‘s Equations at discrete locations (or mesh nodes); therefore, it is reasonable to expect the time retardation behavior of the electromagnetic fields are included such solutions. However, this depends on computational resources, solver simplifying

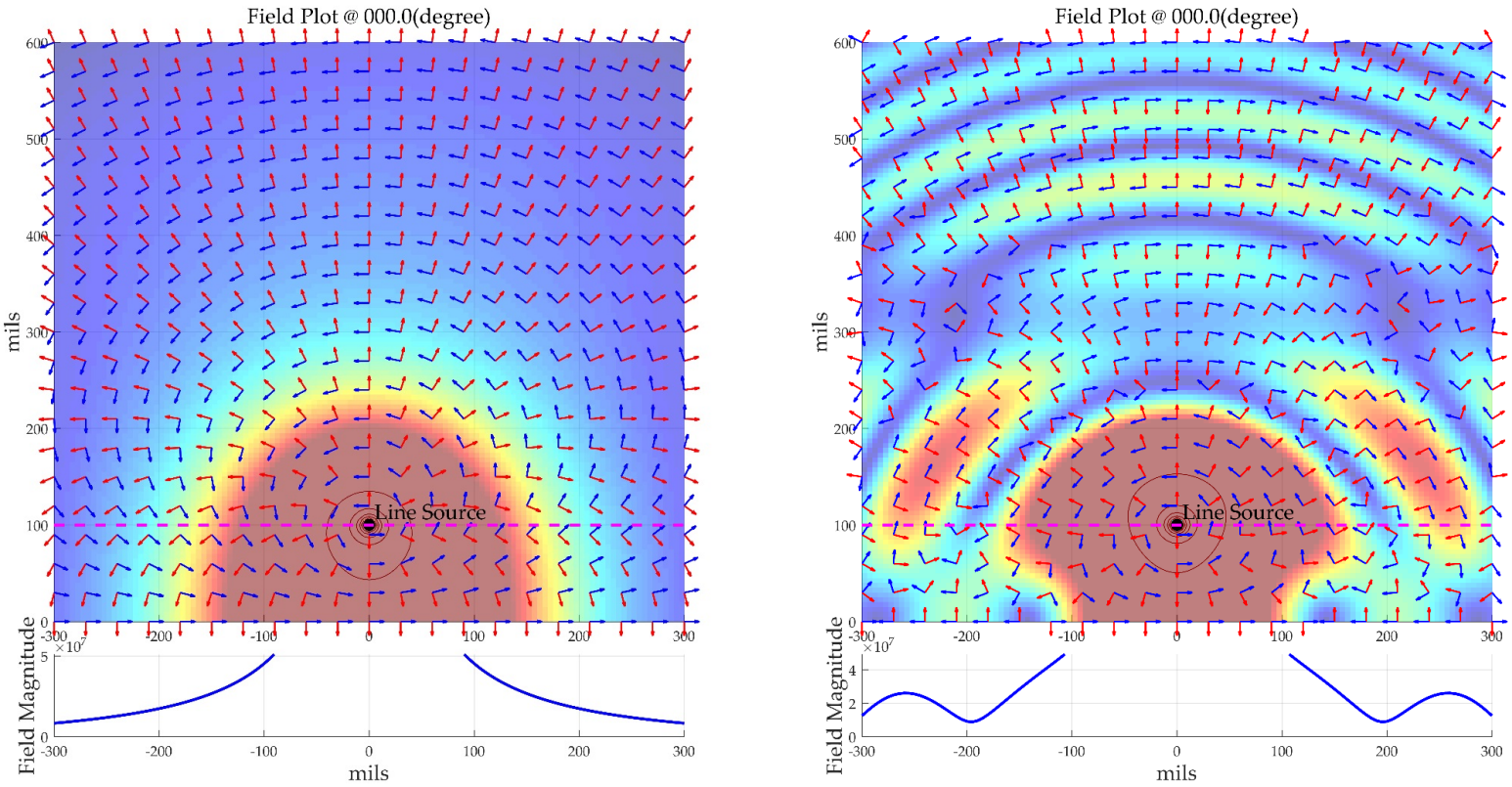

(a) 10GHz Excitation

(b) 100GHz Excitation

Figure 4.3: Magnitude of the Electric Field and Vector Quiver Arrows Observed on a Cross-section of the Transmission Line for 10 GHz Excitation and 100 GHz Excitation

assumptions (if any), and limitations of the numerical method.

Analytical methods are closed-form solutions of analytical functions. These methods make use of simplifying assumptions (including thin wire, image theory technique, homogenous and lossless mediums, static fields, etc.) and exist for only the simplest of geometries. Despite this, these methods can be invaluable while simplifying and iteratively applying assumptions to gain insight into the fundamentals of a particular phenomenon. Also, they can be an error-free reference for validating numerical methods [12]. Even so, complexities of electronic design within a printed circuit board favor numerical methods.

Numerical methods seek to find approximate solutions to Maxwell‘s Equations by discretizing the continuous integral equations or differential equations resulting from given boundary and initial conditions. There exist many approaches ranging from problem specific to very general. Likewise, CAD based numerical solvers for Maxwell‘s Equations are plentiful, but one must be cognizant and familiar with the underlying assumptions made within these coding engines. Computational resources required for numerical methods are proportional to the electrical size of the geometry because these simulation codes discretize the physical geometry typically with 20 to 30 mesh cells per wavelength. The resulting matrix computations are often limited by either solution time or system memory depending on if the numerical method is time domain based (transient method) or frequency domain based (time harmonic method), respectively. Available numerical simulation tools comprise several dimensionality categories (2D, 2.5D, and Full Wave) with varying applications and assumptions during calculation [12]. Some commercial tools can also make use of multiple solvers to provide electrical evaluations of multi-layer interconnect [43]. This too must be taken into account when understanding the limitations of design results.

It is not sufficient to say that all numerical codes contain the time retardation

behavior of electromagnetic fields, but full wave solutions are the most likely to do so. For this reason, the following sections will use as a comparison benchmark the Finite Element Method, Full Wave simulation tool: ANSYS HFSS.

4.2 Comparison for a Line Source Over a PEC Plane

At the beginning of this chapter, an idealized transmission line similar to an embedded microstrip waveguide is described and illustrated in Figure 4.1, page 54. This geometry is solved with the ASJE code. A similar geometry is drawn and simulated in ANSYS HFSS. Table 4.1 contains known geometric and material differences between these two simulations. Differences listed in Table 4.1 are either to satisfy the simulator requirements (finite radius of the line source), or to fit within the limitations of the available compute resources (line source length and boundary size).

Table 4.1: Geometric and Material Differences Between ASJE and HFSS

Description	**ASJE**	**HFSS**
Radius of Line Source (mil)	Infinitesimal	0.1
Metal Conductivity (S/m)	PEC	$6e^{10}$
Length of Line Source (mil)	1000	250
Boundary (X mil,Y mil)	None	(600 x 500)

The method of comparison is to observe the Electric field intensity magnitude resulting from a 100 GHz excitation on the 2D cross-section illustrated in Figure 4.2, page 54 and to overlay plots of the Electric field intensity magnitude at the height of the line source, $h = 100$ mil. For initial field cross section comparison shown in Figure 4.4, it is apparent that several additional considerations must be aligned between the two simulators (chiefly the phase and magnitude of the excitation as well as the assignment of the color scheme). The magnitude and phase are adjusted in HFSS by changing the `Menubar -> HFSS -> Fields -> Edit Sources` dialog box to specify

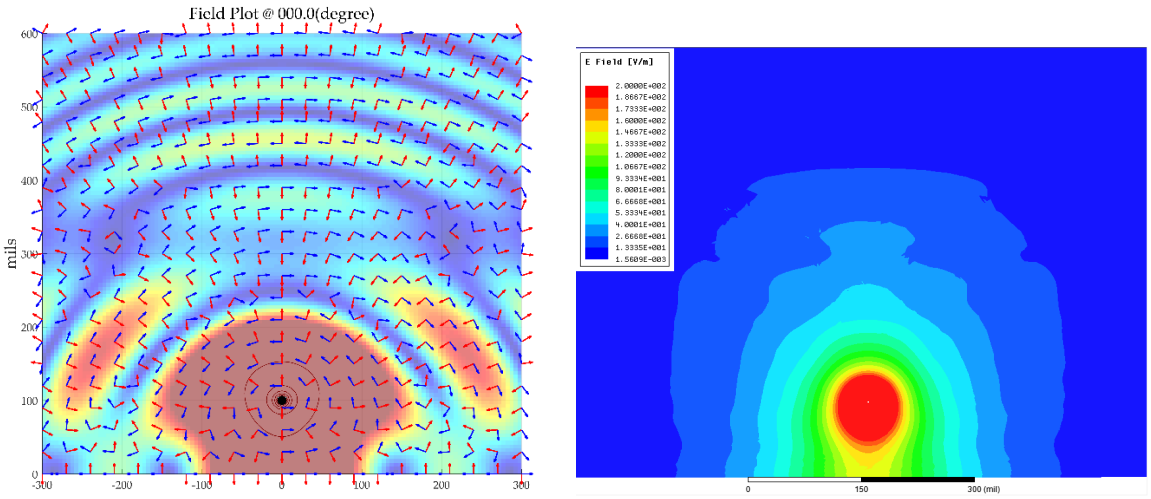

(a) ASJE (b) ANSYS HFSS

Figure 4.4: Initial Comparison between ASJE and ANSYS HFSS

desired magnitude (mW) and phase (degrees). It is notable that the input phase is constrained to a 5 degrees step size thus limiting the resolution of phase matching to the peak magnitude. The excitation port in HFSS is located at the beginning of the line source; however, the observation is at the center of the line source. The method to translate from the excitation phase that produces a peak electric field magnitude at the port excitation to that at the center of the line source is as follows. The magnitude is plotted along the length of source at a distance of 1 mil from the conductor and the phase is swept to obtain the peak value. Figure 4.5 contains a plot of the electric field magnitude. Note the emphasis on the phase of 45 degrees which produces a peak electric field magnitude at the center of the line source, $l = 125$ mil. The source charge density, $\rho\left(z',t\right) = \alpha_s\left(z'\right) Q \cos\left(k_s z' - \omega t - \varphi\right)$, is the sinusoidal excitation in ASJE [1]. The attenuation α is made unity, and the charge Q in Coulombs (C) is iteratively adjusted to align with the HFSS source input power. Attempts to calculate the translation of input power to values of Q are unsuccessful and presumed to be due to the finite radius of the line source in HFSS. Thus an empirical approach is necessary. Resulting values between the two simulators are:

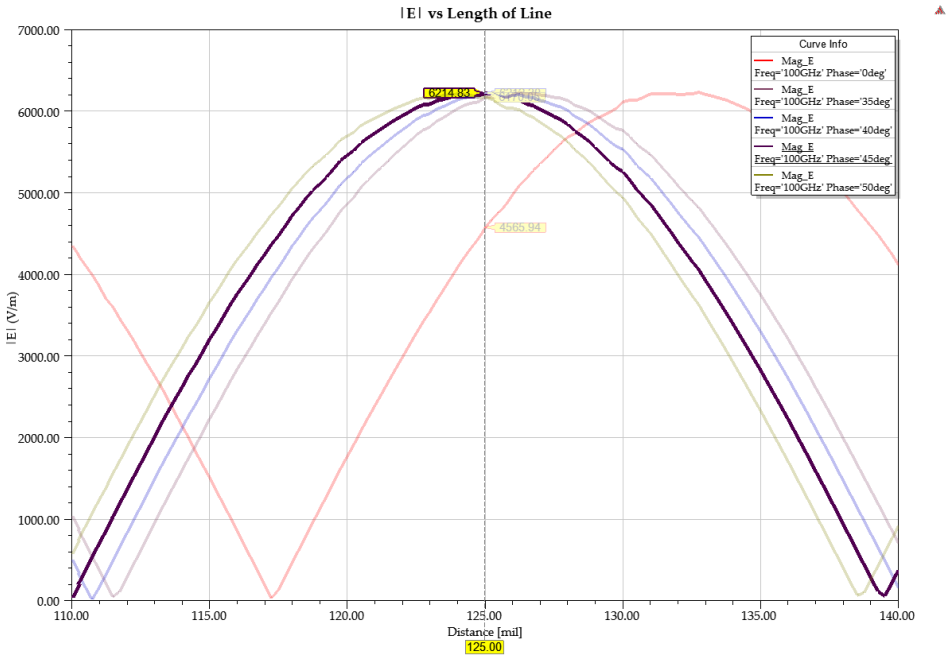

Figure 4.5: Electric Field Magnitude Along the Line Source

input source power in HFSS = 0.0325 mW and $Q = 1.25e^{-6}$ C in ASJE. These values create equal magnitude at the center of the line source, $l = 125$ mil, and a distance of 1 mil horizontally from the line source.

To align color scales, it is beneficial to plot the field data using the same plotting engine. This is achieved by scripting an extraction of the field solution from HFSS via the `Fields Calculator` and piping it through the plotting engine of ASJE. Thus the color scheme, range of colors, and magnitude calculations are the same. A caveat concerning this extraction is that ASJE calculates the field data at 1 mil increments in the x-direction away from the line source, whereas, HFSS is interpolating the field data between mesh nodes.

Comparisons of cross-section field data are displayed in Figure 4.6a and 4.6b. Examining the features of Figures 4.6a and 4.6b, it is apparent that the peaks and nulls that indicate time retardation are more pronounced in the ASJE simulation, Figure 4.6b.

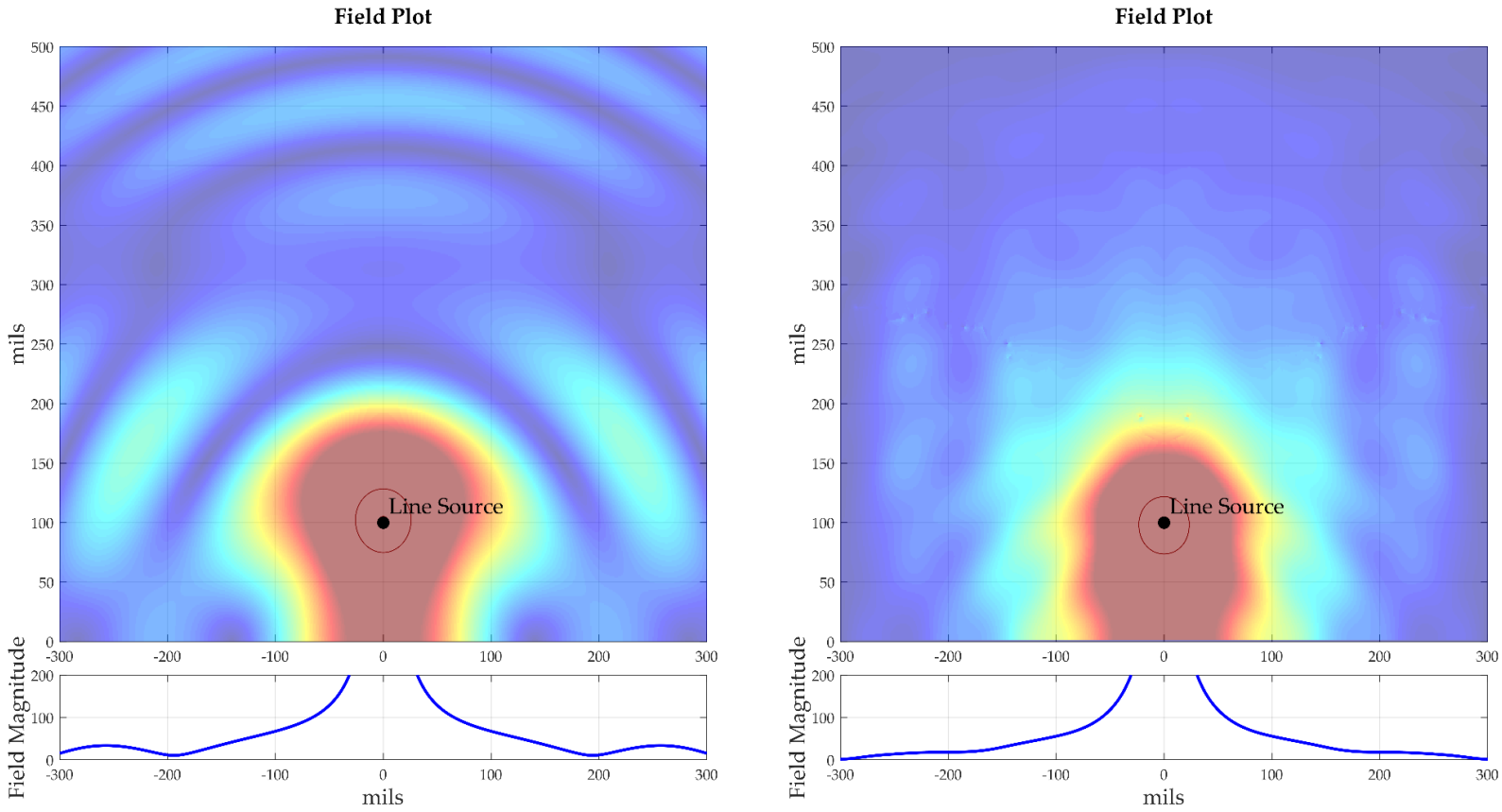

(a) ASJE

(b) HFSS

Figure 4.6: Cross-sectional Observation Comparison between ASJE and HFSS

The magnitude moving away from the line source, in the X-direction, and at the height of the line source is plotted in Figure 4.7a and Figure 4.7b, page 63. For the first 50 mil, the magnitudes are in agreement. However, interesting behaviors occur for the small field values between 50 mil and 300 mil away from the line source. For these distances, the ASJE produces a more defined peak and null.

Concerns about mesh density and handling of the reference plane - large finite conductivity versus PEC boundary - are not able to be addressed with the embedded microstrip structure. The limitations on compute resources (2 Terabyte of RAM) did not allow the max mesh length to decrease below 15 mil for the defined boundary box. Reducing the boundary box raises concern about non-ideal radiation boundary reflections which may interfere with small values of electric field. To address these issues, the following section explores a further simplified geometry of a line source without a reference plane.

4.3 Comparison for a Line Source Geometry

If the reference plane is absent from the previously described transmission line geometry, the line source is expected to exhibit field magnitude peaks and nulls forming concentric rings of electromagnetic fields propagating radially outward [1]. Such a geometry is the subject of this section and illustrated in Figure 4.8, page 64.

This section contains simulation experiments which explore the influence of boundary size, boundary shape, and mesh density in ANSYS HFSS. All plotting is native HFSS and uses the same color scheme which is found in Figure 4.9, page 64 .

The initial simulation experiments retain the rectangular radiation boundary, but change mesh density by first allowing HFSS to converge without explicit mesh restrictions and then forces mesh restrictions of 20 mil max mesh length inside the volume. Figures 4.10a and 4.10b, page 65, contain the resulting cross section observation planes plotted natively in ANSYS HFSS.

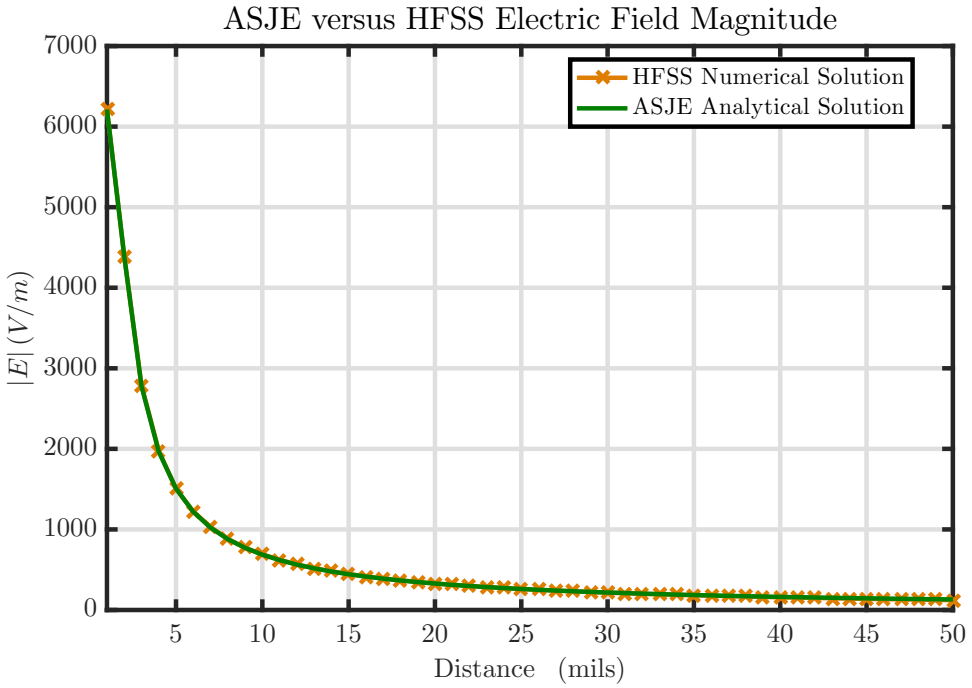

(a) 1 mil to 50 mil

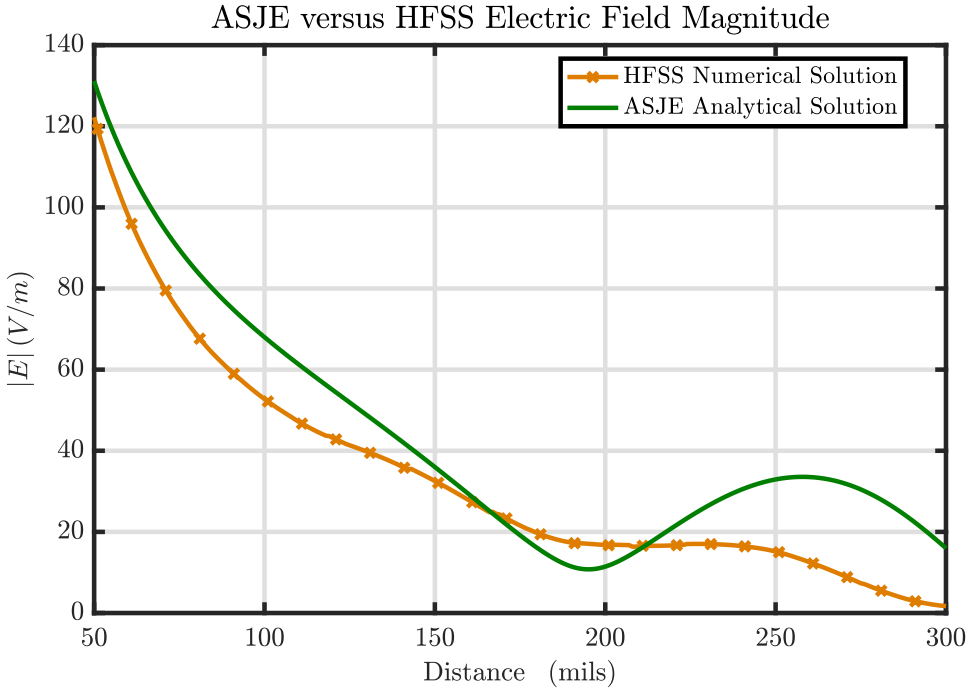

(b) 50 mil to 300 mil

Figure 4.7: Comparison of Electric Field Magnitude Along the X-Direction at the Height of the Line Source

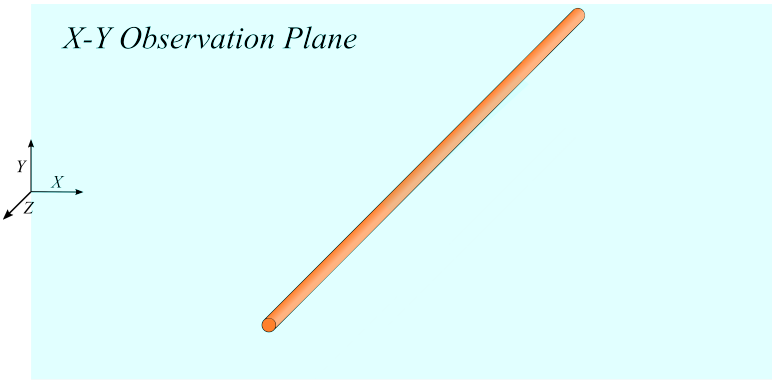

Figure 4.8: Illustration of a Cylindrical Line Source without a Reference Plane

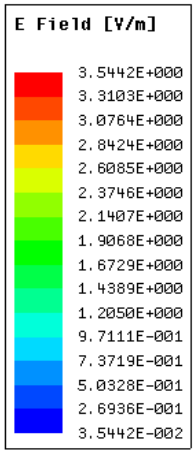

Figure 4.9: Color Scale for Electric Field Intensity

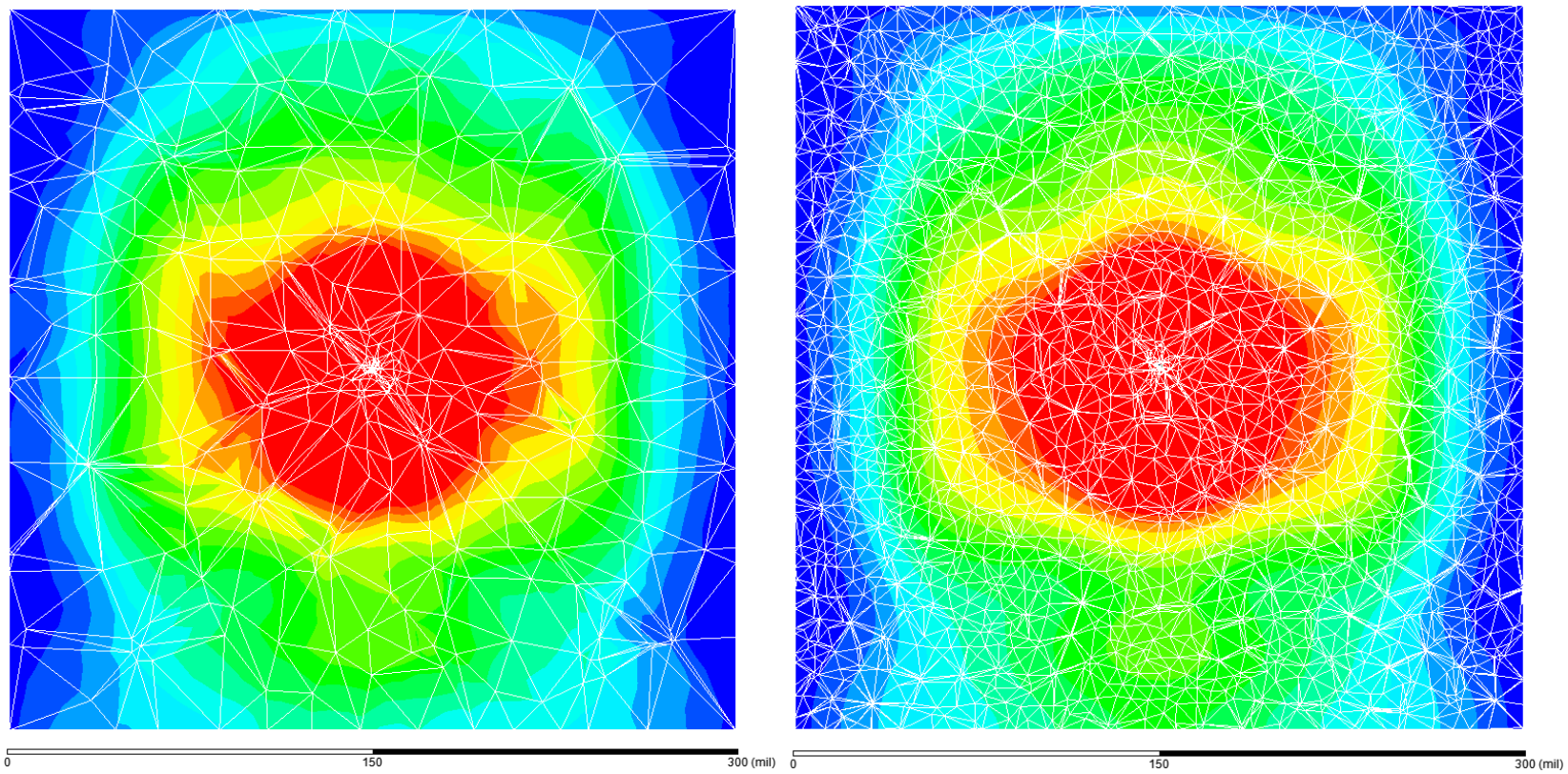

(a) Without Mesh Restrictions

(b) Max Mesh Length of 20 mil

Figure 4.10: Line Source Electric Field Intensity: Medium Permittivity = 4 and Rectangular Boundary both Without Mesh Restrictions and Max Mesh Length of 20 mil

From these figures, the dependence on mesh density to refine the contours is evident. Also, the shape of the contours is rectangular rather than circular which denotes the influence of the shape of the boundary.

The second set of simulation experiments makes a change to the medium permittivity by increasing it from 4 to 32. This increase slows down the field velocity by a factor of $\sqrt{32}$ in the medium and increases the electrical size of the problem without a physical size increase. Figure 4.11a and Figure 4.11b contain the resulting 2D observation planes plotted natively in ANSYS HFSS. From this set of simulations, the concentric field magnitude peaks and nulls are brought out, but so too is the influence of the radiation boundary shape on the field plots.

The third set of simulations experiments repeat the previous for a relative permittivity of 32; however, the radiation boundary is made cylindrical instead of rectangular. This change allows the fields to have normal incidence on the radiation boundary thereby reducing the reflection [44]. Figure 4.12a and Figure 4.12b contain the line source Electric field intensity for a medium with permittivity of 32 showing both unrestricted mesh length and max mesh of 10 mil. In both of these figures, the expected concentric circular rings of field intensity peak and nulls are present. The mesh density increase refines the contours of these field regions as seen in Figure 4.13b compared with Figure 4.13a.

Figure 4.14b is an extraction of the HFSS field solution of Figure 4.13b, but plotted with the ASJE plotting engine. This is compared with Figure 4.14a which is the ASJE simulation of a similar line source geometry. Comparing Figure 4.14b to Figure 4.14a, it is noted that the nulls differ in location by approximately 30 mil and the magnitude after the null is doubled in Figure 4.14b. After observing the magnitude change versus phase, it is determined that the HFSS simulation contains a standing wave because the null position does not propagate outward as expected. This is attributed to the size of the waveport excitation and the presence of higher

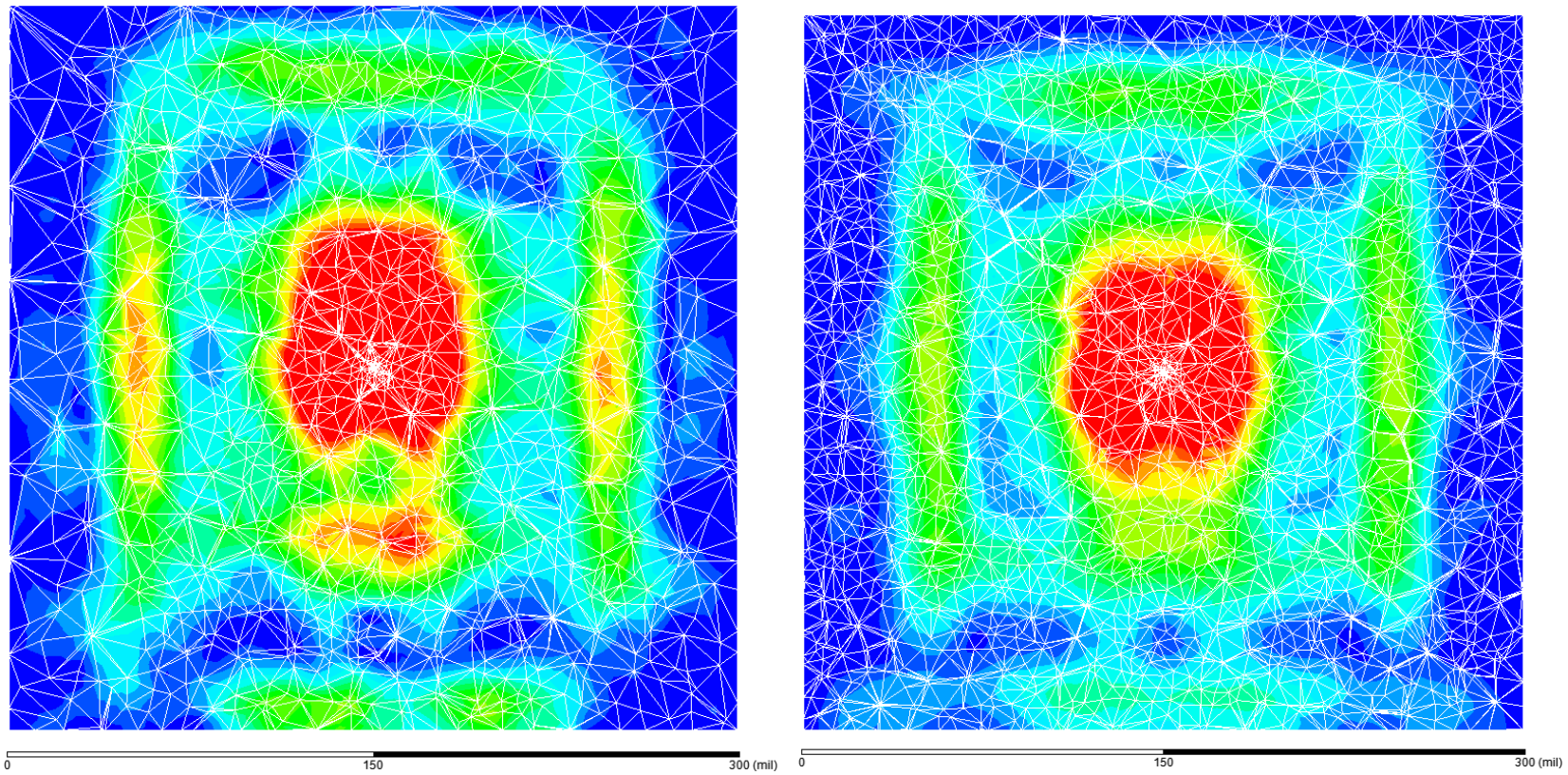

(a) No Mesh Restrictions

(b) Max Mesh Length of 20 mil

Figure 4.11: Line Source Electric Field Intensity: Medium Permittivity = 32 and Rectangular Boundary both without Mesh Restrictions and a Max Mesh Length of 20 mil

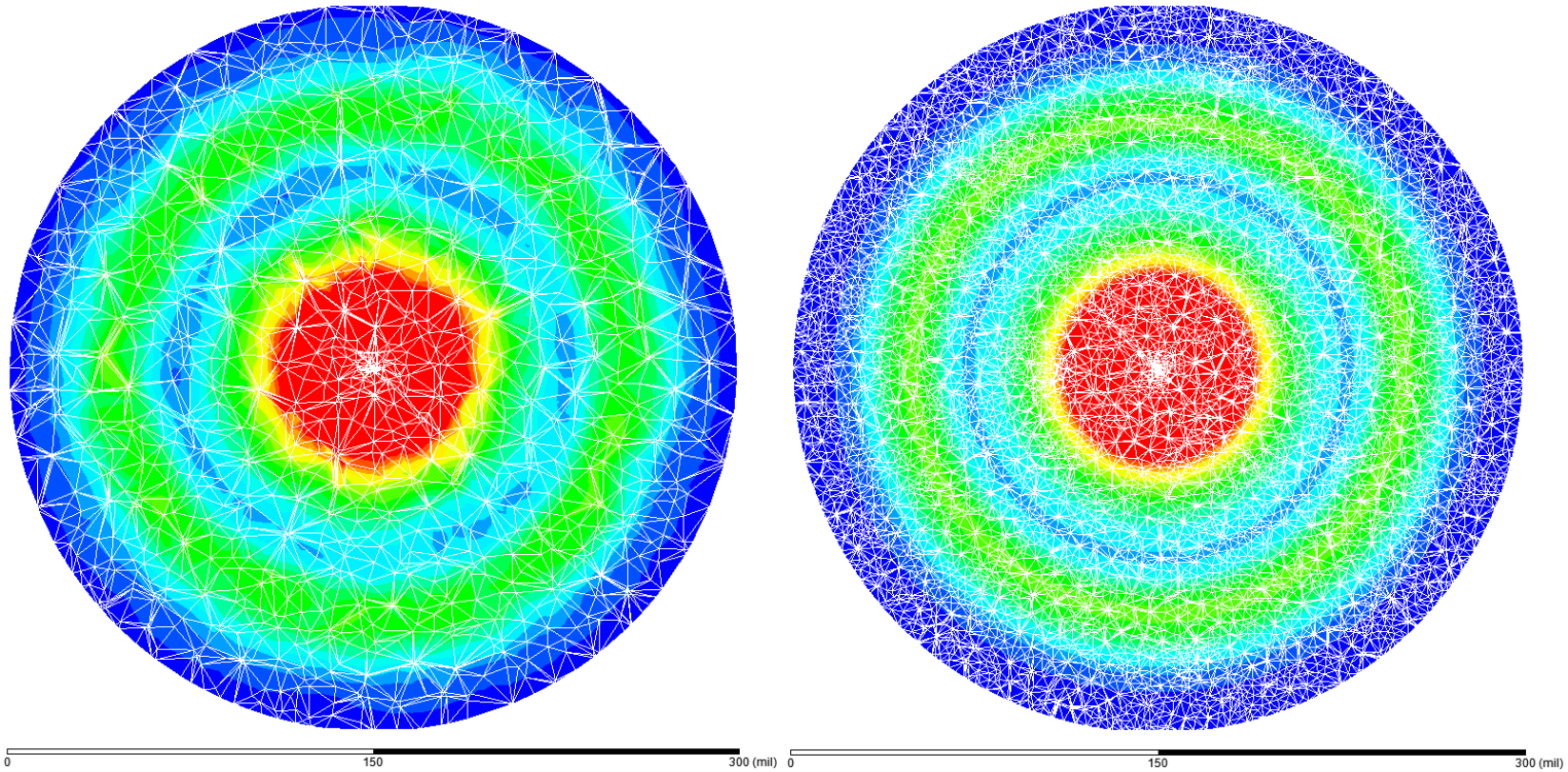

(a) Without Mesh Restrictions

(b) Max Mesh Length of 10 mil

Figure 4.12: Line Source Electric Field Intensity: Medium Permittivity = 32 and Cylindrical Boundary with an Unrestricted Mesh Length and a Max Mesh Length of 10 mil

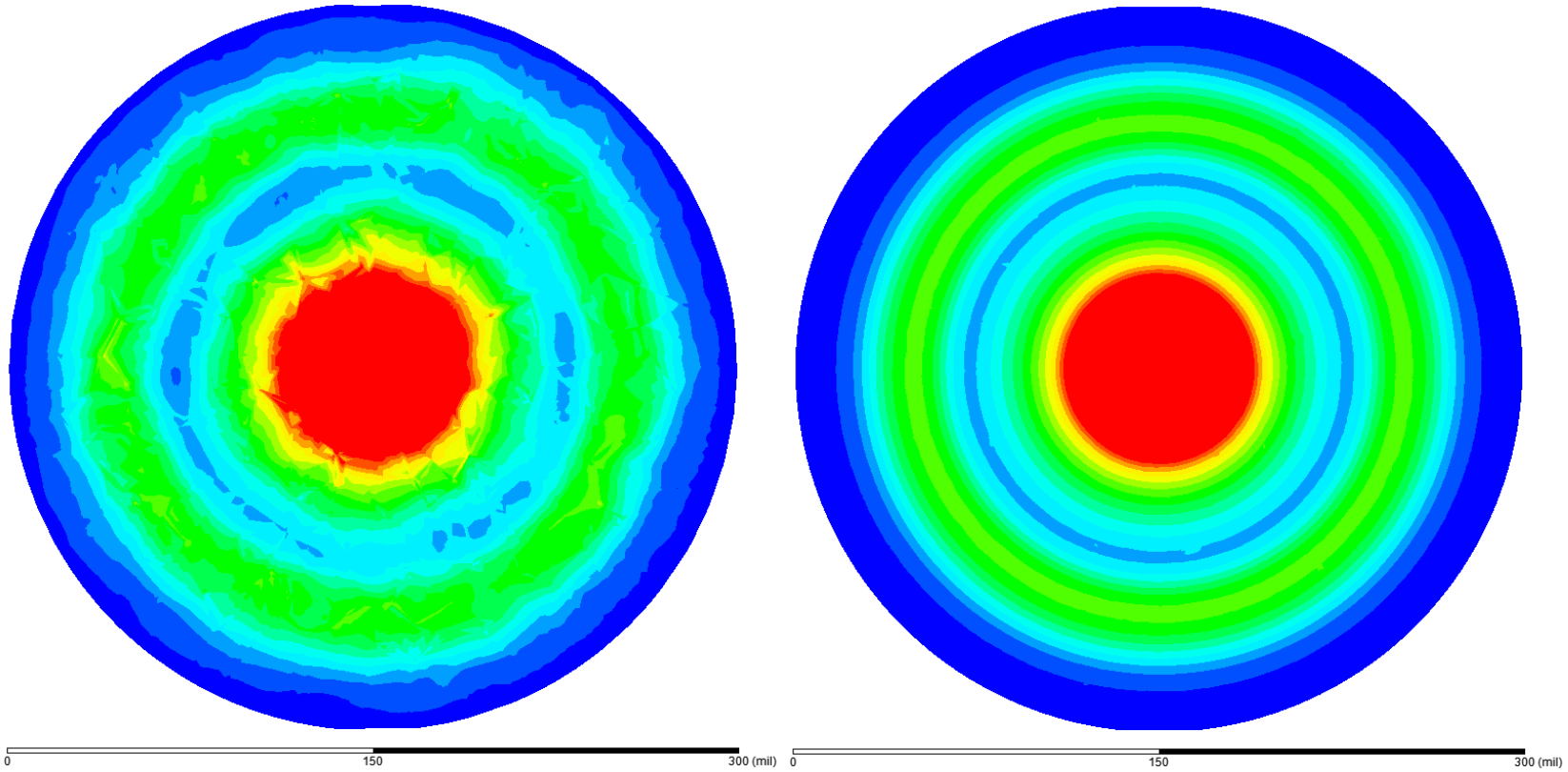

(a) Without Mesh Restrictions

(b) Max Mesh Length of 10 mil

Figure 4.13: Line Source Electric Field Intensity in Medium Permittivity = 32 and Cylindrical Boundary Mesh Plot Removed

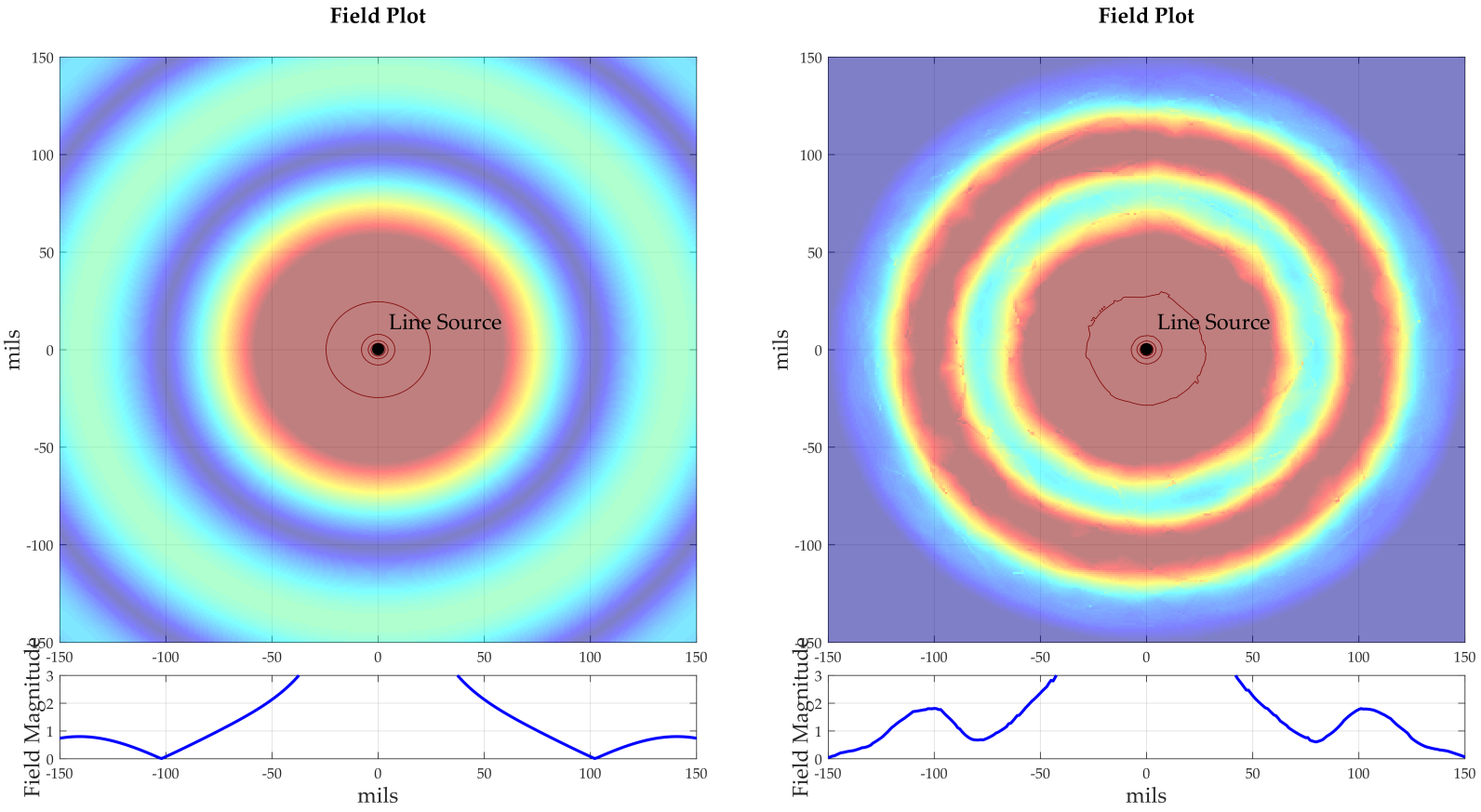

(a) ASJE

(b) ANSYS HFSS

Figure 4.14: Line Source Electric Field Intensity: Medium Permittivity = 32 and Cylindrical Boundary in ASJE and HFSS

order modes being excited in the simulation.

The wave port excitation in HFSS is a semi-infinite long waveguide of the cross section geometry matching where the port is attached to the problem [45]. For a line source excitation, the wave port is treated as a coaxial waveguide. To limit additional propagating modes, the radius of the wave port b is reduced to 6 mil. This dimension is determined from Equation 4.1 assuming the desired cutoff frequency $f_c = 100\,\text{GHz}$ [10].

$$f_c = \frac{ck_c}{2\pi\sqrt{\varepsilon}} \tag{4.1}$$

where k_c is the cutoff wavenumber and evaluated for inner radius a and outer radius b using Equation 4.2.

$$k_c = \frac{2}{a+b} \tag{4.2}$$

Reducing the wave port size eliminates the additional propagating modes and the standing wave behavior. The resulting simulation exhibits the expected behavior of the nulls in the electric field intensity propagating outward as the phase changes. However, the reduction in wave port size introduces an additional consideration. A radiation pattern is created from the source mismatch to the line source geometry. This is seen by observing the magnitude of the Electric field intensity on the cross-section of the X-Z plane. This top down view along the z direction is shown in Figure 4.15a.

When plotting the X-Y cross-section for this configuration, the number of nulls has increased as shown in Figure 4.15b. Typically, a longer length of line is simulated and the observation plane moved to a position where this radiation pattern has subsided. For this particular simulation there is a conflict between the available compute resources and the desire to have a dense mesh to refine the field contours. Thus, a line source with a length greater than 250 mil is unable to be solved. Given the requirements of exciting HFSS and the limitation in available compute resources,

it is not possible to separate the nulls produced by time retardation of the fields and the nulls introduced from the radiation of the wave port source.

The final attempt to compare the ASJE and HFSS numerical simulation is preformed by reducing the length of the line source in the ASJE simulation to that of the HFSS simulation: 250 mil. Figure 4.17 contains a side by side comparison of the simulation for a line length of 250 mil. The field plots agree and exhibit similar behavior. Figure 4.16a and Figure 4.16b compare the Electric field intensity magnitude along the X-Direction in two sub ranges. This comparison shows that the two simulators are in good agreement for the first 40 mil away from the line source. The location of nulls and peaks in the Electric field intensity magnitude after 40 mil differ by approximately 3 mil. These differences are surmised to be from both the finite conductor width in HFSS and the phase resolution limits in HFSS field plotting of 5 degrees.

4.4 Chapter Discussion and Conclusion

Chapter 4 explores the challenges faced in comparing an analytical solution to a numerical solution and the influence of simulation conditions on small field magnitudes. For the purposes of comparing the simulation of a finite length line source to determine if the time retardation effects were evident in the numerical solution, these challenges include the size and application of radiation boundary conditions, the mesh density and compute resource limitations, the length of the line source, as well as the potential to introduce additional propagating modes due to the size of the excitation. It is shown that careful attention to matching the simulator differences can yield results between ASJE simulation and ANSYS HFSS that are in good agreement. Confidence is obtained in ANSYS HFSS ability to correctly account for the same phenomena as shown in the Analytically Solved Jefimenko's Equation.

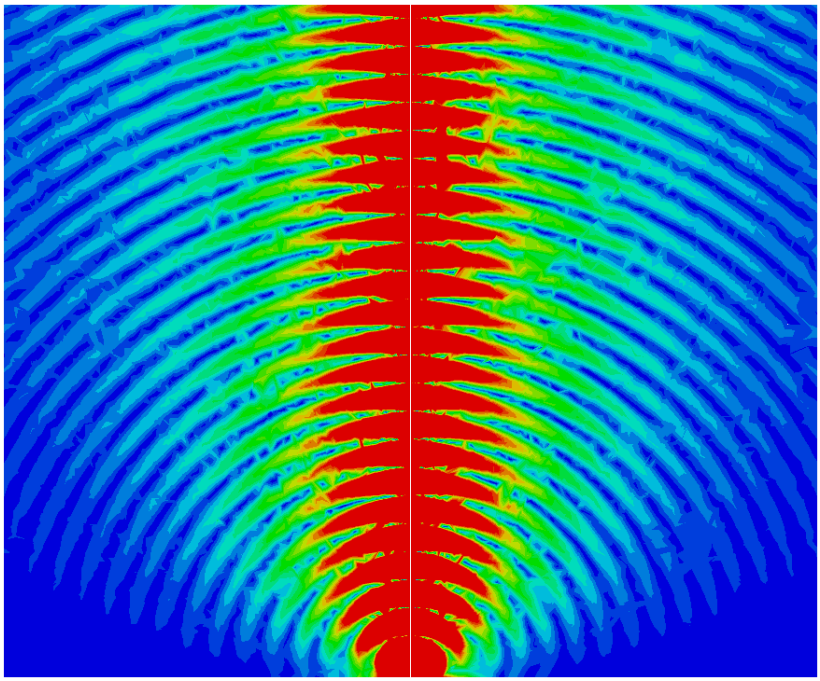

(a) X-Z plane cross-section

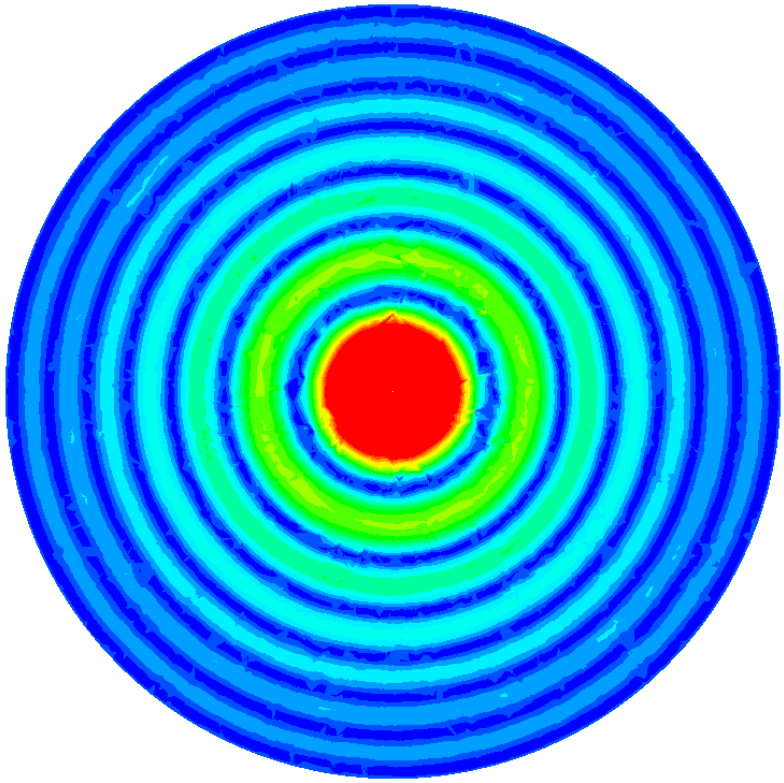

(b) X-Y plane cross-section

Figure 4.15: Line Source Electric Field Intensity Magnitude on the X-Z plane and X-Y plane cross-section

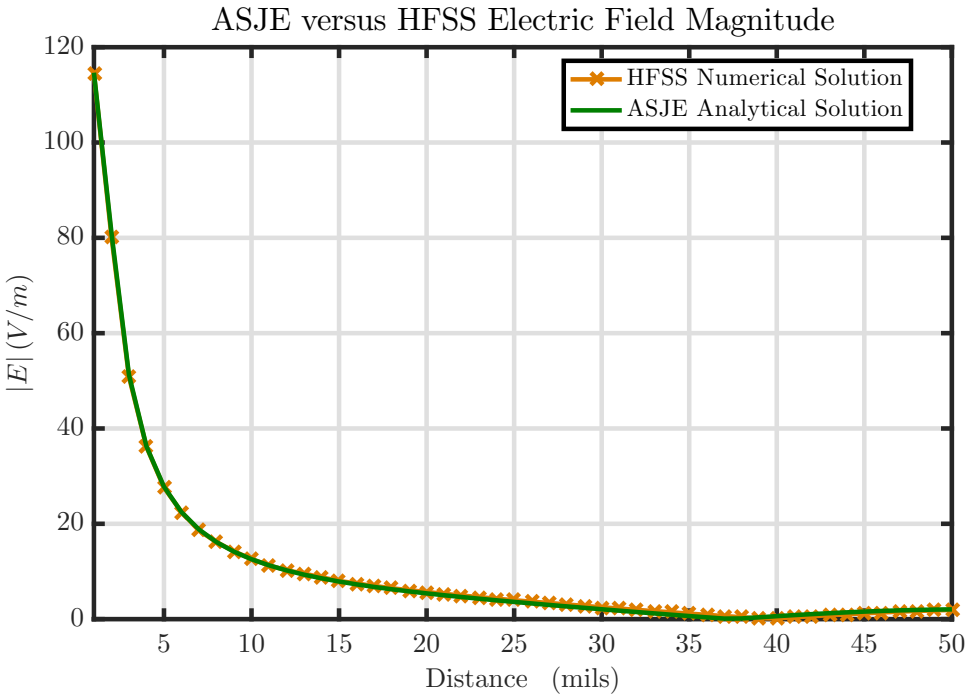

(a) 1 mil to 50 mil

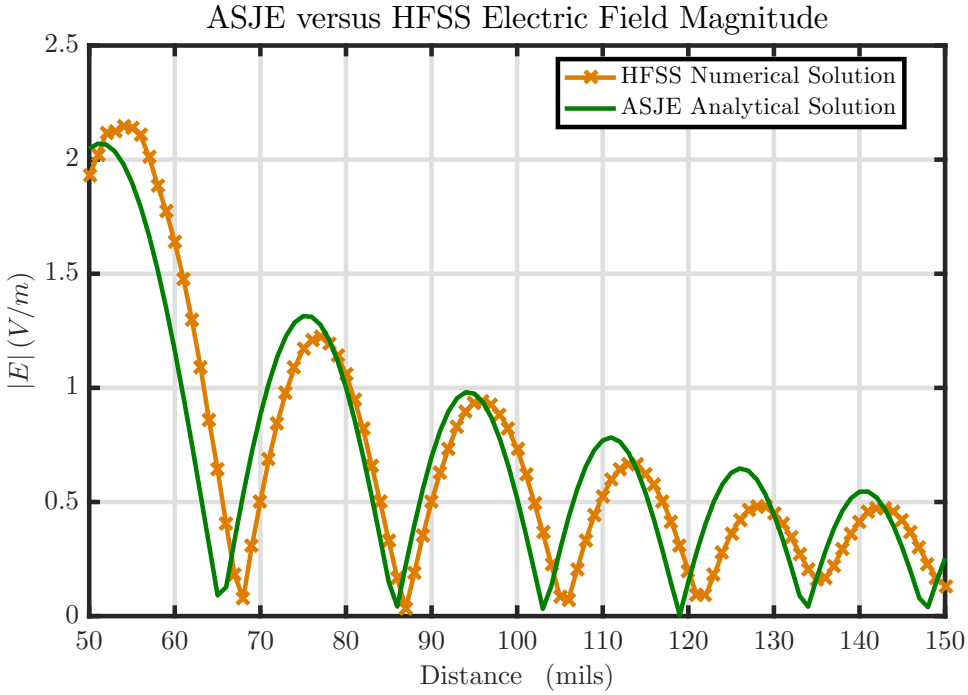

(b) 50 mil to 150 mil

Figure 4.16: Comparison of Electric Field Intensity Magnitude Along the X-Direction at the Height of the Circular Line Source

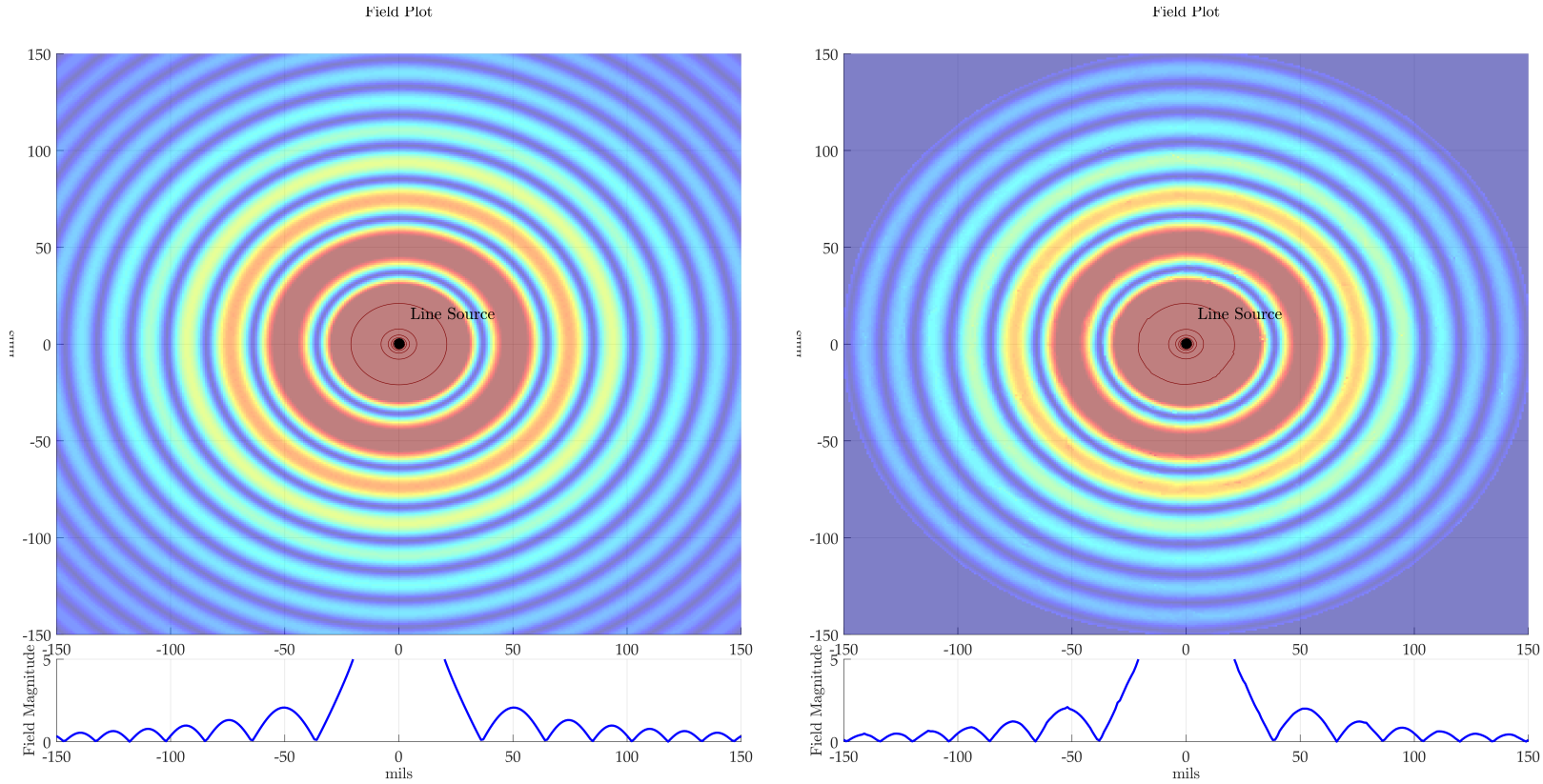

(a) ASJE

(b) ANSYS HFSS

Figure 4.17: Line Source Electric Field Intensity Comparison for a Length of 250 mils

Chapter 5

Test Apparatus for Measuring Time Retardation in Transmission Lines

The RLGC(p) transmission line model augments the Classical RLGC transmission line model by representing the time retardation of electromagnetic fields as a phase term added to each per-unit-length parameter. Measuring such a frequency dependent phase change in a transmission line structure requires that either the observation (e.g. probe) or the reference plane to be a physical distance from the source that is electrically significant. It is of interest to relate measurement results to time retardation in high speed digital interconnects, so the permittivity of the substrate chosen for a test apparatus transmission line is similar to printed circuit board transmission lines i.e. the relative permittivity of the substrate is approximately $\varepsilon_r = 4$. However, unlike a traditional printed circuit board's amalgamate of epoxy and glass fabric, the material chosen is lossless and homogenous so to remove the influence of dispersion and attenuation. These phenomena occlude the phase contribution from time retardation of the fields.

A low value of permittivity forces the frequency of the excitation to be high and the physical distance to the probing be increased to ensure that the time retardation is apparent in the phase measurements. Obtaining measurements at high frequencies are challenging because of several factors which are typically overcome by miniaturization especially the connection between the measurement equipment and the device under test (DUT). It is also desirable to have the DUT characteristic impedance match

closely to the measurement equipment source impedance to reduce mismatch error.

Observing the coupling phase between a second transmission line that is planar and adjacent to the excited transmission line is applicable to printed circuit boards. This coupling is referred to as crosstalk and is a paramount challenge to high speed interconnect design. Relating time retardation to crosstalk results in a better understanding of crosstalk at high frequencies. For this reason, the probe in the test apparatus is chosen to be an adjacent transmission line.

Standard printed circuit boards have two general categories and six sub categories of single ended transmission line waveguides. These are illustrated in Figure: 5.1. Microstrips are on the external layers of the board and striplines are on the internal layers. The subcategories of microstrip depend on the clearance to adjacent metal planes and the height of the coating applied. For co-planar microstrips, the metal clearance is such that the microstrip is intentionally referenced to the planar metal in addition to any metal plane beneath. The embedded microstrip is intentionally coated with a significant amount of epoxy to lower the influence of the air boundary. Remaining subcategories have either an additional metal plating on the copper or a minimal amount of epoxy coating to prevent oxidation. Stripline subcategories depend on the metal clearance to determine if it is a co-planar stripline or standard stripline. For measuring the phase resulting from time retardation, a structure similar to embedded microstrip has the advantage of stronger coupling versus spacing than does stripline and a reduced influence of the air boundary.

For the above reasons, the test apparatus designed and simulated in this chapter consists of three embedded microstrip waveguides constructed on a fused silica substrate. These transmission lines are covered with a fused silica lid that is 3 mm in thickness to reduce the air boundary influence. Figure 5.2 contains a rendering of this structure.

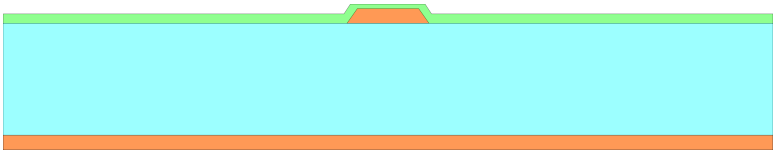

(a) Microstrip with Mask

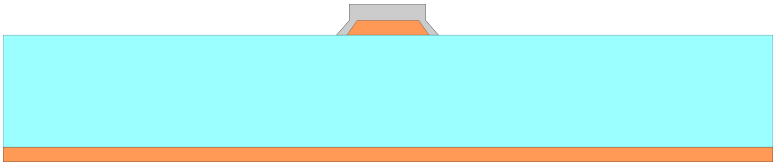

(b) Microstrip with Plating

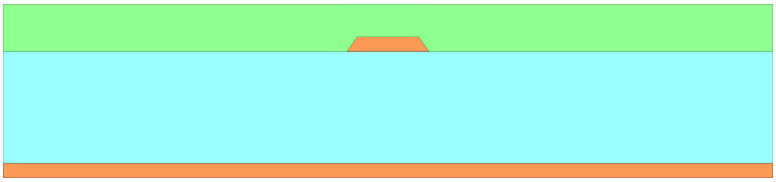

(c) Embedded Microstrip

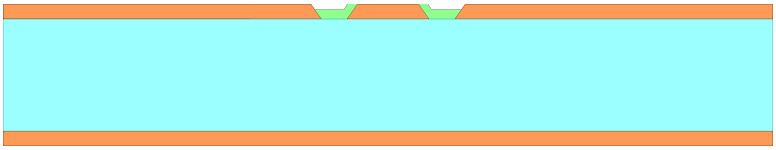

(d) Co-Planar Microstrip

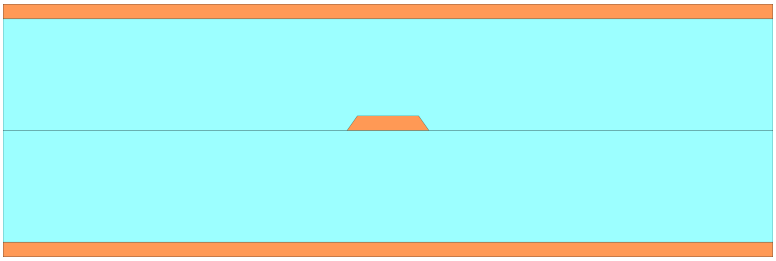

(e) Stripline

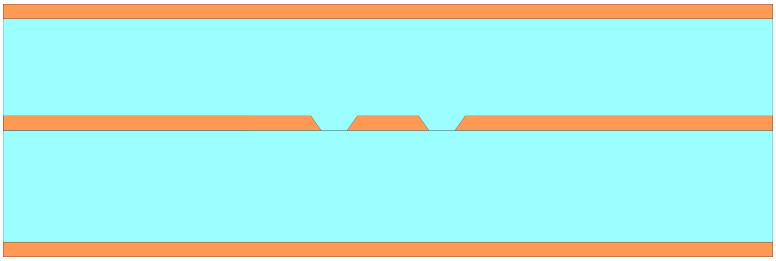

(f) Co-Planar Stripline

Figure 5.1: Printed Circuit Board Transmission Line Configurations

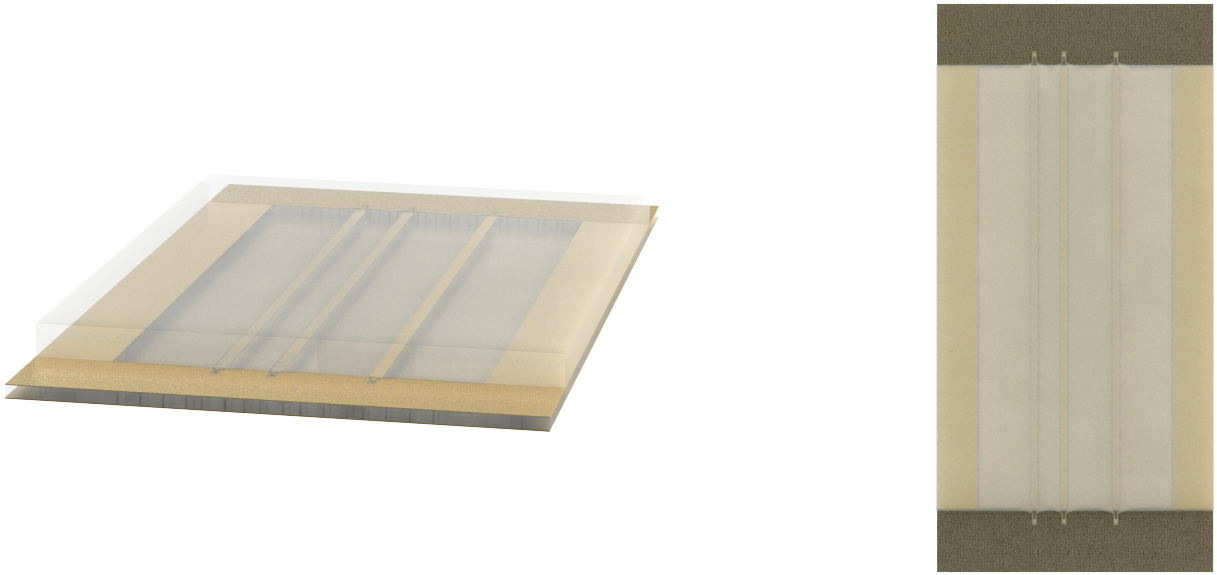

(a) Perspective View

(b) Top Down View

Figure 5.2: Rendering of the Test Apparatus: Three Embedded Microstrips on a Fused Silica Substrate

5.1 Test Apparatus Material and Construction

Fused silica (SiO_2) is used in several industries (in particular the medical industry for implanted devices and micro-fluid applications) because of its excellent mechanical, thermal, and chemical properties [46]. In the electronics industry, fused silica (and other glasses) are used as substrates for silicon devices and in other research areas because it combines the benefits of ceramic, organic, and silicon such as ultra-low electrical loss, dimensional stability, surface smoothness, and adjustable coefficient of thermal expansion [47].

Fused silica is an amorphous solid glass that can achieve high purity compared to fused quartz. Although often used interchangeably by name, fused quartz is produced by melting layers of naturally occurring quartz or other silicon dioxide sources whereas fused silica is produced from gases containing silicon such as silicon tetra chloride ($SiCl_4$). The gas is burned in the presence of oxygen and nano-particles of (SiO_2) are layered through chemical vapor deposition. The two families of deposition are: the one step family which is directly melting onto a fused silica rod, and the two step family (vitrification) where (SiO_2) soot is accumulated then condensed onto a fused silica rod [48]. The resulting glass is homogeneous containing very little metal particles. The fused silica in the test apparatus is an industrial grade of Corning HPFS® 7980 which is certified with purity of 0.04 parts per million [49].

Electrical permittivity of fused silica at microwave frequencies (15 GHz to 21 GHz) is influenced by purity, phase transition, and microstructure which depend on the preparation method. Values of relative permittivity versus different preparation methods range from $\varepsilon_r \sim 3.7$ to 3.9 with loss tangents that range from $tan\delta \sim 2 \times 10^{-5}$ to 8×10^{-6} [50]. It is believed that industrial grade of Corning HPFS® 7980 is produced with a direct melting method; therefore, a relative permittivity $\varepsilon_r = 3.8$ is taken for the design of the test structure.

When shaping holes and channels in the substrate, the fused silica is not drilled

by a diamond bit which is the more conventional method. Instead, a selective laser etching (SLE) technique is used to achieve high precision in three dimensions (1 µm) and a minimum feature size of 10 µm. Using ultrashort-pulsed laser radiation focused within the glass the chemical and optical characteristics are changed without cracking. The irradiated material is then selectively removed by wet-chemical etching. This enables complex shapes (such as through-glass vias) to be channeled into the fused silica glass [51].

The aspect ratios (10:1) from the SLE technique for through-glass-vias (TGV) present a challenge for metallization because of limitations in sputtering coverage of the seed layer. Although, it is noted that improvements in this technique are the subject of research in through-silicon-vias [52]. To fill the TGV in the test apparatus, a proprietary process using conductive paste to fill these holes before a sintering process hermetically seals and renders a conductive path through the glass. The side effect of this process is the low conductivity (5 m$\Omega/\square$) of the conductive path.

Filling a wide transmission line with conductive paste is an unexplored technique at the time of the design of the test apparatus. There is a significant risk to the manufacturing of test apparatus as designed because the stresses incurred by the substrate during the sintering process can crack and reduce side wall adhesion of the paste. This could cause the paste to partially fill and disrupt the conductive path . Therefore, an alternative metallization technique is planned as a mitigation path if the paste filling is unsuccessful during manufacturing.

The alterative metallization is to have copper plated on the top of the fused silica substrate. To allow the fused lid to be place on top of this structure and reduce the air gap, a thin film of polyimide is applied up to the height of the plated copper. Polyimide is a synthetic polymer that has favorable chemical and thermal properties. It is used often in the electronics industry as an insulator and particularly with flexible circuits [53]. Dielectric properties are similar to printed circuit board material;

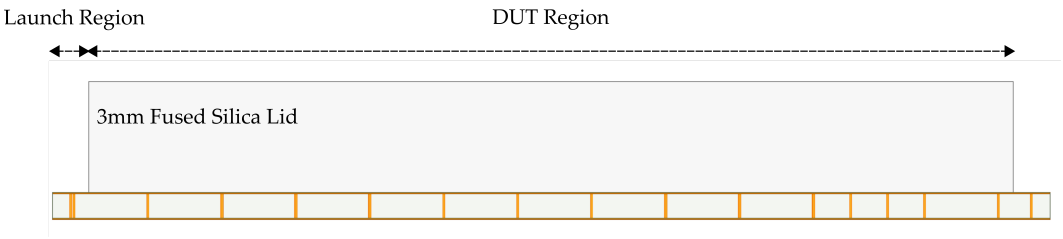

Figure 5.3: Test Apparatus Side View of the DUT and Launch Regions

however, the loss factor is significant compared to the fused silica substrate [54]. It should be noted that the polyimide layer thickness will be on the order of 3um compared to 700um thickness of the fused silica substrate.

The remaining sections in this Chapter will be focused on the design and simulation of test apparatus without the polyimide layer and the transmission line signal path as a laser formed and etched channel filled with conducted paste.

5.2 Design Considerations of the Test Apparatus

Three transmission lines are instantiated in the test apparatus. The middle line is the excited line and the other two lines provide two separate distances from metal edge to metal edge: 1.27 mm and 2.54 mm. These adjacent lines are to be used as probes to measure the phase of the coupled signals.

There are two distinct regions of the test structure that need design attention, and they are illustrated in Figure 5.3. The first is the DUT region. It requires that a width of transmission line is manufactured to achieve a characteristic impedance near the reference impedance of the vector network analyzer, 50 Ohm. Given the electrical properties of the fused silica and the available wafer thickness of 700 µm, a line width of 700 µm yields an impedance of 62 Ohm. There are limitations to the maximum length that can be routed on a glass wafer or risk damage of the structure. As a precaution, the lengths are limited to 25 mm and 12.5 mm.

The second region is the launch region. In this region, the 3 mm thick lid is

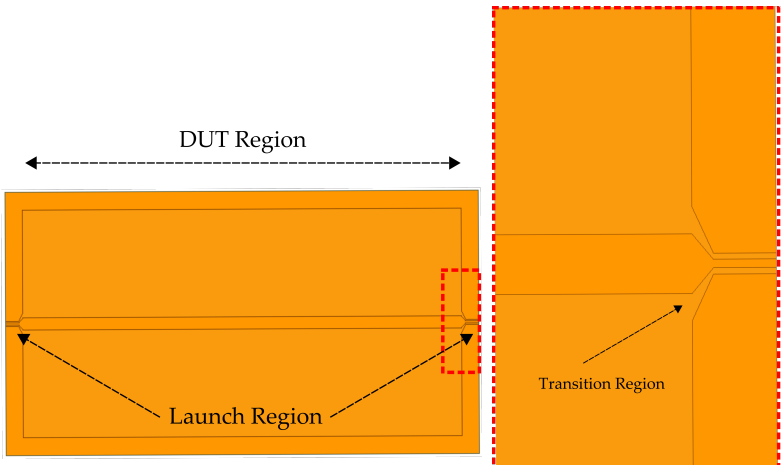

(a) Top Down View with a Red Box Indicating the Transition Region

(b) Top Down View of the Transition Region as Boxed in Figure 5.4a

Figure 5.4: Test Apparatus Top Down View of the DUT Regions, Launch Regions, and Transition Region

recessed to allow access by microprobes. A reference plane is brought near the probe landing to create a co-planar microstrip. This is done to both control the launch trace impedance and to provide a landing for the ground blades of the microprobes when in a ground-signal-ground configuration. The transition region from probe landing to DUT uses a tapered impedance transformer and metal clearance to match impedance for a broad frequency range. Figure 5.5 contains a top down view of the microwave transition region. It is noted that the original design of the transition region and DUT width for a 400 µm thick wafer was not available for manufacturing. Therefore, the manufactured transformer region is not optimal for bandwidths above 60 GHz as is discussed in Section 5.3.

5.3 Simulation of the Test Apparatus

In this section, a review of the predicted electrical performance of the test apparatus is discussed. Simulations of the entire test apparatus including the launch region

are performed in ANSYS HFSS for a single transmission line. These are expected to closely match the measurements obtained of the test structure. Simulations are also performed on the DUT region without the launch which reduce to a set of three uniform transmission lines. In addition to the ANSYS HFSS full wave simulation, a quasi-static simulator ANSYS Q2D is also used to evaluate these three transmission line cross-sections. This simulation provides a frequency response contrast that does not include the time retardation of the fields.

Evaluation of the entire test apparatus for lengths of 25 mm and 12.5 mm is performed in the frequency domain by analyzing the scattering parameters of insertion loss (S21) and return loss (S11) from 50 MHz to 60 GHz. The former indicates the power loss versus frequency while the latter denotes the power reflected back into port one when injected at port one. A useful design criteria to ensure that the phase and phase delay of the scattering parameters is recoverable is to design the cross over frequency of insertion loss and return loss to be as high in frequency as possible. This is also an acceptable criterion for de-embedding methods which relies on the difference of two similar structures [55].

A plot of the frequency domain response is found in Figure 5.5a. From this plot, the crossover frequency is in the region of 45 GHz to 60 GHz. This crossover between insertion loss and return loss is influenced by the transition between the launch region and the DUT region. Obtaining a more optimized transition region was limited by the available wafer thickness and feature size of the tapered transmission line.

Another metric for evaluation the transition region is to convert the return loss to the time domain with the appropriate Inverse Fourier Transform. The resulting plot is the time domain reflectometry (TDR) response where the reflection coefficient is converted to impedance. Figure 5.5b contains the test apparatus TDR response with a stimulus rise time of 10 ps. From these responses, the $\sim 4\Omega$ overshoot of the impedance in the transition region around 0.05 ns and again at 0.35 ns for the test

apparatus of length 25 mm is enough impendence mismatch to limit the crossover frequency seen in Figure 5.5a.

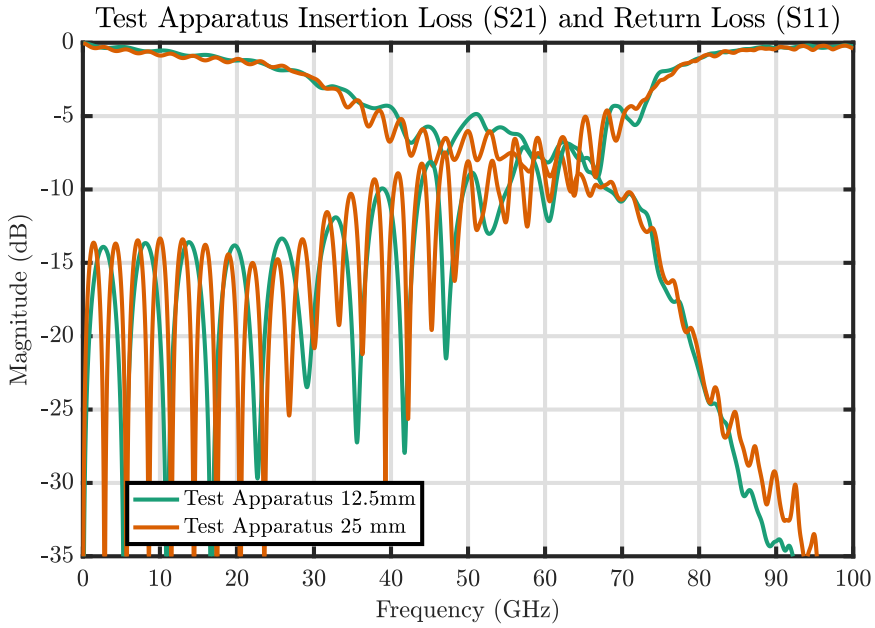

(a) Frequency Domain Responses

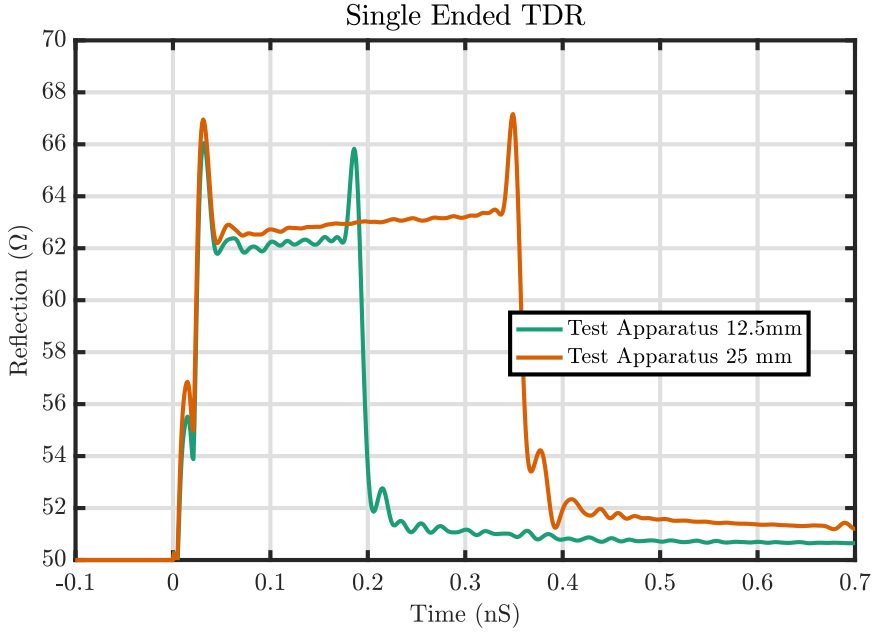

(b) Time Domain Reflection Responses

Figure 5.5: Simulation Responses of both the 12.5 mm and 25 mm Test Apparatus Including the Launch Region

5.3.1 Simulation of a Single Uniform Transmission Line: Progressively Adding Losses

The materials chosen for the construction of the test apparatus and discussed in Section 5.1 are not without some conductor and dielectric losses. It is important to examine the relative impact of adding these loss mechanisms, and the potential to occlude the phase impact of time retardation. For this examination, ANSYS HFSS simulation of a uniform cross-section without the launch region and at a length of 25 mm is generated.

A dielectric of fused silica contains losses on the order of two to three magnitudes lower than conventional PCB material as such the contribution of dielectric loss to phase and dispersion is expected to be small. The conducting material that fills the lased and etched channel and constitutes a transmission line is not pure copper rather it is a sintered paste of copper and glass binders. The conductivity of this paste is much lower than pure copper and simulated as 15 percent of copper. Because phase is decreased by the absorbing of the field versus the skin depth, the change from PEC to copper to paste does show a decrease in phase [8] as well as impact the attenuation of the signal versus frequency.

Figure 5.6 and Figure 5.7 show the scattering parameter results when progressively adding loss to the uniform transmission line. First, the lossless dielectric is changed to a fused silica model that contains loss. Next, the PEC conductor is assigned as copper. The final simulation replaces the copper conductivity with that of the conductivity of the paste.

Figure 5.6a depicts the increase in signal loss versus frequency for each added loss mechanisms. The largest increase in insertion loss is from the low conductivity of the paste. This culminates at -0.9dB of signal attenuation at 100 GHz and is approximately 0.5dB more attenuation as compared to copper. Figure 5.6b contains the phase delay versus frequency as calculated from the unwrapped phase ϕ_{unwrap} as

in Equation 5.1.

$$PhaseDelay = -\frac{\phi_{unwrap}}{\omega} \tag{5.1}$$

The phase delay versus frequency is similar between the lossless simulation and when adding the lossy fused silica material assumptions. Changing the conductivity assumptions from PEC to copper and then to the paste show an increase in the phase delay or a slowing of the signal propagation. This agrees with expectation and is approximately 2 ps of for the paste conductivity.

Figure 5.7a and Figure 5.7b contain similar information concerning the unwrapped phase versus frequency. It is difficult to discern the differences in phase from Figure 5.7a so a subtraction of each progressive loss simulation from the lossless simulation is performed. This is referred to as Phase Delta and is plotted in Figure 5.7b. Here a positive value indicates that the phase has decreased compared to the lossless case. This is shown for the cases where the conductivity is increased over that of PEC and it is notable that this phase decrease is nonlinear versus frequency. When the simulation is changed from lossless to include the dielectric losses in fused silica, the phase increases in value versus frequency. This increase is smaller than the decrease in phase due to decreased conductivity. The Phase Delay from lossless dielectric and perfect conductor to all the predicted losses in the system is on the order of 0.06 radians or 3.44 degrees.

5.3.2 Simulation of a Single Uniform Transmission Line Comparing ANSYS HFSS and ANSYS Q2D

Simulations are also performed on the DUT region without the launch which leaves a set of three uniform transmission lines. ANSYS HFSS is used to provide the full wave solution which contains the time retardation of the fields and ANSYS Q2D is used as the quasi-static simulator. This simulation provides a frequency response contrast that does not include the time retardation of the fields.

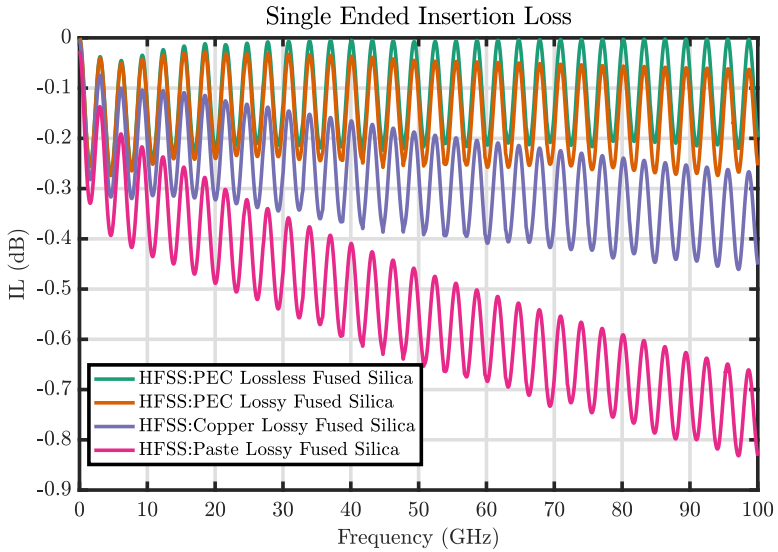

(a) Insertion Loss (S21)

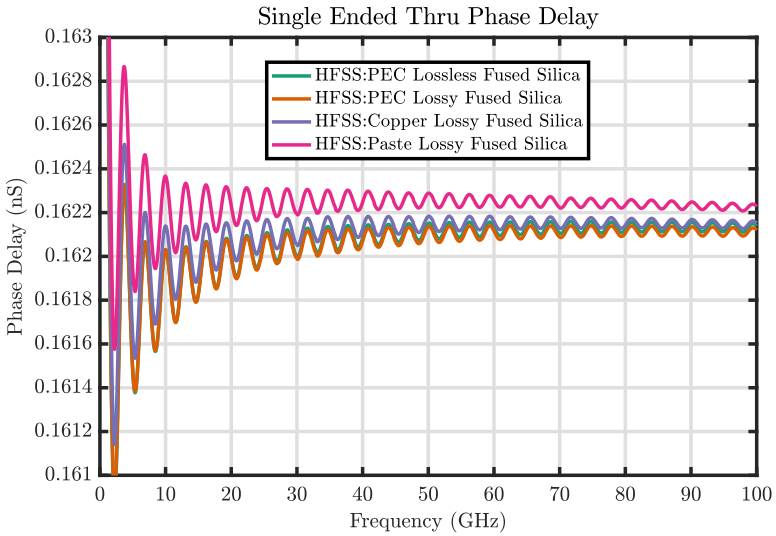

(b) Phase Delay

Figure 5.6: Insertion Loss and Phase Delay of Uniform Transmission Line for Incremental Losses

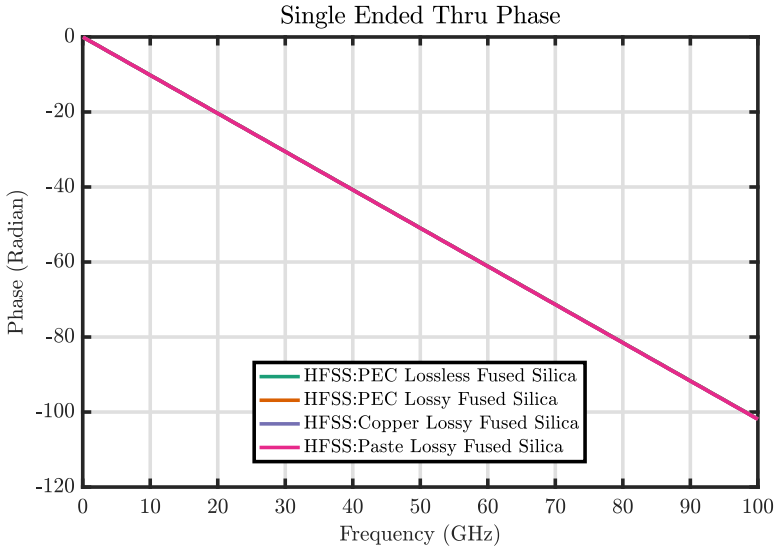

(a) Unwrapped Phase (S21)

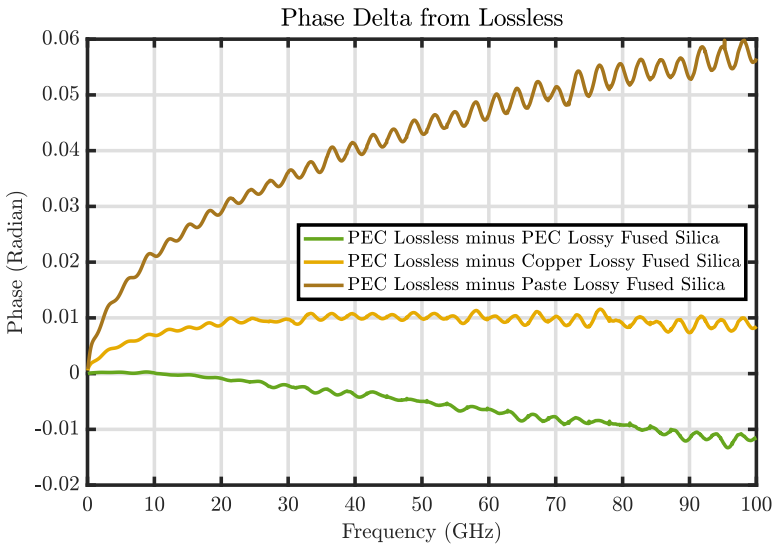

(b) Phase Delta

Figure 5.7: Unwrapped Phase and Phase Delta of Uniform Transmission Line for Incremental Losses

Figure 5.8a contrasts the attenuation or insertion loss S21 versus frequency of the test apparatus simulated in both HFSS (solid lines) and Q2D (dashed lines) for both the lossless assumptions and conductivity assumptions of the Paste. These simulators are in agreement until 10 GHz after which frequency the Q2D simulation continues linearly and the two solutions diverge for both material assumptions.

Figure 5.8b contains the phase delay versus frequency from both simulators and both material assumptions. The simulators again diverge around 10 GHz with the HFSS simulations showing 0.5 ps longer delay for the same physical length of transmission line. When the conductivity is changed from PEC to that of the paste, both simulators predict similar changes in phase delay. Mismatch between the 50 Ω port impedance to the characteristic impedance of the transmission line $\sim$ 64 Ω creates noise oscillations for both simulations.

Figure 5.9a and Figure 5.9b contain similar information concerning the unwrapped phase versus frequency. It is difficult to discern the differences in phase from Figure 5.9a so a subtraction of the unwrapped phase is performed. This is referred to as Phase Delta and is plotted in Figure 5.9b. The difference is obtained to compare Q2D minus the HFSS simulation for the lossless and paste conductivity. Phase delta between HFSS for both material assumptions and Q2D for both material assumptions is also plotted. Here a positive value indicates that the phase has decreased compared to the case from which the phase is being subtracted. The difference in phase between HFSS and Q2D increases with frequency and reaches a total decrease of almost 0.4 radians (22.9 degrees) at 100 GHz versus Q2D. The difference in phase versus frequency for both material assumptions in both simulators reaches between 0.05 and 0.07 radians much less than the difference between the simulators.

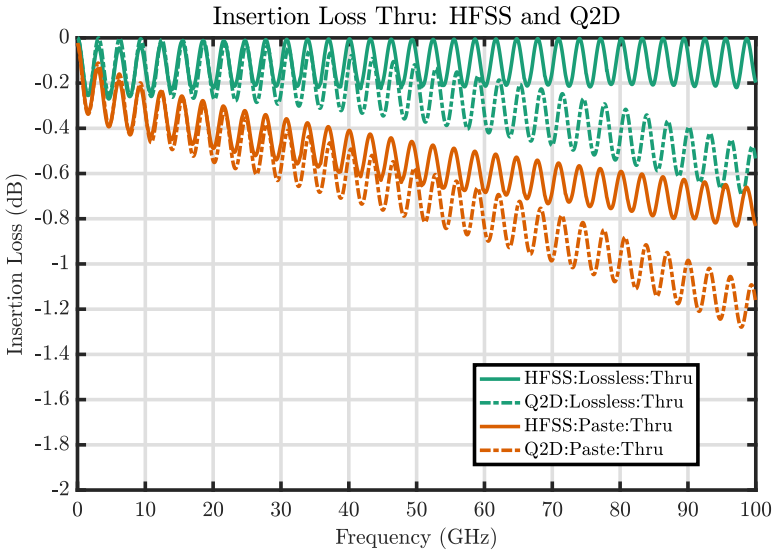

(a) Insertion Loss (S21)

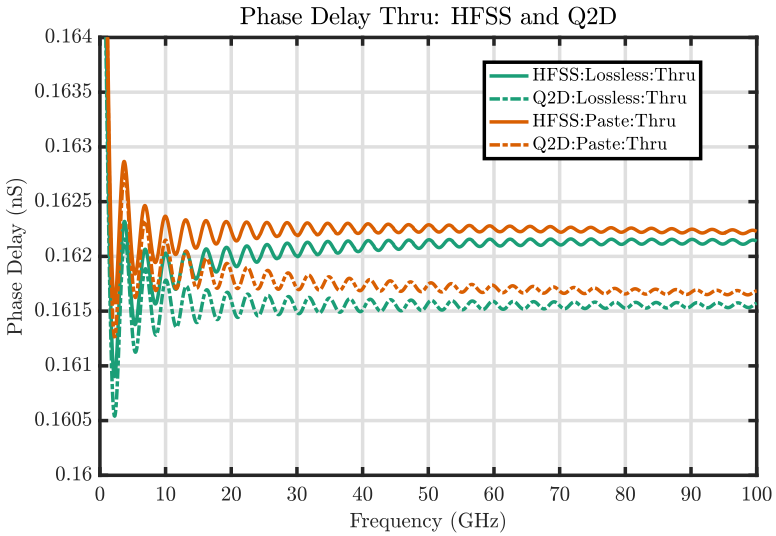

(b) Phase Delay

Figure 5.8: Insertion Loss and Phase Delay Comparison between HFSS and Q2D

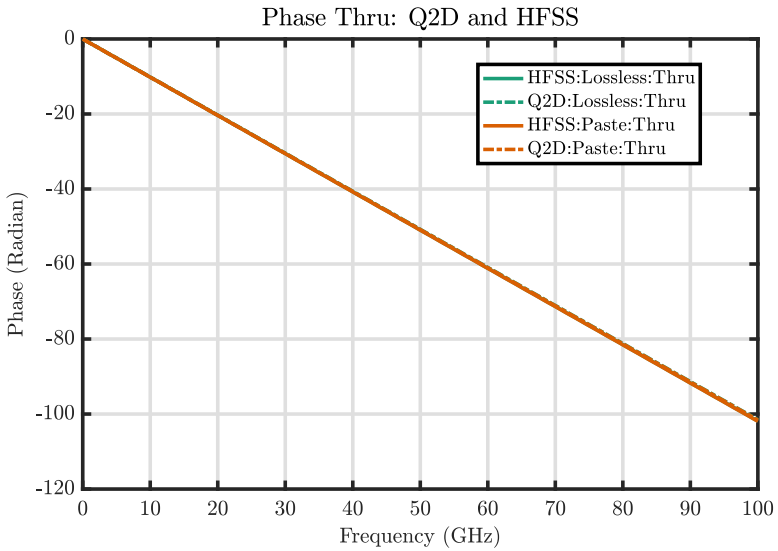

(a) Unwrapped Phase (S21)

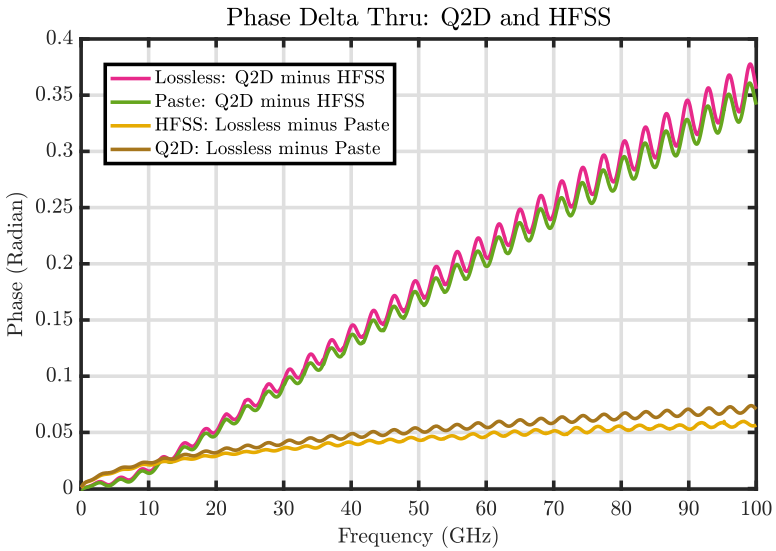

(b) Phase Delta between Q2D and HFSS

Figure 5.9: Unwrapped Phase and Phase Delta Comparison between HFSS and Q2D

5.3.3 Simulation of the Coupling Response in the Uniform Transmission Line Region

Using the same uniform geometry as in Section 5.3.2, the coupling as analyzed at the end of the adjacent transmission lines - also referred to as far end crosstalk (FEXT) - is compared when simulated both with Q2D and HFSS. For this section, a focus will be on the time delay or phase shift between a transmission line that is placed at a distance of 50 mil versus a transmission line that is placed at a distance of 100 mil. Given that one transmission line is farther away, the phase delay will be more when compared to the transmission line that is nearer to the excited transmission line.

Far end crosstalk is probed as illustrated in Figure 5.10 where port 2 is excited and the signal is measured as received at port 4 and port 6. The associated scattering parameters are S_{42} and S_{62}. The magnitude of FEXT in decibels is compared for

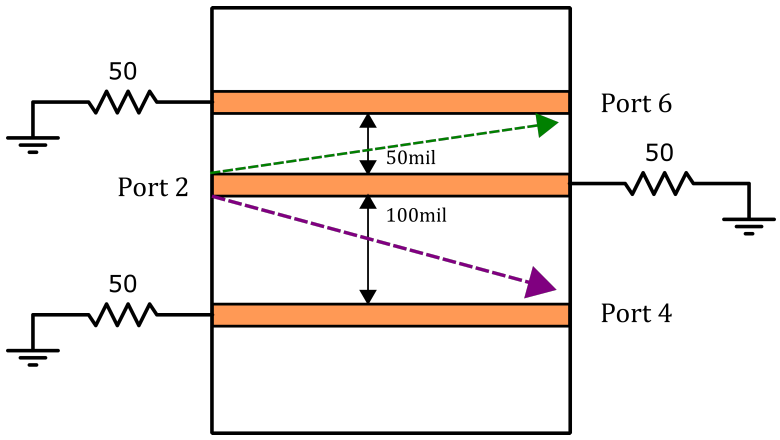

Figure 5.10: Illustration of Far End Crosstalk (FEXT) as Viewed Looking Down on the Test Apparatus

distances of 50 mil and 100 mil and for both simulation tools in Figure 5.11a. A smaller coupling magnitude is seen in a transmission line that is farther away which meets expectation.

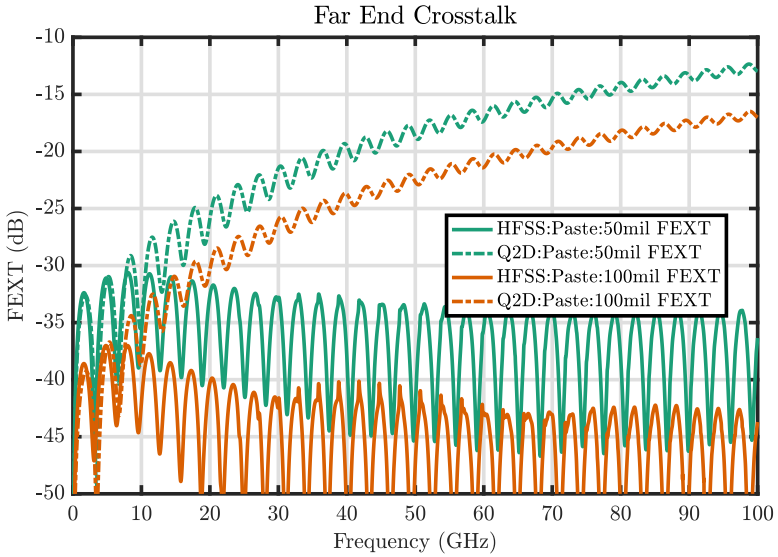

(a) Far End Crosstalk (FEXT) Magnitude

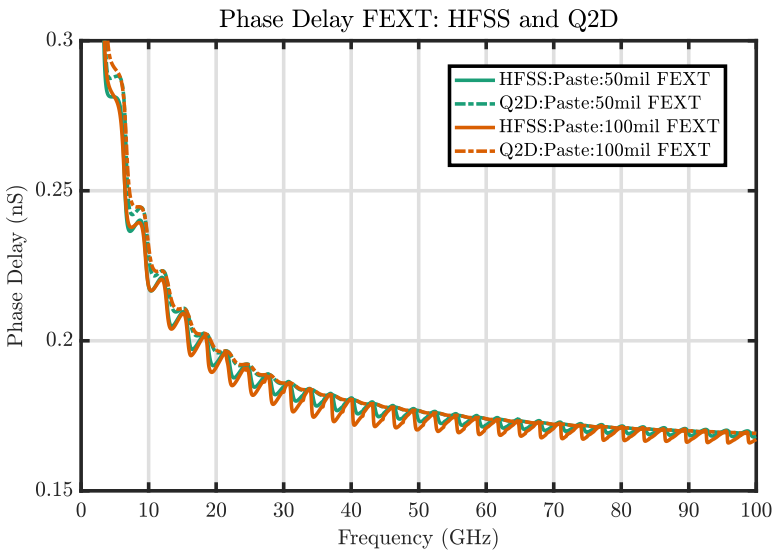

(b) Phase Delay of Far End Crosstalk (FEXT)

Figure 5.11: Far End Crosstalk (FEXT) Magnitude and Phase Delay Comparison between HFSS and Q2D for Distances of 50mil and 100mil

This magnitude versus frequency has a very different trend for the HFSS simulations compared to Q2D when the frequency increases beyond 10 GHz. Crosstalk magnitude in Q2D continues to become greater with frequency whereas the HFSS simulation levels off versus frequency.

Figure 5.11b contains the phase delay of the coupling scattering parameters versus frequency for both simulators. From this plot, the Q2D simulations do not show a phase delay difference between the transmission lines that are spaced at different distances. Conversely, the HFSS simulation does show a difference; however, it is difficult to discern the exact difference because of the oscillatory noise present in the phase delay calculation. For this reason, fitting functions are performed on both unwrapped phase and phase delay.

The unwrapped phase versus frequency is fit with a linear function as described in Equation 5.2 and with coefficients found in Table 5.1.

$$y = ax + b \tag{5.2}$$

Table 5.1: Fitting Coefficients for the Linear Fit of Unwrapped Phase

Phase Fit	**a**	**b**
Q2D FEXT 50 mil	-1.0173	-4.5493
Q2D FEXT 100 mil	-1.0168	-4.5882
HFSS FEXT 50 mil	-1.0202	-4.0200
HFSS FEXT 100 mil	-1.0120	-3.9270

Phase delay versus frequency is fit with a power function as described in Equation 5.3 and with coefficients found in Table 5.2. The fitted response versus the actual

response is found Figures 5.12a and 5.12b.

$$y = ax^b + c \tag{5.3}$$

Table 5.2: Fitting Coefficients for the Power Fit of Phase Delay

Phase Delay Fit	**a**	**b**	**c**
Q2D FEXT 50 mil	0.5386	-0.8868	0.1598
Q2D FEXT 100 mil	0.6081	-0.9344	0.1608
HFSS FEXT 50 mil	0.5559	-0.9439	0.1614
HFSS FEXT 100 mil	0.6731	-1.0253	0.1613

To better compare the fitted unwrapped phase and fitted phase delay versus frequency, a subtraction is performed whereby the 50 mil transmission line scattering parameters are subtracted from the 100 mil scattering parameters. This is referred to as phase delta and phase delay delta. These results are found plotted in Figures 5.13a and 5.13b. For this subtraction, a positive number indicates that the 50 mil spaced transmission line has a greater delay. In Figure 5.13a, the Q2D simulation indicates that the fitted unwrapped phase is similar for both distances; whereas, the fitted unwrapped phase for the HFSS simulation indicates a phase delta of 0.6 radian (34 degrees) at 60 GHz. In Figure 5.13b, the fitted phase delay for 50 mil separation is greater that the 100 mil separation for the HFSS simulation. This is not expected. In Chapter 4, it was found that the size of the port can influence the field distributions. It is supposed that due to the excitation size needed to encompass all of the transmission lines in a single port excitation that the phase delay of the coupling is counter intuitive for the HFSS simulation between 100 mil and 50 mil.

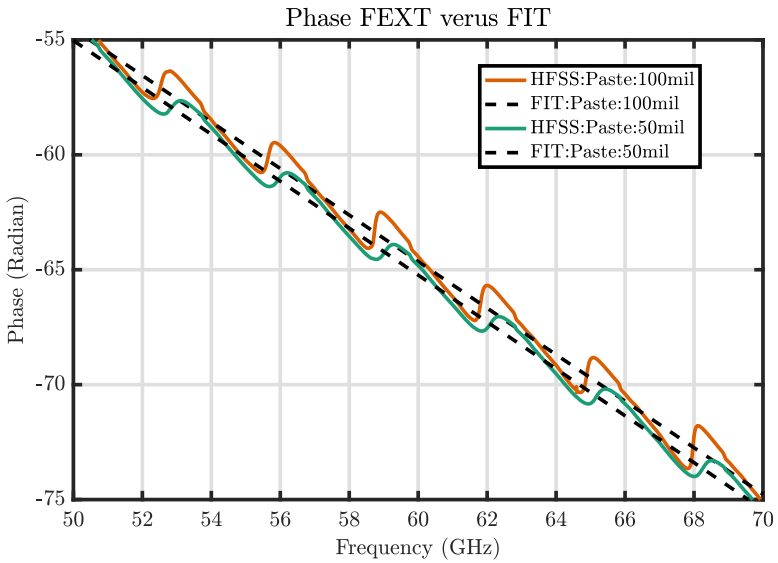

(a) FEXT Phase Curve Fit

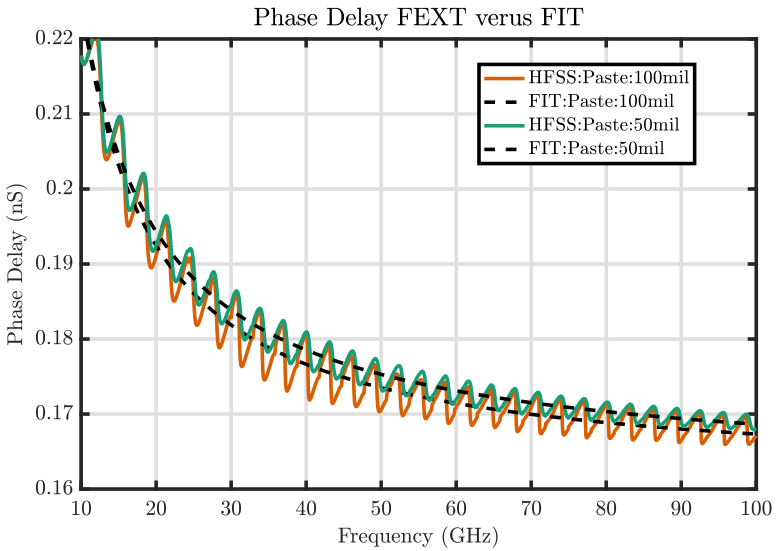

(b) FEXT Phase Delay Curve Fit

Figure 5.12: Far End Crosstalk (FEXT) Phase and Phase Delay Curve Fits for Distances of 50mil and 100mil

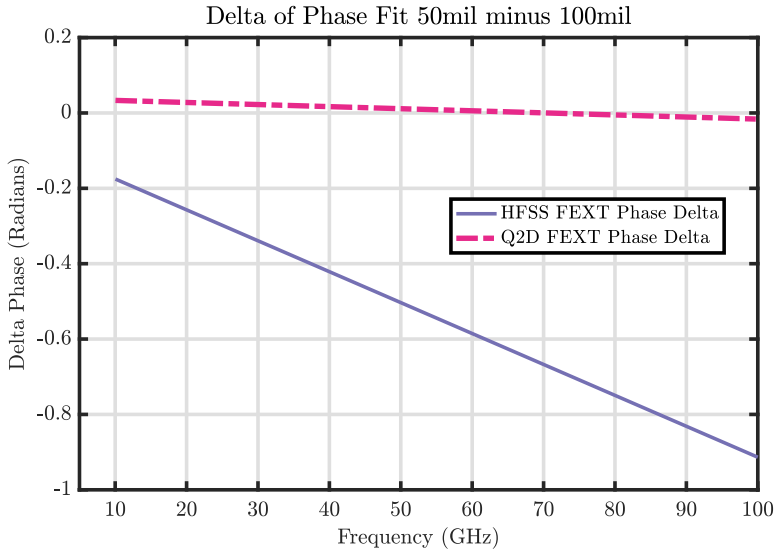

(a) Far End Crosstalk (FEXT) Phase Delta

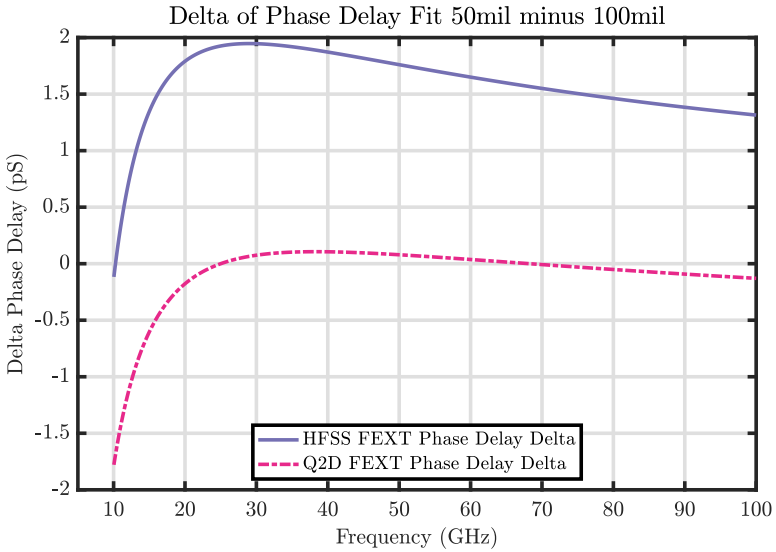

(b) Far End Crosstalk (FEXT) Phase Delay Delta

Figure 5.13: Far End Crosstalk (FEXT) Phase and Phase Delay Comparison of HFSS and Q2D for Distances of 50 mil and 100 mil

5.3.4 Simulation of the Coupling Response for the Test Apparatus

In Sections 5.3.2 and 5.3.3, only the uniform DUT region of the test apparatus was analyzed so to enable a comparison between Q2D and HFSS. In this section, the entire test apparatus including the launch regions is simulated in HFSS. These simulation are expected to more closely resemble the coupling in the physical device. Because of the construction of the launch region, the excitation will have less influence on the phase and phase delay of the coupling responses.

Figure 5.14a contains the FEXT magnitude response versus frequency. Coupling between the transmission line that is closer in proximity of the excited line is greater than the transmission line that is farther away. In Figure 5.14b, the phase delay of the transmission line spaced 100 mil away from the excited line is greater than that of the transmission line spaced 50 mil away.

A phase delta is obtain by subtracting the phase of the transmission line 50 mil away from the transmission line that is 100 mil away. Figure 5.15a contains these results which indicate that the phase difference increases with frequency and reaches the largest delta of 2.5 radians (143.24 degrees) at 60 GHz.

To compare the phase delay between the two distances, a subtraction is performed similar to what is done for phase delta. These results are plotted in Figure 5.15b. The phase delay of the transmission line that is spaced at a distance of 100 mil is more than that of the transmission line space a distance of 50 mil. At a frequency of 60 GHz this amount of phase delay delta is 7 ps.

5.4 Chapter Discussion and Conclusions

Chapter 5 explores the design and simulation of a test apparatus for quantifying the time retardation impact on coupling in transmission lines on a Fused Silica substrate. Uniform cross-section simulation in Q2D is compared against a similar geometry is simulated in HFSS. As expected, the quasi-static assumptions in Q2D do not include

time retardation effects and the phase of the coupling between two lines of different distances is very similar. When the full test apparatus is analyzed in HFSS, the transmission line that is spaced 100 mil away from the excited transmission line has a phase difference of 143 degrees at 60 GHz and a phase delay difference of 7 ps at 60 GHz compared to the a transmission line that is spaced 50 mil away from the excited transmission line.

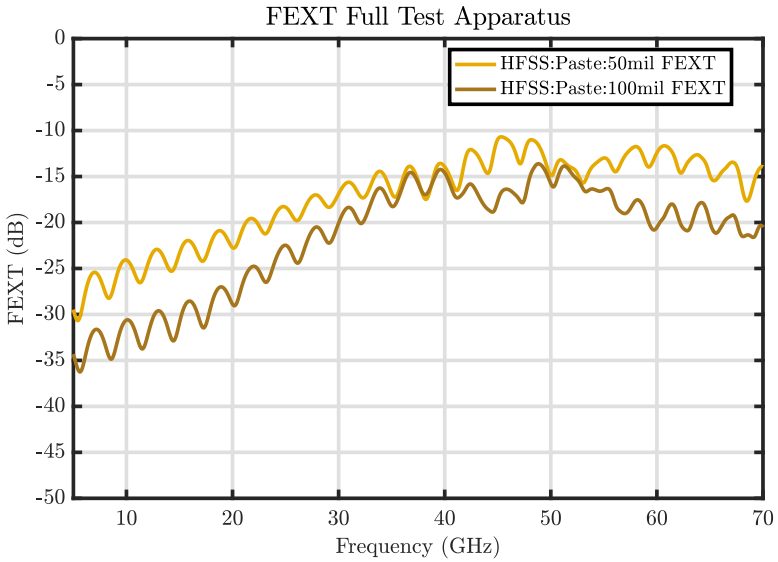

(a) Far End Crosstalk (FEXT) Magnitude

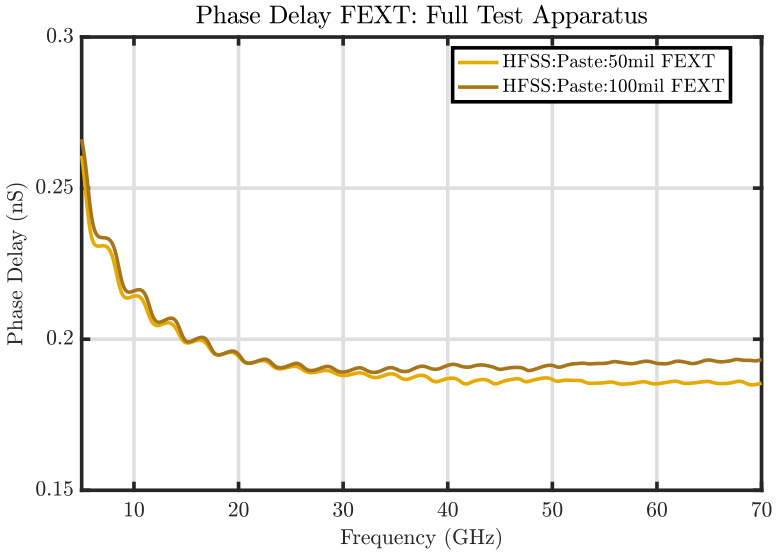

(b) Phase Delay of Far End Crosstalk (FEXT)

Figure 5.14: Test Apparatus Far End Crosstalk (FEXT) Magnitude and Phase Delay Comparison for Distances of 50mil and 100mil

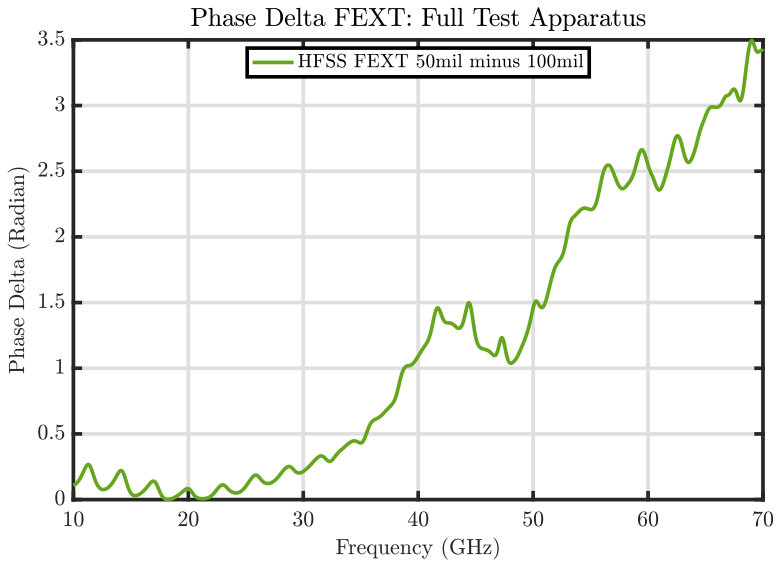

(a) FEXT Phase Delta 50 mil minus 100 mil

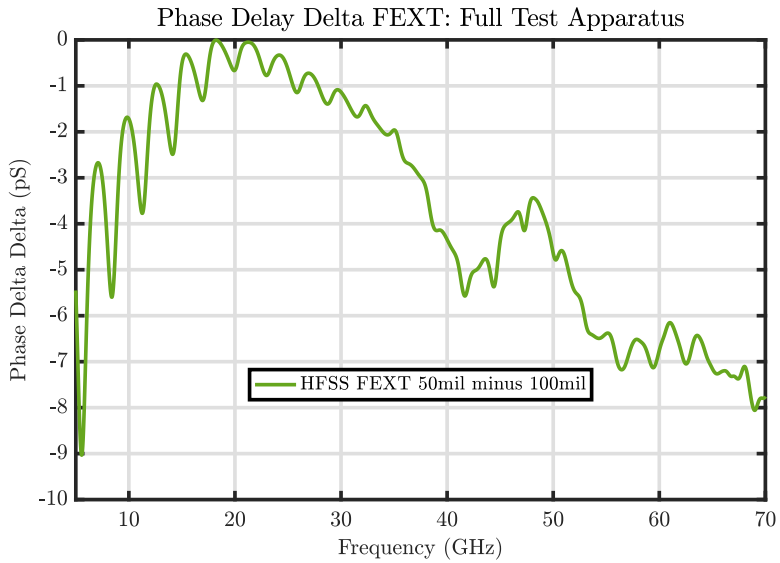

(b) FEXT Phase Delay Delta 50 mil minus 100 mil

Figure 5.15: Test Apparatus Far End Crosstalk (FEXT) Phase and Phase Delay for Distances of 50mil and 100mil

Chapter 6

Measurement Results of the Test Apparatus

The test apparatus as described in Chapter 5 was manufactured at SAMTEC Inc. Glass Core Technologies. However, there were challenges during several phases of the construction with the most notable defect being the inability to fill the channel with conductive paste. The stresses incurred by the substrate during the sintering process caused cracking and reduced the paste side wall adhesion to the fused silica substrate.

After trials with different proprietary paste formulations yielded unsuccessful conductive paths in the channel, a mitigation strategy was pursued in which an alternative metallization was attempted. This alterative metallization is to have copper plated on the top of the fused silica substrate. To allow the fused silica lid to be placed on top of this structure and eliminate the air gap, a thin film of polyimide is applied up to the height of the plated copper. Polyimide is a synthetic polymer that has dielectric properties similar to printed circuit board materials. It should be noted that the thickness of the polyimide layer is 3 µm compared to 700 µm thickness of the fused silica substrate; therefore, the influence on the measurements of the polyimide layer is expected to be minimal. Figure 6.1 contains a comparison of the original build up and metallization as well as the alternative build up and metallization. This chapter provides analysis of the measurements made on the alternative construction of the test apparatus.

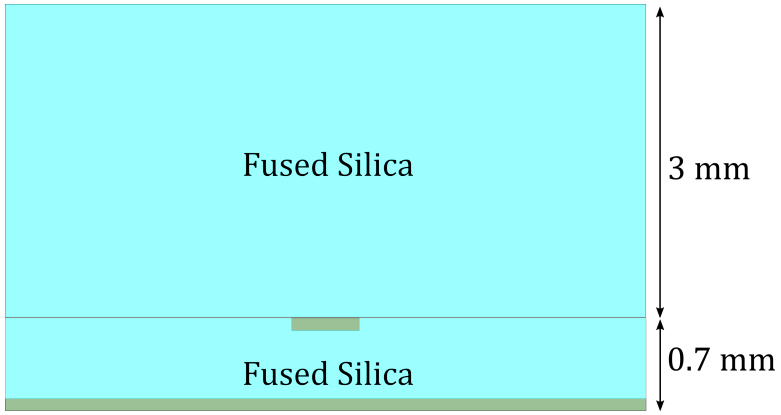

(a) Original Test Apparatus

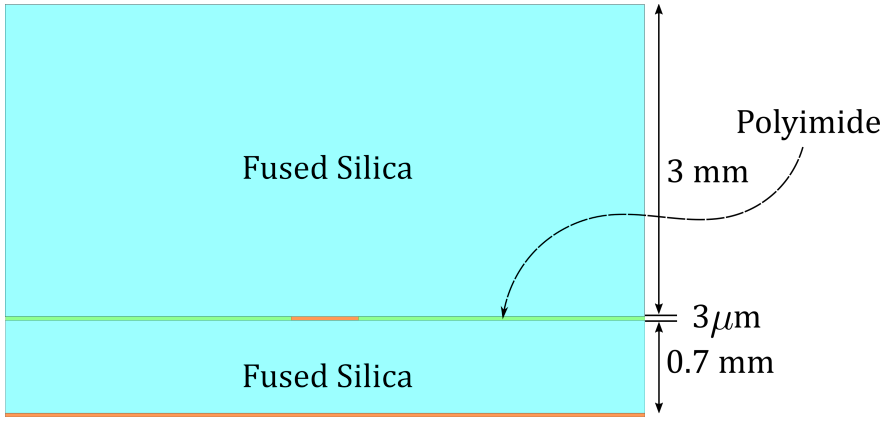

(b) Alternative Test Apparatus

Figure 6.1: Build Up Layer Descriptions for Original and Alternative Test Apparatus

6.1 Measurement Equipment and Data

Calibration of the Rohde & Schwarz ZVA67 vector network analyzer is performed to mathematically provide systematic error correction to the probe tips. To successfully contact the test substrate by matching the pitch of the measurement landing site, GGB Industries Dual PicoProbe® model number 67A-GSG-150/67A-GSG-150-DP-D-300 are employed [56]. These probes are in G-S-G-S-G configuration with a signal to ground pitch of 150 µm.

The type of measurement calibration selected is the short, open, load, thru (SOLT) method. Known error coefficients are loaded onto the vector network analyzer specific to the CS-2-150 substrate provided by GGB Industries Inc. Figure 6.2 is a photo

of an unused calibration substrate. The measurement calibration establishes a fixed reference plane at the ends of the probe tips of zero phase shift, zero reflection, lossless transmission, and known impedance [57]. Figure 6.3 is a photo of the measurement setup showning the vector network analyzer, the vibration isolation table, and the micro position probe holder which adjust the PicoProbes®.

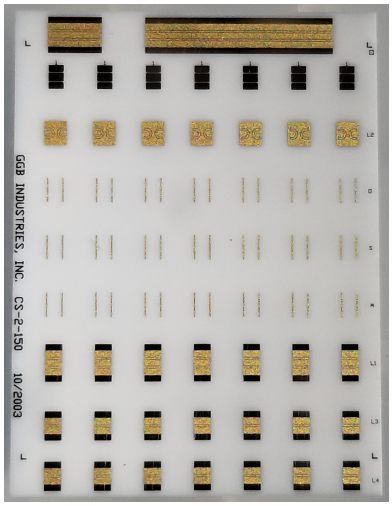

Figure 6.2: SOLT Calibration Substrate

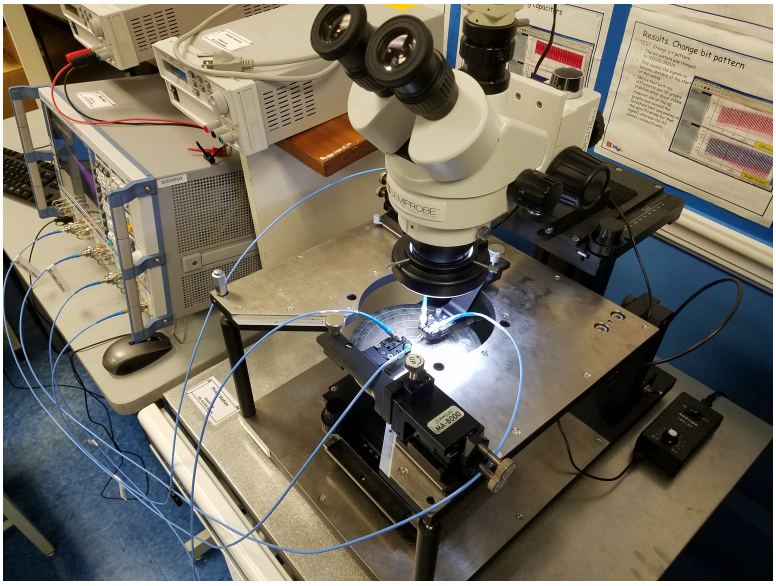

Figure 6.3: Measurement Setup

As described in Chapter 5, the holes in the Fused Silica substrate are shaped by selective laser etching with ultrashort-pulsed laser radiation focused within the glass.

The chemical and optical characteristics are changed without cracking, and the irradiated material is then selectively removed by wet-chemical etching. To fill the TGV and provide a conductive path from the top and bottom surface metal, a proprietary process using conductive paste is used before a sintering process hermetically seals the TGV. A microscope image of the TGV for the test apparatus before metallization of the glass surface is provided in Figure 6.4.

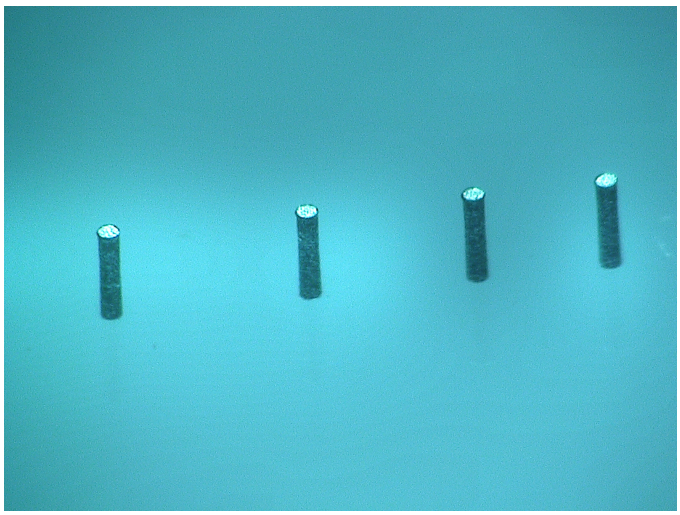

Figure 6.4: Metallization of Holes in Fused Silica Wafer

So that copper plating can adhere to the top and bottom of the Fused Silica substrate, a sputtering of titanium and copper (TiCu) must first be laid down in selected areas where copper is to be plated. Copper is then electrolytically deposited to a thickness of 3 µm before a layer of polyimide is cured only in the open area of the test apparatus. The polyimide layer is also a mask for the electroless nickel immersion gold (ENIG) deposition so that surface finish is not applied in areas other than the landing site for the probes and surrounding top surface metal. Figure 6.5 contains a photos of the test apparatus before the Fused Silica lid is bonded. Figure 6.6 is the finished test apparatus where the lid is bonded to create an embedded microstrip transmission line.

After successful calibration to the tips of the PicoProbes®, it was found that the

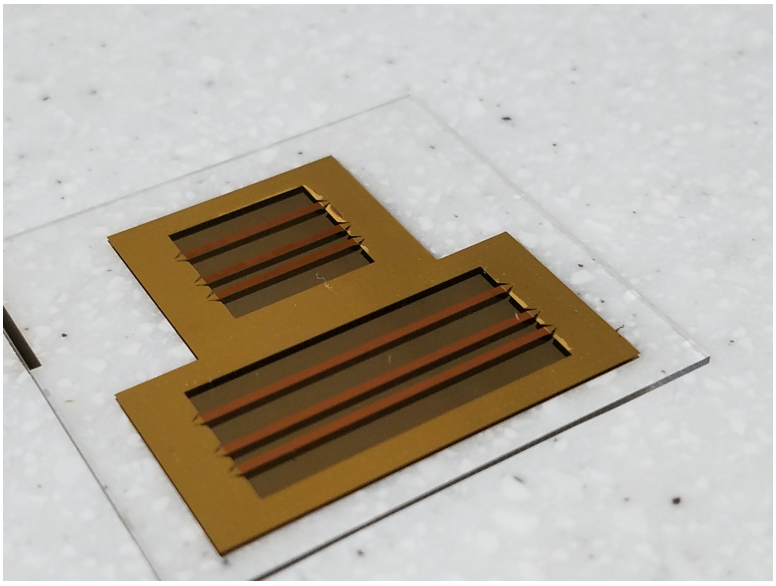

Figure 6.5: Test Apparatus without Fused Silica Lid

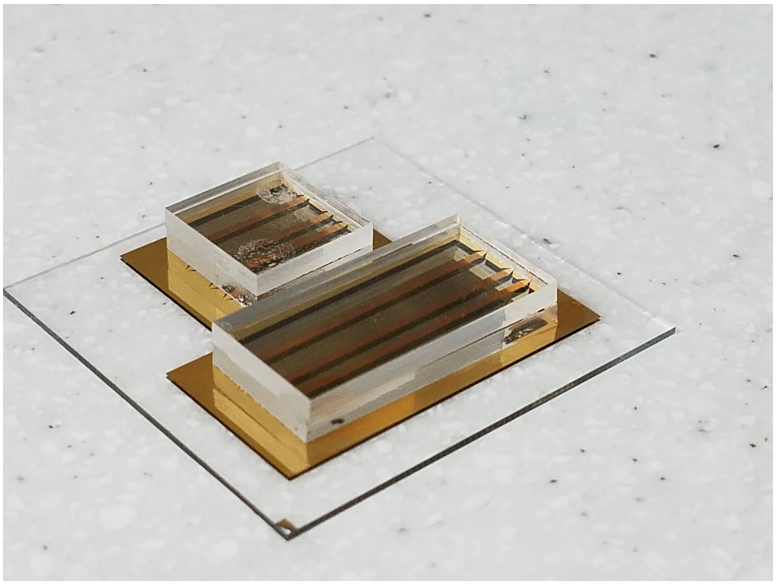

Figure 6.6: Test Apparatus with Fused Silica Lid

through path scattering parameters of a single transmission line were not showing expected results; more specifically, the measured results were characteristic of a electrical short rather than the through path of a transmission line. Upon inspection, it was found that the ENIG deposition leached into the area between the signal and the adjacent reference metal. The additional metal in this 25 µm gap created an electrical short. This rendered the test apparatus unsuccessful. A photo of the leached metal

at the probe landing site is shown in Figure 6.7.

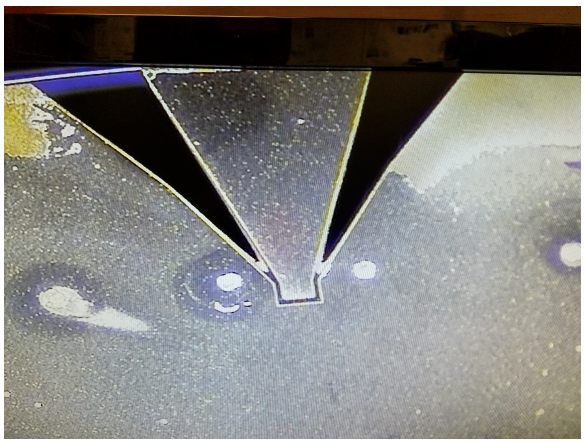

Figure 6.7: Unexpected Metal Migration that Shorts Signal to Ground

6.2 Chapter Discussion and Conclusions

A test apparatus was manufactured and measurement characterization with a vector network analyzer was attempted. However, after several challenges during the device construction, it is apparent that the technology is yet immature for the substrate chosen. In particular, the metal to metal clearance when ENIG is deposited can not be at a minimum distance of 25 µm without electro migration into the gap. As of the writting of this research, it was not determined if the measurement characterization of the test apparatus agreed with the simulation experiments contained in Chapter 5.

Chapter 7

Conclusion and Future Work

Chapter 3 examines applications of time retarded fields as they propagate in a microstrip transmission line. Surface charge density propagating on the top of the signal conductor at the speed of light is contrasted with surface charge density propagating on the bottom of the signal conductor where the medium enforces a velocity one-half the speed of light. A new loss mechanism in microstrip transmission lines is speculated to exist namely Cherenkov radiation.

Chapter 4 recapitulates the challenges faced in comparing an analytical solution to a numerical solution and the influences of simulation conditions on small field magnitudes. It is shown that careful attention to matching the simulator differences can yield results that are in good agreement. Confidence is obtained in ANSYS HFSS ability to correctly account for time retarded electromagnetic fields.

Chapter 5 describes the design and simulation of a test apparatus for quantifying the time retardation impact to coupling of transmission lines in a Fused Silica substrate. Simulation contrasted in HFSS predicts that a transmission line that is spaced 100 mil away from the excited transmission line has a phase difference of 143 degrees at 60 GHz and a phase delay difference of 7 ps at 60 GHz compared to a transmission line that is spaced 50 mil away.

Chapter 6 details the challenges during manufacturing of the test apparatus. Measurement characterization with a vector network analyzer was attempted but unsuccessful. After several challenges during the device construction, it is apparent that the technology is yet immature for the substrate chosen. In particular, the metal to

metal clearance when ENIG is deposited cannot be at a minimum distance of 25 µm without electro migration into the gap. As of the writting of this research, it was not determined if the measurement characterization of the test apparatus agreed with the simulation experiments contained in Chapter 5.

7.1 Future Work

The test apparatus designed in Chapter 5 is expected to match the predicted simulation results. As the capability of metallization on a glass surface matures, a measurable device will be produced. Attempts to fabricate and measure another device are on-going.

A suggested area of future study is to experiment with ways to visualize the time retarded behavior of electromagnetic fields. Ideally, the electromagnetic field pattern similar to those found in Figure 4.10 is projected onto a material that illuminates in the present of an electromagnetic field. One potential material is electroluminescent paint that is used for auto body lighting effects. Such paints are excited with 9V-24V DC input to an inverter producing 1.8 kHz AC. In the commercial usage, a capacitor is formed from layers of paint with the top coat being a conductive, clear coating. The electroluminescent film layer is sandwiched between other dielectric layers for protection [58].

It is proposed that this electroluminescent film layer could be applied to a sheet with a wire passing through. The wire would then be excited with a 100 GHz sinusoidal source to produce the desired electromagnetic field patterns. It is unknown if the wire would need to directly contact the electroluminescent film. If the film can be excited without contact, other visualizations of fields at different distances from the source could be observed.

Another application of the electroluminescent film (or other luminescent materials) is to apply a coat on the top of the a microstrip waveguide as described and

simulated in Chapter 3. The device could then be excited continuously with a voltage pulse train. Ringing dipoles that fluoresce in the material would begin to build after each successive passing of a pulse and lead to an intensity that should be seen visually. The forefront pulse traveling, at the speed of light in air, should cause the material dipoles to "ring" where that pulse has its greatest intensity; near the starting point of the device. Bright areas at the input side should be seen with the pulse dying exponentially as the pulse propagates. By using several electroluminescent paints of different colors it might be proven experimentally that Cherenkov radiation results in a non-opaque dielectric material.

Yet another potential avenue for visualizing Cherenkov radiation in a microstrip transmission line would be to submerge the test apparatus in water during measurement or to place a glass container of water on top of the test apparatus. Water presents an even greater mismatch in the propagation velocity of surface charge density between the bottom and top signal conductor surfaces. The surrounding water may even give off the characterize blue glow of Cherenkov radiation of nuclear reactor.

Bibliography

[1] P. Ye. "Applying the Retarded Solution of Electromagnetic Fields to PCB Transmission Line RLGC Modeling". PhD thesis. University of South Carolina, 2015.

[2] S.H. Hall and H.L. Heck. *Advanced Signal Integrity for High-Speed Digital Designs*. Wiley - IEEE. Wiley, 2011. ISBN: 9781118210680.

[3] P.J. Nahin. *Oliver Heaviside: The Life, Work, and Times of an Electrical Genius of the Victorian Age*. Johns Hopkins University Press, 2002. ISBN: 9780801869099.

[4] Bill Glover. *History of the Atlantic Cable & Undersea Communications*. Oct. 2016. URL: `http://atlantic-cable.com//`.

[5] William Thomson. "On the theory of the electric telegraph". In: *Proceedings of the Royal Society of London* 7 (1854), pp. 382–399.

[6] Clayton R. Paul. *Analysis of Multiconductor Transmission Lines*. John Wiley and Sons Ltd, Nov. 13, 2007. 780 pp. ISBN: 978-0-470-13154-1.

[7] P.G. Huray. *Maxwell's Equations*. Wiley - IEEE. Wiley, 2011. ISBN: p.

[8] P.G. Huray. *The Foundations of Signal Integrity*. Wiley - IEEE. Wiley, 2009. ISBN: 9780470543467.

[9] C.A. Balanis. *Advanced Engineering Electromagnetics, 2nd Edition*. Wiley, 2012. ISBN: 9781118213483.

[10] D.M. Pozar. *Microwave Engineering, 4th Edition*. Wiley, 2011.

[11] P. Besnier S. Chabane and M. Klingler. "A Modified Enhanced Transmission Line Theory Applied to Multiconductor Transmission Lines". In: *IEEE Transactions on Electromagnetic Compatibility* 59.2 (2017), pp. 518–528.

[12] D.G. Swanson and W.J.R. Hoefer. *Microwave Circuit Modeling Using Electromagnetic Field Simulation*. Artech House microwave library. Artech House, 2003. ISBN: 9781580536882.

[13] D. Poljak, F. Rachidi, and S. V. Tkachenko. "Generalized Form of Telegrapher's Equations for the Electromagnetic Field Coupling to Finite-Length Lines Above a Lossy Ground". In: *IEEE Transactions on Electromagnetic Compatibility* 49.3 (2007), pp. 689–697. ISSN: 0018-9375. DOI: 10.1109/TEMC.2007.902179.

[14] J. B. Nitsch and S. V. Tkachenko. "High-Frequency Multiconductor Transmission Line Theory". In: *Foundations of Physics* 40.9 (2010), pp. 1231–1252. ISSN: 1572-9516. DOI: 10.1007/s10701-010-9443-1.

[15] J. B. Nitsch and S. V. Tkachenko. "Complex-valued transmission-line parameters and their relation to the radiation resistance". In: *IEEE Transactions on Electromagnetic Compatibility* 46.3 (2004), pp. 477–487. ISSN: 0018-9375. DOI: 10.1109/TEMC.2004.831905.

[16] P. Besnier S. Chabane and M. Klingler. "Extension of the transmission line theory application with modified enhanced per-unit-length parameters". In: *Progress In Electromagnetics Research M* 32 (2013), pp. 257–270.

[17] P.D.J. Nitsch, F. Gronwald, and P.D.G. Wollenberg. *Radiating Nonuniform Transmission-Line Systems and the Partial Element Equivalent Circuit Method*. Wiley, 2009. ISBN: 9780470682418.

[18] S. G. Pytel Jr. "Multi-gigabit Data Signaling Rates for PWBs including Dielectric Losses and Effects of Surface Roughness". PhD thesis. University of South Carolina, 2007, p. 111. ISBN: 9780549127659.

[19] O. Oluwafemi. "Surface Roughness and Its Impact on System Power Losses". PhD thesis. University of South Carolina, 2007. ISBN: 9780549420811.

[20] B.J. Hunt. *The Maxwellians*. Cornell history of science series. Cornell University Press, 2005. ISBN: 9780801482342.

[21] J.D. Jackson. *Classical Electrodynamics*. 3rd. Wiley, 2007. ISBN: 9788126510948.

[22] Oleg D Jefimenko. *Causality electromagnetic induction and gravitation: A different approach to the theory of electromagnetic and gravitational fields*. Princeton University Press, 2000.

[23] Oleg D Jefimenko. *Electromagnetic retardation and theory of relativity: new chapters in the classical theory of fields*. Electret Scientific Co, 1997.

[24] P. Ye, B. Gore, and P. Huray. "Applying the Retarded Solutions of Electromagnetic Fields to Transmission Line RLGC Modeling". In: *Advanced Electromagnetics* 6.1 (2017), pp. 56–62. ISSN: 2119-0275. DOI: 10.7716/aem.v6i1.420.

[25] Oleg D Jefimenko. *Electricity and Magnetism: An Introduction to the Theory of Electric and Magnetic Fields*. 2nd Edition. Electret Scientific Company, 1989. ISBN: 0-917406-08-7.

[26] David J. Griffiths. *Introduction to Electrodynamics*. Addison Wesley Pub. Co. Inc., Oct. 6, 2012. 624 pp. ISBN: 0321856562.

[27] John David Jackson. *Classical Electrodynamics*. 2nd Edition. Wiley, 1975. ISBN: 978-0471431329.

[28] U. Bellotti and M. Bornatici. "Time-dependent, generalized Coulomb and Biot-Savart laws: A derivation based on Fourier transforms". In: *American Journal of Physics* 64.5 (1996), pp. 568–570. DOI: 10.1119/1.18265.

[29] José A. Heras. "Time-dependent generalizations of the Biot-Savart and Coulomb laws: A formal derivation". In: *American Journal of Physics* 63.10 (1995), pp. 928–932. DOI: 10.1119/1.18086. eprint: http://dx.doi.org/10.1119/1.18086.

[30] R. de Melo e Souza et al. "Multipole radiation fields from the Jefimenko equation for the magnetic field and the Panofsky-Phillips equation for the electric field". In: *American Journal of Physics* 77.1 (2009), pp. 67–72. DOI: 10.1119/1.2990666.

[31] R.P. Feynman, R.B. Leighton, and M. Sands. *The Feynman Lectures on Physics: The New Millennium Edition: Mainly Mechanics, Radiation, and Heat*. v. 1. Basic Books, 2015. ISBN: 9780465040858.

[32] G. Romo. "Stack-Up and Routing Optimization by Understanding Micro-Scale PCB Effects". In: *DesignCon*. 2011.

[33] J. R. Miller G.J. Blando I. Novak. "Additional Loss due to Glass-Weave Periodic Loading". In: *DesignCon*. 2010.

[34] P. Pathmanathan. "Power Transmission Loss Due to Periodic Loading In Multi-Gigabit Data Signaling Interconnects". PhD thesis. University of South Carolina, 2012. URL: www.scholarcommons.sc.edu/etd/2201.

[35] C. Heard S. McMorrow. "The Impact of PCB Laminate Weave on the Electrical Performance of Differential Signaling at Muti-Gigabit Data Rates". In: *DesignCon East*. 2005.

[36] X. Ye J. Loyer R. Kunze. "Fiber Weave Effect: Practical Impact Analysis and Mitigation Strategies". In: *DesignCon*. 2007.

[37] A. R. Djordjevic et al. “Wideband frequency-domain characterization of FR-4 and time-domain causality”. In: *IEEE Transactions on Electromagnetic Compatibility* 43.4 (2001), pp. 662–667. ISSN: 0018-9375. DOI: 10.1109/15.974647.

[38] R. Lacombe. *Adhesion Measurement Methods: Theory and Practice*. CRC Press, 2005. ISBN: 9781420028829.

[39] A. B. Pippard. *Dynamics of Conduction Electrons (Documents on Modern Physics)*. Gordon & Breach Science Pub, 1965. ISBN: 0677007205.

[40] A. Healey E. Kochuparambil L. B. Artsi R. Mellitz C. Moore A. Ran P. Zivny M. Brown M. Dudek. “The State of IEEE 802.3bj 100Gb/s Backplane Ethernet”. In: *DesignCon*. 2015.

[41] A. Zangwill. *Modern Electrodynamics*. Modern Electrodynamics. Cambridge University Press, 2013. ISBN: 9780521896979.

[42] A. M. Helmenstine. “Why Is the Water Blue in a Nuclear Reactor? - Cherenkov Radiation: Why Nuclear Reactors Really Do Glow”. In: (2017). URL: www.thoughtco.com/blue-reactor-water-cherenkov-radiation-4037677.

[43] *SIwave Training: Signal and Power Integrity Analysis for Complex PCBs and IC Packages*. Dec. 2016. URL: www.ansys.com/Services/Training-Center.

[44] S. G. Johnson. “Notes on Perfectly Matched Layers (PML)”. Mar. 2010. URL: www.math.mit.edu/~stevenj/18.369/pml.pdf.

[45] *ANSYS Electromagnetics 18.1 Online Help: Excitations in HFSS*. 2017.

[46] Swift Glass. *Creating Glass That Withstands Extreme Environments*. Online Resource. URL: www.swiftglass.com/resource-library/.

[47] *3D Systems Packaging Research Center Booklet 2017*. Online. Jan. 2017. URL: www.prc.gatech.edu/sites/default/files/images/HomePage/prc_industry_consortium_booklet_-_may_2017.pdf.

[48] Heraeus Quarzglas. *Making of Fused Quartz and Fused Silica*. Heraeus Holding. Online Tutorial, 2017. URL: www.heraeus.com/en/hqs/fused_silica_quartz_knowledge_base/production_process/makingoffusedsilica.aspx.

[49] *Corning HPFS 7979, 7980, 8655 Fused Silica Optical Materials Product Information*. June 2014. URL: www.corning.com/worldwide/en/products/advanced-optics/product-materials/semiconductor-laser-optic-components/high-purity-fused-silica.html.

[50] Fang Yong et. al Li Lei. "Microwave Dielectric Properties of Fused Silica Prepared by Different Approaches". In: *International Journal of Applied Ceramic Technology* 11.1 (2014), pp. 193–199. ISSN: 1744-7402. DOI: 10.1111/j.1744-7402.2012.02846.x.

[51] Jens Gottmann and Martin Hermans. *Selective Laser Etching of Glass and Sapphire*. Fraunhofer Institute for Laser Technology. Mar. 2014. URL: www.ilt.fraunhofer.de.

[52] Tiwei Wei et al. "Optimization and evaluation of sputtering barrier/seed layer in through silicon via for 3-D integration". In: *Tsinghua Science and Technology* 19.2 (2014), pp. 150–160.

[53] *Flexible Printed Circuit Design Guide*. Tech-Etch, Inc. 2008. URL: www.tech-etch.com/flex.

[54] *Kapton Summary of Properties*. Dupont. 2017. URL: www.kapton.com.

[55] *A Simple, Powerful Method to Characterize Differential Interconnects*. Keysight Technologies. Aug. 2014.

[56] GGB Industries Inc. "High Performance Microwave Probes Model 67A". URL: www.ggb.com/67a.html.

[57] Keysight Technologies. *Specifying Calibration Standards and Kits for Keysight Vector Network Analyzers Application Note*. URL: www.keysight.com.

[58] LitCoat. "An Introduction to Light Emitting Paint". URL: www.litcoat.com/el-paint/electroluminescent-coating-or-paint-explained.

Appendix A

Permission to Reprint

Several figures within the dissertation were reprinted or redrawn with the expressed permission of the copyright owners. The following sections include the permissions granted to the author and the pertinent figures.

A.1 History of the Atlantic Cable & Undersea Communication

Bill Burns maintains a very informative website (atlantic-cable.com) preserving the history of the Trans-Atlantic telegraph cable. His content was heavily cited in Section 1. Specifically, Figure 1.1 is included with his permission provided via the email below:

> *On 7/18/2017 8:20 PM, GORE, BRANDON wrote:*
>
> *Hi Bill,*
>
> *I am writing my dissertation in electrical engineering, and I am including some historical information about the transatlantic telegraph cable. I have found your website extremely informative, and am citing it often. I would like to use the attached image which I believe is copyrighted. To include copyright information in my dissertation, I am required to include a permission letter in the appendix. Is it possible to use the attached image and are you able to allow its use?*
>
> *Regards,*
>
> *Brandon*

On 7/18/2017 9:00 PM Bill Burns billb@ftldesign.com wrote:

Brandon: I took that photo of a cable display case at the Science Museum in London a few years ago, so it's my copyright. I'm happy to give permission for you to use it in your dissertation (I'm an EE myself, from England long ago!) Please credit to "Atlantic-Cable.com Website".

Regards,

Bill

A.2 Foundations of Signal Integrity

The author obtained a personal, non-exclusive, non-sub licensable (on a standalone basis), non-transferable, worldwide, limited license (License Number 4312020693023; dated March 18th, 2018) for Figure 3.2. In *The Foundations of Signal Integrity* by Paul G. Huray this graphic is also found as Figure 6.5. This copyrighted material is owned by or exclusively licensed to John Wiley & Sons, Inc. or one of its group companies (each a"Wiley Company") or handled on behalf of a society with which a Wiley Company has exclusive publishing rights in relation to a particular work (collectively "WILEY").

A.3 Classical Electrodynamics

The author obtained a personal, non-exclusive, non-sub licensable (on a standalone basis), non-transferable, worldwide, limited license (License Number 4312021149969; dated March 18th, 2018) for Figure 3.7. In *Classical Electrodynamics 3rd Edition* by John David Jackson this graphic is also found as Figure 13.5. This copyrighted material is owned by or exclusively licensed to John Wiley & Sons, Inc. or one of its group companies (each a"Wiley Company") or handled on behalf of a society with

which a Wiley Company has exclusive publishing rights in relation to a particular work (collectively "WILEY").